

University of Nevada, Reno

**Benchmark of CFD Simulations Using Temperatures
Measured Within an Enclosed Array of Heater Rods Oriented
Vertically and Horizontally**

A thesis submitted in partial fulfillment of the
requirements for the degree of Doctoral of Philosophy in
Mechanical Engineering

By

Narayana Rao Chalasani
Dr. Miles Greiner /Thesis Advisor

December, 2010



University of Nevada, Reno
Statewide • Worldwide

THE GRADUATE SCHOOL

We recommend that the dissertation
prepared under our supervision by

NARAYANA RAO CHALASANI

entitled

**Benchmark Of CFD Simulations Using Temperatures Measured Within An
Enclosed Array Of Heater Rods Oriented Vertically And Horizontally**

be accepted in partial fulfillment of the
requirements for the degree of

DOCTOR OF PHILOSOPHY

Dr. Miles Greiner, Advisor

Dr. Richard Wirtz, Committee Member

Dr. Chanwoo Park, Committee Member

Dr. George Fernandez, Committee Member

Dr. Nicholas Tsoulfanidis, Graduate School Representative

Marsha H. Read, Ph. D., Associate Dean, Graduate School

December,

ABSTRACT

Experiments and computational fluid dynamics/radiation heat transfer simulations of an 8×8 array of heated rods within an aluminum enclosure are performed. This configuration represents a region inside the channel of a spent boiling water reactor (BWR) fuel assembly between two consecutive spacer plates. The heater rods can be oriented horizontally or vertically to represent transport or storage conditions, respectively. The measured and simulated rod-to-wall temperature differences are compared for various heater rod power levels (100, 200, 300, 400 and 500W), gases (Helium and Nitrogen), enclosure wall temperatures, pressures (1, 2 and 3 atm) and orientations (Horizontal and Vertical) to assess the accuracy of the computational fluid dynamics (CFD) code. For analysis of spent nuclear fuel casks, it is crucial to predict the temperature of the hottest rods in an assembly to ensure that none of the fuel cladding exceeds its temperature limit.

The measured temperatures are compared to those determined using CFD code to assess the adequacy of the computer code. Simulations show that temperature gradients are much steeper near the enclosure walls than they are near the center of the heater rod array. The measured maximum heater rod temperatures are above the center of heater rod array for nitrogen experiments in both horizontal and vertical orientations, whereas for helium the maximum temperatures are at the center of heater rod array irrespective of the orientation due to the high thermal conductivity of the helium gas. The measured temperatures of rods at symmetric locations are not identical, and the difference is larger for rods close to the enclosure wall than for those far from it. Small but uncontrolled

deviations of the rod positions away from the design locations may cause these differences. For 2-inch insulated nitrogen experiment in vertical orientation with 1 atm pressure and a total heater rod power of 500 W, the maximum measured heater rod and enclosure wall temperatures are 375°C and 285°C respectively with the measured rod-to-wall temperature difference of 90°C. The simulated rod-to-wall temperature difference for this case is 91.2°C. The simulations reproduce the measured temperature profiles. The ΔT_{SIM} vs. ΔT_{MEA} for all experiments (i.e. $N = 3384$ measured/simulated temperatures), the linear regression line " $\Delta T_{\text{SIM,LR}} = 0.97\Delta T_{\text{MEA}} + 0.8^\circ\text{C}$ " shows that the simulations slightly but systematically under predict the heater rod temperatures with 95% of the simulated temperatures are within 11°C. The ΔT_{SIM} vs. ΔT_{MEA} for the hottest heater rod temperatures yields a linear regression line " $\Delta T_{\text{SIM}} = 1.01\Delta T_{\text{MEA}} - 1.1^\circ\text{C}$ " with 95% of the simulated temperatures are within 7.3°C which is 34% smaller than it was for all the temperatures. These results can be used to assess the accuracy of using simulations to design spent nuclear fuel transport and storage systems.

ACKNOWLEDGEMENTS

I would like to express my sincere gratitude to my advisor, Dr. Miles Greiner for the continuous support of my doctoral study and research, for his patience, motivation and immense knowledge. His guidance and support helped me in all time of this research and writing, especially during the tough time in building this experiment facility. I could not have imagined having a better advisor and mentor for my doctoral study.

Besides my advisor, I would like to thank the rest of my thesis committee: Dr. Richard Wirtz, Dr. Chanwoo Park, Dr. George Fernandez and Dr. Nicholas Tsoulfanidis, for their insightful comments during the committee meetings.

I would like to thank Ferrill Berendsen and Wade Cline for their help in building this experiment facility. Also, Steve and James from electrical workshop for doing all the wiring. These guys were always available whenever I needed their help.

I thank my fellow graduate students (Pablo, Venkata, Mithun and Krishna) and friends for their help.

Last but not the least, I would like to thank my parents for their continuous support.

This work was conducted with the support of DOE RW and AFC R&D.

N.R. Chalasani

TABLE OF CONTENTS

1.	INTRODUCTION	1
	1.1 Motivation	1
	1.2 Background	2
2.	RESEARCH GOALS	7
3.	EXPERIMENTAL APPARATUS AND PROCEDURE	9
	3.1 Apparatus	9
	3.2 Instrumentation	13
4.	NUMERICAL MODEL	19
	4.1 Computational Domain	19
	4.2 Boundary Conditions	21
5.	RESULTS	22
	5.1 Experimental Boundary Conditions	22
	5.1.1 Measured Enclosure Wall Temperatures	22
	5.1.2 Measured Spacer Plate Temperatures	23
	5.2 Comparison of Temperature Profiles	26
	5.2.1 Vertical Orientation	26
	5.2.2 Horizontal Orientation	29
	5.3 Statistical Comparison of Measured and Simulated Temperature Differences	31
	5.3.1 All Heater Rod Locations	31
	5.3.2 Peak Heater Rod Temperature Locations	32

6. CONCLUSIONS	34
7. FUTURE WORK	36
8. REFERENCE	39
TABLES	44
FIGURES	47
APPENDIX A – Natural Convection/Radiation Heat Transfer Simulations of an Enclosed Array of Vertical Rods	73
APPENDIX B – Benchmark of Computational Fluid Dynamics Simulations using Temperatures Measured Within Enclosed Vertical and Horizontal Arrays of Heater Rods	104

LIST OF TABLES

Table 1	Heater rod symmetry groups for horizontal orientation for determining the axial temperature profiles	44
Table 2	Heater rod symmetry groups for mid-plane temperature profiles for vertical orientation	45
Table 3	Heater rod symmetry groups for vertical orientation for determining the axial temperature profiles	45
Table 4	Number of experiments performed	46

LIST OF FIGURES

Figure 1	Photograph of 8 x 8 heater rod array and enclosure	47
Figure 2	System for fastening heater rods to spacer plates	48
Figure 3	Photograph of endplate	48
Figure 4	Photograph of the assembled apparatus	49
Figure 5	Schematic vertical axial cut view of the apparatus in Horizontal orientation	50
Figure 6	Photograph of endplates with connections	51
Figure 7	Measured emissivities	52
Figure 8	Schematic end view of apparatus with thermocouple and their locations	53
Figure 9	Schematic of heater rod symmetry groups in the mid-plane for horizontal orientation	54

Figure 10	Schematic of one-eighth rod symmetry groups in the mid-plane for vertical orientation	55
Figure 11	3-D finite volume grid	56
Figure 12	End view of computational domain	57
Figure 13	Schematic of apparatus and computational domain on free end side	58
Figure 14	Effective thermal conductivity for the gap between heater rod and spacer plate	59
Figure 15	Measured temperatures versus time (helium, 100W, 1 atm, horizontal orientation)	60
Figure 16	Average measured enclosure temperatures	61
Figure 17	Temperature difference between maximum and minimum enclosure temperatures	62
Figure 18	Average temperature difference between spacer plate and enclosure wall	63
Figure 19	Average temperature difference between the spacer plates on free and hinged ends	64
Figure 20	Temperature contours for vertical orientation with nitrogen backfill	65
Figure 21	Measured and simulated mid-plane temperature difference for vertical orientation	66
Figure 22	Measured and simulated temperature difference for the archetypical heaters in vertical orientation	67

Figure 23	Temperature contours for horizontal orientation with nitrogen backfill	68
Figure 24	Measured and simulated mid-plane temperature difference for horizontal orientation with nitrogen backfill	69
Figure 25	Measured and simulated mid-plane temperature difference for horizontal orientation with helium backfill	70
Figure 26	Simulated versus measured rod temperature difference for 72 experiments	71
Figure 27	Simulated versus measured hottest rod temperature difference for 72 experiments	72

Nomenclature

Al	= aluminum
C	= offset distance between inconel sheath and spacer plate surface
Cr	= chromel
g	= gravity
He	= helium
K_{eff}	= effective thermal conductivity
MgO	= magnesium Oxide
N_2	= nitrogen
$NiCr$	= nichrome
P	= pressure [atm]
Q	= heat Load [W]
t	= time
T	= local temperature
TIG	= Tungsten Inert Gas Arc Welding
TC	= thermocouple
T_{TOP}	= top enclosure wall temperature
T_{BOTTOM}	= bottom enclosure wall temperature
T_{RIGHT}	= right enclosure wall temperature
T_{LEFT}	= left enclosure wall temperature
$T_{Wall, Avg}$	= average temperature of twenty thermocouples on aluminum enclosure
$T_{Wall, Max}$	= maximum temperature measured on aluminum enclosure

$T_{Wall, Min}$	= minimum temperature measured on aluminum enclosure
$T_{Wall, Avg}$	= average of temperatures from twenty thermocouples on aluminum enclosure walls
$T_{Spacer, Avg}$	= average of temperatures measured from ten thermocouples, five on each spacer plate
$T_{Free, Avg}$	= average of temperatures measured from five thermocouples on spacer plate on free end
$T_{Hinged, Avg}$	= average of temperatures measured from five thermocouples on spacer plate on hinged end
$T_{Rod, Max}$	= maximum temperature at a heater location
x, y, z	= coordinate system
ΔT_{SIM}	= simulated rod to wall temperature difference
ΔT_{MEA}	= measured rod to wall temperature difference
ε	= emissivity
λ	= wavelength

CHAPTER 1

INTRODUCTION

1.1 Motivation

Light water reactor fuel assemblies (FAs) consist of zircaloy tubes held in square arrays by periodic spacer plates [1]. Boiling water reactor (BWR) FAs vary from 7x7 to 9x9 arrays, while pressurized water reactor (PWR) FAs vary from 14x14 to 18x18. The majority of tubes contain stacked uranium dioxide (UO_2) pellets. The remaining instrument sheath and guide thimble tubes are hollow. BWR assemblies have zircaloy channels around the array of fuel rods.

Spent Nuclear Fuel (SNF) is highly radioactive and continues to discharge heat after removal from the nuclear/power reactor [2]. SNF is stored under water for a period of time to allow its heat generation and radioactive decay rates to decrease. It is then moved to thick-walled casks for dry storage or offsite shipment. In the casks, individual assemblies are supported within square cross-section openings of a basket structure. The region containing the fuel and basket is evacuated and backfilled with helium or another non-oxidizing cover gas. In transport the fuel rods are oriented horizontally. In storage the packages are frequently placed so that the fuel rods are vertical.

The zircaloy cladding provides an important containment boundary and its temperature must not exceed 400°C during normal conditions [3]. Solar heat flux and heat generated by the fuel makes the package hotter than its surroundings [4, 5]. Package designers and operators must calculate the maximum or peak cladding temperature to assure that it does not exceed the allowed limit. The cask thermal dissipation capacity [6] is the fuel heat generation rate that brings the peak clad temperature to this limit. Cask

operators can use this capacity to determine how many fuel assemblies may be safely loaded into a cask, and/or how long the fuel must be aged under water in the spent fuel pool before being loaded.

1.2 Background

Finite element models of loaded packages are employed to predict cask and fuel temperatures [4, 5]. In the past, computational resources were not available to accurately model the hundreds of fuel rods within the multiple fuel assemblies (some rail and truck transport casks have room for up to 21 and 4 PWR assemblies, respectively [4, 5]). The rods and cover gas within each basket opening were therefore replaced with homogenized solid elements with a uniform heat generation rate. Temperature-dependent Effective Thermal Conductivities (ETC) were applied to these elements [4, 7, 8, 9]. They were developed to model the effects of conduction and radiation heat transfer in the directions normal to the rod axes.

Manteufel and Todreas [8] developed an analytical model for one-dimensional conduction and radiation within a rectangular array of heated fuel rods immersed in stagnant gas. They used this model to calculate a temperature-dependent ETC for the region within the fuel assembly, and a conductance model for the thin band between the assembly envelope and the basket walls. This model neglects possible two-dimensional heat transfer effects at the corners, hollow instrument sheath and guide thimble tubes, external channels, and natural convection.

Bahney and Lotz [9] performed two-dimensional finite element simulations of conduction and radiation heat transfer within the fuel assembly/cover gas region. They constructed one-quarter models of several BWR and PWR fuel assemblies. These

geometrically-accurate models included unheated instrument sheath and guide thimble tubes, and external channels. The maximum cladding temperature was determined as functions of assembly heat generation rate and basket wall temperature for an isothermal basket temperature.

A shortcoming of using thermal conductivity models to calculate temperatures within fuel assembly/cover gas regions is that they approximate heat flux at a location based only on the temperature and its spatial gradient at that location. This is not universally appropriate when thermal radiation and/or natural convection effects are significant. Radiant heat flux at a location is affected by temperatures at a distance. Natural convection is affected by the local fluid velocity, which depends on temperatures at other locations. As a result, an effective thermal conductivity that is appropriate for a basket opening whose walls are isothermal may not be accurate for openings with highly non-isothermal walls.

Current computational resources allow the use of numerical models with meshes that accurately include the many fuel rods and unheated assembly components within a cask. Canaan and Klein performed two-dimensional computational fluid dynamics (CFD) simulations of an 8×8 array of heated rods in a uniform temperature enclosure [10], and benchmarked the results using experimental temperature measurements [11]. However, their wall boundary temperatures were much cooler and more isothermal than those expected on the surface of a transport cask basket opening [6, 12, 13]. Gomez-Araya and Greiner [14, 15] conducted two-dimensional simulations of geometrically-accurate PWR and BWR assemblies within high-temperature isothermal basket openings. Those simulations used the FLUENT commercial CFD package. The simulations

determined the conditions when buoyancy induced gas motion affects peak cladding temperature, as well as the sensitivity to cladding surface emissivity and geometric variations.

Venigalla and Greiner [12] and Gudipati and Greiner [13] performed two-dimensional simulations of whole truck and rail transport cask cross sections that included geometrically accurate fuel rods in each basket opening. These simulations also used FLUENT. Simulations that included buoyancy induced cover gas motion gave temperatures that were very close to those from stagnant gas simulations (in which the gas speed was set to zero). This indicates that natural convection does not strongly affect cladding temperatures within horizontal transport cask. Results from these geometrically-accurate simulations were compared with a homogenized fuel model using the Manteufel and Todreas [8] ETCs. The geometrically accurate models predicted lower cladding temperatures and higher cask thermal dissipation capacities than the homogenized fuel models.

If the higher cask thermal dissipation capacities can be confirmed, spent fuel may not need to be aged under water for as long as indicated by the earlier homogenized models before being transferred to dry casks. The computational methods used in the geometrically accurate simulations must be benchmarked against relevant experimental data before it can be used with confidence.

Lovett [16] measured the temperature of an 8x8 array of heated horizontal rods within an aluminum enclosure. Experiments were performed for different gases in the enclosure, and for a ranges of gas pressures and rod heating rates. These conditions are similar to those of a BWR assembly within a transport cask. FLUENT simulations of the

experiments were performed that employed different assumptions regarding the thermal conditions of the endplates that held the heaters [17]. This was necessary because the endplate conditions were not completely documented. For a certain set of endplate assumptions, the simulation results accurately reproduced the experimental results.

Experiments performed by Arya and Keyhani [18, 19] measured the temperature of twelve vertical heated rods within a constant temperature, internally-finned cylindrical enclosure. Measurements were performed with air or helium in the enclosure for ranges of rod heat generation rates and gas pressures. Steady-state three-dimensional computational fluid dynamics simulations of conduction, natural convection and radiation heat transfer within the experiment were conducted to benchmark the simulation techniques [20] (This journal article is discussed in detail Appendix A). In the computational model, different thermal conductivities were applied to a spacer plate between a plate that held the heaters and one of the enclosure endplates. This was done to model a range of contact resistance between the plates. This was necessary because the experimental endplate conditions were not completely documented. The calculations accurately reproduced the local and average temperatures when a low plate conductivity (corresponding to a high contact resistance) was modeled. These results emphasize that conditions far from measurement locations can affect experimental results. Those conditions must be well documented if they are to be used to benchmark computational methods.

Experiments performed by Chalasani, Araya and Greiner [22] measured the temperature of 64 heater rods within an uniform temperature aluminum enclosure for horizontal and vertical orientation. Measurements were performed with air in the

enclosure for a range of rod heat generation rate. Steady-state three-dimensional computational fluid dynamics simulations of conduction, natural convection and radiation heat transfer within the experiment were conducted to benchmark the simulation techniques [22] (This journal article is discussed in detail Appendix B). .

CHAPTER 2

Research Goals

In the current work an experimental facility is constructed consisting of an 8x8 array of heater rods within a square cross-section aluminum enclosure. It models a section of a spent BWR assembly between consecutive spacer plates, and within the assembly channel. The rod diameter, spacing between rods, and distance from the outermost rods to the enclosure wall are all 10% smaller than the dimensions inside the channel of a GE 8x8 BWR assembly [1]. Araya and Greiner [15] performed two-dimensional CFD simulations of natural convection and radiation heat transfer for a horizontal BWR assembly within a uniform temperature basket cell. They showed that the channel surrounding the fuel rods and the gap between the channel and outer basket can be modeled analytically. As a result, only the region inside the channel is modeled in the current experiment.

The test facility can be placed so the rods are horizontal to simulate the conditions in a transport cask, or vertical to simulate storage conditions. The heater rod, spacer plate and enclosure wall temperatures are measured within the apparatus filled with nitrogen or helium, for a range of heater rod power levels (1.5, 3.1, 4.7, 6.25 and 7.8 watts/rod) and gas pressures (1, 2 and 3 atm). The measured spacer plate and aluminum wall temperatures are used as boundary conditions for CFD simulations. The measured temperatures from these experiments are compared to three-dimensional simulations including conduction, natural convection and radiation heat transfer within the same domain using the FLUENT CFD code. The goal of this work is to quantify how well the

CFD code predicts the measured temperature difference between the enclosure walls and the heater rods for all the heater rod locations and the peak heater rod temperatures.

CHAPTER 3

Experiment Apparatus and Procedure

2.1 Apparatus

Figure 1a shows the 8×8 heater rod array held by 0.635 cm thick stainless steel spacer plates at each end and a 2.54 cm thick aluminum enclosure used in the current experiment. Each rod shown in Fig. 1a is a Watlow Inc. tubular heater that is 1.1 cm in diameter and 67.3 cm long. The heater rods are made from 0.7-mm-thick Incoloy sheath with compressed magnesium oxide (MgO) powder inside. They are nearly straight, but when laid on a flat surface some heater rods exhibit gaps from bowing which are as large as 2 mm near the center. Figure 1b shows schematic axial cross section of a rod with nichrome (NiCr) heater coil inside. The ends of the heater coil are connected to metal pins that are connected to external power leads. When current passes through the rods the heat generation is nearly uniform except for 3.2 cm (1.25 inch) unheated sections on both ends (i.e. at the location of the connector pins). For the 64 heater rods, the average and standard deviation of the measured resistances are 4.0Ω and 0.12Ω respectively. The rod surface emittance as specified by the manufacturer is 0.8 also measured.

The sixty-four heaters are divided into eight sets with eight rods each in each set. The rods within each set are wired in series. These sets are then wired in parallel to a 1000 W regulated DC power supply (HP 6218B). Experiments are performed for total heat generation rates of $Q = 100, 200, 300, 400$ and 500 Watts (1.5, 3.1, 4.7, 6.2 and 7.8 watts/rod). The heat generated from each rod is same within a $\pm 3\%$ uncertainty.

The enclosure is constructed by tungsten inert gas (TIG) welding of four 2.54-cm thick aluminum plates. The length of the aluminum enclosure is 91.44 cm and its interior

width and height are 12 cm with a tolerance of 0.25 cm. Five thermocouple wells are drilled into the outside of each enclosure wall for measuring the temperature of enclosure. Each thermocouple well is 2.3 cm deep i.e. 0.25 cm away from the inner surface of the enclosure. All the five thermocouple wells are located on the axial and mid-plane centerlines to measure the temperature gradient of each wall.

Thirty three of the 47 instrumented heater rods have a type-K (chromel/alumel) thermocouple at their mid-planes and fourteen at other axial locations. The type-K thermocouples are constructed by inserting a chromel rod into one end that is roughly half as long as the heater rod as shown in Fig. 1b. A thermocouple junction is formed by wrapping an alumel wire around the end of the chromel rod. The other end of the alumel wire is connected to an alumel pin at the end of the heater. Thermocouple lead wires are connected to the chromel rod and alumel pin. In instrumented heater rods, both the heater and thermocouple are offset from the rod centerline. The heater coil is centered in heater rods that do not contain thermocouples. The positions of the heater coils and thermocouple junctions are not specified by the manufacturer, so their exact location and variation from rod to rod is not known.

Figure 2a is a schematic of the stainless steel spacer plate with 1.15 cm diameter holes, heater rods are in contact with the bottom of the holes in the spacer plate and a tapered open ring with a bolt. A tolerance of 10 mm to the hole allows the heater to be inserted into the spacer plate freely without any friction. The tapered open ring and bolt arrangement is used to avoid any sliding of the heaters when the apparatus is in vertical orientation. Figure 2b shows the schematic of the bolt screwed to the spacer plate with the tapered opened ring, the ring expands when the bolt is screwed against the tapered

edge of the ring and push the heaters against the holes in the spacer plates not allowing the heaters to slide.

The heater rod array is slid into the enclosure leaving a 12 cm gap on either side of the array when the array and enclosure centers are at the same axial location. Figure 3a shows an endplate with an O-Ring, two holes for the thermocouple feedthrough/power supply and twelve holes for the bolts. The O-ring is made of Kalrez Perfluoroelastomer with a limit temperature of 315°C (\$400/O-Ring) used for sealing the apparatus for pressure and vacuum experiments. The two holes for the feedthrough's are used for taking the thermocouple and lead wires out of the apparatus to the data acquisition system. After making the connections, endplate is bolted against the enclosure on the free end using the twelve holes on the endplate. Another endplate of the same dimensions, O-Ring and holes are used for the hinged end of the enclosure, except that one hole is used for the thermocouple feedthrough and the other hole is used for a connector tube. The connector tube is used to either backfill the aluminum enclosure with the appropriate gas to the required pressure or removing gas from the enclosure and is connected with an atmospheric valve, evacuation valve, oil filter and an evacuation tube connected to the vacuum pump. The connector tube is also instrumented with a low pressure and high pressure gages.

Figure 3b shows the gap on the either side of the array inside the enclosure and is mostly used for the connections and storage of the lead and thermocouples wires from the heaters. All wires inside the enclosure are insulated with fiberglass insulation. The thermocouple and lead wires from the heater array are connected to the respective wires on the feedthrough's making a big cluster of wires in the gap leaving very little space.

Figure 4a shows the experimental apparatus without exterior insulation on a hinged test stand in horizontal orientation. Hinged end of the apparatus is the end at which the apparatus is fixed to the test stand, while the other end of the apparatus is called free end. The test stand is altered and built from the chassis of a desk removing the wooden plank from the top. In horizontal orientation, the free end of the apparatus rests on an insulation sheet fixed to the stand. An aluminum plate is bolted to the bottom end of the endplate on the hinged end of the apparatus with an insulation sheet between the endplate and aluminum sheet (white plate shown in Fig. 4a). The aluminum plate is then bolted to an iron cross bar on the test stand which enables the apparatus to swivel and stand in a vertical orientation. Figure 4b shows the experimental apparatus on the test stand in vertical orientation with the hinged and free ends indicated. When the apparatus is in vertical orientation, the upper portion of the endplate on the hinged end rests on another iron cross bar which is detachable from the stand. The circles shown in the figures are locations where type-K thermocouple probes (Watlow Insulated thermocouples) are inserted into thermocouple wells in the enclosure. Figure 4c shows the apparatus in vertical orientation with insulation.

Figure 5 shows a schematic axial cross section of experimental apparatus in horizontal orientation with hinged and free ends. The total length of the apparatus is 91.44 cm. The thermocouples in heater rods at mid-plane and other axial locations are at $Z = -17.3, 0, 17.3$ and 29.2 cm. The gaps between the heater array and the endplates are filled with thermocouple and lead wire connections to the thermocouple feedthrough's.

Figure 6a shows photograph of endplate and external components on free end. The endplate on the free end has two holes for two thermocouple feedthrough's. Ceramic

feedthrough (thermocouple wire and power lead wires) with a short tube has high temperature (635°C) limit, whereas the epoxy feedthrough (all thermocouple wires) has a long tube fitting to compensate for its low temperature (140°C) limit. Figure 6b shows photograph of endplate along with external components on hinged end. The endplate on hinged end has two holes, one for the thermocouple feedthrough and the other for the connector tube.

Figure 7 shows average measured (three measurements) emissivity of inconel sheath from Watlow tubular heater rod and anodized black dye aluminum enclosure samples for different angles (20° and 60° from normal) as a function of wavelength range. Emissivities were measured using a SOC 410C DHR Reflectometer with an uncertainty of ± 0.03 at Sandia National Laboratory. These measured emissivities are used in the CFD analysis for benchmarking measured data. All CFD simulation results presented in this work have $\epsilon_{\text{Enclosure}} = 0.7$, $\epsilon_{\text{Heater Rod}} = 0.8$.

The apparatus is tested for leak using a helium leak testing device after assembling and fixing to the stand. The leak rate determined from the test is 2×10^{-10} cm³/sec.

2.2 Instrumentation

Figure 8a is a schematic of end view of experimental apparatus showing 64 heater rods (circles), 2.5 cm thick aluminum enclosure walls, 2.3 cm deep thermocouple wells and TIG welding locations. Textured circles are the heater rods that are instrumented with thermocouples. Open circles are the heater rods with no thermocouples. This pattern of heater rod arrangement in the array is chosen to take the advantage of half and quarter

symmetry of the horizontal and vertical orientations respectively. Heater rod columns and rows are labeled 1 through 8 and A through H respectively. The five X's shown are the locations of type-K Watlow grommet-terminal surface thermocouples on the spacer plates. The direction of the gravity vector shows that the orientation of the apparatus is in horizontal orientation. Figure 8b shows a table of z location of the thermocouple for each heater rod texture in fig 8a. Thirty three of the 47 textured heater rods are chosen to have thermocouples at the mid plane ($z = 0$) for determining the temperature profiles of the heater columns 1 through 8 for horizontal experiments. Fourteen textured heater rods with thermocouples at different axial locations ($z = -17.3, 17.3$ and 29.2) are chosen to determine axial temperature profiles of these heaters along with mid plane temperatures. Heater rods with thermocouples at $z = -17.3$ and 17.3 are same, but inverted while assembling the apparatus to avoid the setup charges from the manufacturer for two heater rods ($z = -17.3$ and 17.3) instead of one.

When apparatus is in horizontal orientation, the measured temperatures are expected to be nearly equal at pairs of heater rods that are located symmetrically across the plane mid-way ($z = 0$) between heater rod columns 4 and 5 (Fig. 8a). For example, the temperatures measured in heater rods C4 and C5 (see row letters and column numbers in Fig. 8a) are expected to be nearly the same. Hence the columns in Fig. 9 are labeled 1&8 through 4&5, where 1&8 shows the heater rods from column 1 and 8 combined. Heater rods with thermocouples at different z-locations are not shown. Circles in these columns with 2 indicate that, both the heater rods in the symmetry location are instrumented, 1 denotes for symmetry pair that has only one heater rod instrumented and open circles are shown for the symmetry pair where both the heater rods are not instrumented. For

horizontal experiments with nitrogen as cover gas, maximum temperatures are expected to be above the center of the heater rod array due to buoyancy induced gas motion and hence the upper part of the combined columns are all instrumented except two heater rods to fully understand the temperature distribution at these locations. Heater rods with thermocouples at different z -locations are grouped together to determine the temperature profile of a archetypical heater rod in the assembly. Table 1 shows the symmetry groups for horizontal orientation of heater rods with thermocouples at different z -locations for determining the axial temperature profiles. A total of eight symmetry groups are listed in the table R1 through R8. For example, symmetry group R4 consists of heater rods D4 and D5. From Fig. 8a., heater D4 is instrumented with a thermocouple at $z = 0$ and D5 at $z = 29.2$ cm. Temperatures measured from both these heater rods are used to determine the temperature profile of archetypical heater rod R4.

When the apparatus is in vertical orientation, near symmetry is expected across that plane, the plane midway between rows D and E, and the diagonal plane (the planes connecting rods A1 and H8, and connecting rods A8 and H1). Fig. 10a shows the bottom right part of the symmetry of Fig. 8a when the apparatus is in vertical orientation at $z = 0$. For vertical orientation the heater rods may be broken into ten symmetry group. Table 2 shows the name of each group, the heater rods in each, and the name and number of heater rods in each group that are instrumented with thermocouples. The archetypical heater rod for each group is also shown in Fig. 10a. Similarly, for heater rods instrumented with thermocouples at different z -locations are also grouped together as shown in Table 3 to determine the vertical temperature profile of a archetypical heater rod. If the experimental configuration (geometry and boundary conditions) is perfectly

realized, and there are no measurement errors, then all the measured temperatures within each symmetry group will be the same.

However, some factors of the experimental configuration are not rigidly controlled and may disturb this symmetry. These factors include non-uniformity of the heater rod spacing (due to heater rod curvature, the enclosure wall temperature, clearance between heater rod and endplate holes, and non-uniformity of the enclosure inner dimensions); the rod heat generation rate (due to differences in heater rod resistance), the heater rod and enclosure surface emittance; as well as variation of the apparatus from vertical or horizontal alignment. Variations of temperatures within each symmetry group are also caused by random measurement errors. The apparatus was designed so that the heater rods with thermocouples are positioned to measure temperatures of the expected hottest and coldest heater rods, and so that multiple measurements are made within each symmetry group.

The apparatus has a total of 83 thermocouples (47 in the heater rods, 22 in aluminum enclosure walls, 10 on the spacer plates and 4 on the endplates). All the alumel wires from the heater rods and the surface thermocouples on the spacer plate at the hinged end of the apparatus were connected together and a alumel wire from this group is connected to data acquisition to a individual negative input terminal (all the negative input terminals on the data acquisition are connected in a loop) via. the feedthrough on the endplate except the four heater rods ($Z = -17.32$ cm) that are inverted. The chromel wires from the inverted heater rods and the surface thermocouples on the spacer plate are connected to the data acquisition positive input terminals. Similarly, on the free end of the apparatus, the chromel wires from the heater rods, surface thermocouples on the spacer

plate are connected to the positive input terminals of the data acquisition system through the ceramic and epoxy feedthrough, while the alumel wires from the inverted heater rods and surface thermocouples are connected together and a single wire from this group is connected to the negative input terminal of the data acquisition system.

Table 4 shows the 72 experiments that were performed in this study for various insulation layers, gases, pressures, apparatus orientation and rod heat generation rates. All 72 experiments are primarily grouped into three categories based on the layers of insulation on the apparatus, i.e., no-insulation, 2.5 cm thick insulation and 5 cm thick insulation.

Experiments in the no-insulation category are performed with the apparatus covered with 2.5 cm thick Fiberfrax insulation sheets on enclosure aluminum walls. Stainless steel endplates, thermocouple feedthrough's and instrument tube are not insulated. Thirty experiments are performed with this setup. All 30 experiments are performed with nitrogen backfill for both horizontal and vertical orientations for 1,2 and 3 atm enclosure pressure and heat generation rates of 100 W, 200 W, 300 W, 400 W and 500 W.

Experiments in 2.5 cm thick insulation category are performed with apparatus covered with 2.5 cm thick Fiberfrax insulation sheets on enclosure aluminum walls, stainless steel endplates, thermocouple feedthrough's and 2.5 cm thick Isofrax insulation blanket on connector tube. Thirty six experiments are performed with this setup for both helium and nitrogen backfill, horizontal and vertical orientations for 1, 2 and 3 atm enclosure pressures and heat generation rates of 100 W, 300 W and 500 W.

Experiments in 5 cm thick insulation category are performed with apparatus covered with 2.5 cm thick Isofrax insulation blanket on existing 2.5 cm thick insulation Fiberfrax sheets. Six experiments are performed with this setup in vertical orientation for helium and nitrogen backfills at 1 atm pressure for 100 W, 300 W and 500 W. The 5 cm insulation is used to elevate the enclosure wall temperatures close to 300°C.

CHAPTER 4

NUMERICAL MODEL

4.1 Computational Domain

Figure 11 shows the three dimensional finite volume computational mesh and coordinate system used in this work. Three meshes (coarse, nominal and fine) were created using MSC/PATRAN mesh generator. This domain includes the region between the spacer plates. Since the temperatures in the enclosure aluminum walls are measured at 0.25 cm away from the inner surface, only a 0.25 cm thick aluminum wall is modeled in the mesh domain instead of a 2.5 cm thick enclosure aluminum wall in the apparatus. The dimensions and emissivities given in Apparatus section, and temperature-dependent properties of the indicated materials were applied to the numerical model. The region of the heater rods that protrudes outside the spacer plate, region between the spacer and endplates and localized heater coil are not modeled in the domain (heat is generated uniformly throughout the heater). Variations due to rod curvature are also not included.

Conduction, natural convection and radiation heat transfer within the domain are simulated using the FLUENT commercial computational fluid dynamics (CFD) package (version 6.3.26). FLUENT solves for conservation of mass, momentum and energy equations using a finite-volume method with discretized governing equations. Pressure-velocity coupling is solved using the SIMPLE method. The computational mesh created using MSC/PATRAN is imported to FLUENT and the governing equations are solved with double precision. Steady solver and a second-order upwind scheme are used for the momentum and energy equations. The buoyancy-induced flow is generated by adding gravitational acceleration (9.81 m/s^2) in the $-y$ or $-z$ directions for the horizontal or

vertical orientation, respectively. The temperature-dependent gas density is included in the natural convection calculation to model buoyancy. Radiation is solved for gray diffuse surfaces using the discrete ordinates method.

Figure 12a shows an end-view of the computational domain with coarse mesh. The spacer plates in the computational domain are divided into nine parts as shown. X's show the location of the temperatures measured on the spacer plates whereas solid dots show the locations of temperatures measured on the aluminum enclosure walls. Taking advantage of the half and quarter symmetry for horizontal and vertical orientations respectively, the temperatures measured on the spacer plates are applied independently for each of the nine parts. Figures 12b and 12c show the nominal (174,928 elements) and fine (330,167 elements) meshes. All computational results presented in this work use the coarse mesh. Computational results using nominal/fine mesh (not included in this work) are within 0.16°C of the results with the coarse mesh.

Figure 13a shows a schematic of free end of the experimental apparatus with heater rods protruding out of the spacer plate, the wire connections and the gap between the heater and spacer plate. The 3.1 cm unheated end region of the heater is in contact with the spacer and protruding outside the spacer plate. Figure 13b shows a schematic of computational domain on the free end as modeled. Since, the regions between the spacers on the free and hinged ends are only modeled in the computational domain, the rod ends (Insulated Rod Ends) and the ends of the gaps between the spacer and heater rods (Insulated Gap Ends) are insulated. An effective thermal conductivity (K_{Eff}) is calculated for the inconel sheath of the heater and the gap between the sheath and the spacer plate as they are modeled as solid elements.

Figure 14a shows a numerical model used for calculating the effective thermal conductivity of the gap between the spacer plate and the inconel sheath. The domain shown has a heater rod surrounded by inconel sheath and a gap between the spacer and sheath (Offset Distance, C). Three domains with different offset distances are used to calculate the effective thermal conductivity. K_{Eff} is calculated for a range of sheath and spacer temperatures. Figure 14b shows effective thermal conductivity versus offset distance. As expected the effective thermal conductivity increases as the offset distance decreases and tends to be infinite when $C = 0$. In the current work an effective thermal conductivity of $13.87 \text{ W/m}^2\text{K}$ is used for the simulations with $C = 0.135 \text{ mm}$.

4.2 Boundary Conditions

Figure 15 shows the measured thermocouple temperatures (total of 83 thermocouples - placed within enclosure walls, spacer plates and heater rods) versus time for $Q = 100 \text{ W}$ (1.5 W/rod) with the apparatus filled with helium at 1 atm pressure in horizontal orientation. The initial temperature of all the thermocouples is same as the ambient room temperature around 23°C . All temperatures increase until a steady state is reached at approximately 25 hours. Then, to acquire temperature data, experiment is continued at a steady state. The total time for the experiment is 28 hours. The data for the 3 hours after steady state is time averaged. Once time averaged data is acquired for each wall thermocouple, the time averaged data from the five thermocouples on enclosure walls are again averaged to obtain the final average enclosure wall temperature. The final average enclosure wall temperature is later used as temperature boundary condition for the CFD domain.

CHAPTER 5

RESULTS

5.1 Experimental Boundary Conditions

5.1.1 Measured Enclosure Wall Temperatures

Figure 16 shows average temperatures on all four enclosure walls as a function of heat load for no-insulation, 2.5 cm insulation and 5 cm insulation experiments. Each of these experiment categories are explained in Table 3. The maximum average enclosure temperature measured for no-insulation, 2.5 cm insulation and 5 cm insulation experiments are 193°C, 222 °C and 280°C. The average enclosure temperature increases with heat generation rate and the thickness of the insulation enclosing the apparatus. Even though each of the experiment category have experiments performed with either helium or nitrogen backfill, horizontal and vertical orientation for different pressures, they exhibit similar average temperatures. For example, 2.5 cm insulation has a total of 36 experiments performed for both nitrogen and helium backfill, horizontal and vertical orientations and different pressures (1, 2 and 3 atm), the difference between the average enclosure temperatures of all the experiments at 500 W is 11°C. A rise of 29°C is observed between the no-insulation and 2.5 cm insulation experiments, which quantifies the heat losses through the endplates when not insulated.

Figure 17a shows the difference between the maximum and minimum temperatures of all the 20 (five on each wall) temperatures measured on the four enclosure walls for no-insulation (Nitrogen, $P = 1, 2$ and 3 atm, horizontal and vertical orientation) experiments at 100, 200, 300, 400 and 500 Watts. The difference between the maximum and minimum enclosure temperatures increases with Q and are higher for

vertical experiments compared to horizontal. This is due to the high temperature gradient in the enclosure walls for vertical experiments due to buoyancy induced gas motion. The temperature differences tends to increase with pressure and are almost identical for pressures at 2 and 3 atm for horizontal orientation and 1 atm for vertical orientation. Figure 17b also shows the difference between the maximum and minimum temperatures of enclosure walls for 2.5 cm insulation (Nitrogen and helium, $P = 1, 2$ and 3 atm, horizontal and vertical orientation) experiments at 100, 300 and 500 Watts. The 2.5 cm insulation experiments with nitrogen backfill also exhibit the same trends discussed for Fig 17a. For helium, the wall temperature differences are almost identical irrespective of the pressure and orientation. This is due to the absence of buoyancy induced gas motion , because helium has high thermal conductivity. Figure 17c shows the difference between the maximum and minimum temperatures of enclosure walls for 5 cm insulation (Nitrogen and helium, 1 atm, horizontal and vertical orientation) experiments and as discussed above, the temperature differences for helium are lower compared to nitrogen experiments.

5.1.2 Measured Spacer Plate Temperatures

Figure 18a shows the average temperature of the spacer plates (averaged temperature of 10 thermocouples, five on each spacer plate) minus the average temperature of the enclosure walls for 100, 200, 300, 400 and 500 Watts for experiments with no-insulation. The solid and dotted lines represent the horizontal and the vertical experiments respectively. Since, the heaters are in direct contact with the spacer plates, the average temperatures are always higher compared to the enclosure walls. The average

temperature difference increases with Q , but decreases with increase in pressure. This is due to the buoyancy induced gas motion inside the apparatus (increased velocity). The vertical experiments for 1 atm and 2 atm pressures exhibit higher average temperature difference compared to the horizontal experiments except for 3 atm pressure. Further, the decrease in temperature difference is larger from 2 atm to 3 atm than from 1 atm to 2 atm for vertical experiments compared to the horizontal experiments. This is due to the increased gas motion inside the apparatus at 3 atm pressure.

Figure 18b shows the average temperature difference between the Spacer plate and enclosure walls for experiments with "2.5 cm insulation" at 100, 300 and 500 Watts. Unlike the "no-insulation" experiments with nitrogen backfill, all the vertical experiments have larger temperature differences compared to the horizontal experiments (Figure 18b shows that the average temperature difference for 3 atm vertical experiments is lower than 3 atm horizontal experiments). This is because; buoyancy effect tends to decrease as the enclosure wall temperatures increase. For experiments with helium backfill, the average temperature differences are almost identical irrespective of the pressure and orientation of the apparatus. This is due to the absence of buoyancy induced gas motion, because helium has high thermal conductivity. Figure 18c shows the average temperature differences for experiments with "5 cm insulation", the temperature differences with nitrogen backfill are higher compared to helium backfill.

Figure 19a shows the average temperature of spacer plate (5 thermocouples) on the free end minus the average temperature of the spacer plate (5 thermocouples) on the hinged end of the apparatus at 100, 200, 300, 400 and 500 Watts for no-insulation experiments. The average temperatures of spacer plate on the free end of the apparatus

are always higher than the spacer plate on the hinged end for both horizontal and vertical experiments. Since, the cross-section areas for buoyancy induced gas motion is larger in vertical experiments compared to horizontal experiments, the average temperature differences are larger for vertical than the horizontal experiments. For Vertical experiments, the average temperature differences increases with Q and are identical for 2 and 3 atm pressure experiments whereas the average temperature difference for 1 atm pressure experiment also increases with Q only up to 300 Watts but remains constant thereafter. This is due to the decrease in gas motion at lower pressures and high rod heat generation rates, where radiation heat transfer tends to overtake convection heat transfer. For horizontal experiments, the average temperature differences are expected to be zero due to symmetry in the apparatus, but increases with Q . This may be due to the experimental and random errors in the apparatus. Fig 19b shows the average temperature difference between the free and hinged spacer plates for 2.5 cm insulation experiments at 100, 300 and 500 Watts. The average temperature differences show the same trends for nitrogen experiments as in Fig. 19a. For horizontal and vertical experiments with helium backfill, the average temperature differences are expected to be negligible due to the apparatus symmetry in horizontal orientation and the high thermal conductivity of helium. But, the maximum difference in average temperature in the helium backfill experiments is 8°C due to the experimental and random errors in the apparatus. Figure 19c show the average temperature difference between the free and hinged end spacer plates for 5 cm insulation experiments.

The measured average enclosure wall temperatures are imposed as isothermal boundary conditions to the top, left, right and bottom enclosure walls in CFD simulation

model as shown in Fig. 11. Whereas the measured spacer plate (five on each spacer plate) temperatures are imposed on respective spacer plate grids in CFD simulation model using the horizontal and vertical symmetry of the apparatus as shown in Fig.12. Heat is generated uniformly inside the heater instead of a localized heater coil (NiCr coil). Temperature dependent thermophysical properties are used for all the materials (Aluminum, MgO, Inconel, Stainless Steel Helium and Nitrogen) in CFD simulation model. The values of surface emissivity for enclosure walls and heater rods are taken from their respective measurements shown in Fig. 7.

5.2 Comparison of Temperature Profiles

5.2.1 Vertical Orientation

Figure 20 shows CFD simulation results with nitrogen backfill at 3 atm pressure for 500 Watts with 2.5 cm insulation in vertical orientation. Figure 20a shows enclosure, gas and rod temperature contours at mid-plane between the spacer plates with the maximum temperature at the center of the domain, while Fig. 20b shows temperature contour and velocity vectors in the vertical mid-plane. The velocity vectors in Fig. 20b show that the buoyancy induces an upward gas motion in the vertical mid-plane of the domain and downwards near the enclosure walls. As a result the maximum temperatures are above the domain center in the vertical mid-plane.

Figure 21 shows measured (symbols) and simulated (lines) rod-to-wall temperature difference for a "2.5 cm insulation" vertical experiment with nitrogen backfill of 3 atm pressure at 500 Watts. Results are presented for each symmetry group (described in Table 2) versus x-location of the archetypical heater rod for that group.

Ovals enclose data when more than two measurements were acquired at their symmetric locations. The simulations show the rods are nearly isothermal and relatively large temperature gradients exist in the space between the heater rods. All the temperature measurements at groups S1, S2, S3 and S4 are from the heater rods near the enclosure walls, where group S4 comprise of seven heater rods (A4, A5, D1, D8, E1, H4 and H5) with the largest difference between the measurements of 20°C.

As discussed earlier, differences between measurements at symmetric locations are caused by both random measurement errors and uncontrolled aspects of the apparatus (configuration errors). For all no-insulation, 2.5 cm insulation and 5 cm insulation vertical experiments with nitrogen backfill, the largest difference in temperature measurements between symmetric locations is in group S4 near the enclosure wall. For $Q = 500 \text{ W}$, $P = 3 \text{ atm}$, the difference is 20°C. The differences are significantly smaller at other positions, and they decrease as the heat generation rate decreases. We note that the simulated temperature profiles exhibits very steep gradients near the walls. As a result, displacements of the near-wall heater rods from their design location of 0.7 to 1.0 mm have the potential to cause large variation in temperatures among symmetry group.

The rods in symmetry group S9 near $x = 5.2 \text{ cm}$ (Rods C4 and C5) are near the center of the domain. The measurements from this symmetric pair are very close. Since, the simulated temperature profiles exhibits much smaller temperature gradients in the vicinity of these heater rods than they do near the walls, small position variations of these rods are not expected to cause as large a temperature variation as they would for rods near the walls.

The simulated rod-to-wall temperature difference follows the measured temperature profiles. The simulations over predict the maximum measured temperature difference (in symmetry group S10) by 5°C.

Figure 22a shows measured (symbols) and simulated (lines) rod-to-wall temperature difference for the archetypical heater rods for a "2.5 cm insulation" vertical experiment with nitrogen backfill of 3 atm pressure at 500 Watts. Results are shown for each symmetry group (described in Table 3) versus the z-location (along the length of the heater rod) of the archetypical heater rod for that group. Symmetry group S11 contains heater rods that are near the enclosure walls.

Maximum temperature difference is above the center of the domain due to the buoyancy induced gas motion inside the apparatus as observed in Figure 20. The rods in symmetry group S14 are at the center of the domain and exhibit the hottest temperatures measured. Measured temperatures difference in symmetry group S13 has a symmetry pair for every heater rod in its group as shown in Figure 8a and Table 3. The measurements are too close to identify the difference between them and hence can be seen as a single symbol.

Symmetry group S11 has heater rods near to the two enclosure walls (all four heaters are at the four corners of the heater rod array, figure 8a), where a small displacement in the heater rod would effect the temperature measurement as the temperature gradient from the enclosure wall to the nearest heater rod very steep. The X's shown are the temperature measured on the free and hinged spacer plates. Temperatures of the spacers on the free end are hotter than the hinged end, due to the buoyancy induced gas motion (described in Fig. 19). Also, the enclosure wall and endplate temperatures are

effected due to the buoyancy induced gas motion. The temperatures measured at the thermocouple locations near the hinged end are lower compared to the temperatures measured at the locations near the free end.

The CFD simulations accurately predict the temperature measurements at $z = 0$, 17.3 and 29.2 cm, but, over predict at $z = -17.3$ cm near the hinged end for the symmetry groups S12, S13 and S14. However, for the symmetry group S11, the simulations under predict at the top and under-predict at $z = 0$, 17.3 and 29.2 cm and over predict at $z = -17.3$ cm. This is due the heater rods in group S11 are all near the walls as described earlier.

Figure 22b shows measured (symbols) and simulated (lines) rod-to-wall temperature difference for the archetypical heater rods for a "2.5 cm insulation" vertical experiment with helium backfill of 3 atm pressure at 500 Watts. Since helium has higher thermal conductivity compared to nitrogen, there is no buoyancy induced gas motion. Hence, the hottest temperatures are at the center of the domain.

5.2.2 Horizontal Orientation

Figure 23 shows CFD simulation results for a "2.5 cm insulation" horizontal experiment with nitrogen backfill of 3 atm pressure at 500 Watts. Fig. 23a shows enclosure walls, as and rod temperature contours and velocity vectors at mid-plane between the spacer plates. The velocity vectors show that the buoyancy induced upward gas motion in the center of the domain and downward near the enclosure walls. The maximum temperatures are above the domain center. Fig. 23b shows the temperature

contours at the axial mid plane between the enclosure walls (y-z plane). The maximum temperatures are above the center of the domain.

Figure 24 shows measured (symbols) and simulated (lines) rod-to-wall temperature difference for a "2.5 cm insulation" horizontal experiment with nitrogen backfill of 3 atm pressure at 500 Watts. The temperature difference between each heater rod location and the coolest temperature on the enclosure walls, $\Delta T = T(y) - T_{WALL,MIN}$, is plotted versus elevation above the bottom enclosure wall, y . The lines show the temperature difference along vertical lines that bisect the rod columns described in Fig. 9. To reduce crowding, the temperature differences from columns 1&8 and 3&6 are shown in Fig. 24a and those from columns 2&7 and 4&5 are shown in Fig. 24b. Ovals enclose data when more than two temperature measurements were acquired from a symmetry pair. As discussed earlier, the difference in temperature difference between the heater rods in a symmetry pair are due to the random measurement errors and uncontrolled aspects of the apparatus (configuration errors). For all the "2.5 cm insulation" horizontal experiments, the maximum deviation in the temperature difference of a symmetry pair is 8.5°C and is significantly smaller at other y -locations. As described earlier for Fig. 21, the simulated temperature difference profiles for the heater rod columns exhibit steep gradients near the enclosure walls

The maximum temperature difference is at $y = 0.8$ cm in column 4&5 in Fig. 24b and are near the center of the domain. This is due to the buoyancy induced gas motion as shown in Fig. 23. The difference between the temperature differences of the heater rods at this symmetry location is 0.2°C. Simulations over predict measured temperature data for columns 4&5 and 3&6. CFD simulations predict measured data accurately.

Figure 25 shows measured (symbols) and simulated (lines) rod-to-wall temperature difference for a "2.5 cm insulation" horizontal experiment with helium backfill of 3 atm pressure at 500 Watts. Unlike the nitrogen backfill experiments, the buoyancy induced gas motion for helium backfill experiments is smaller due to the high thermal conductivity of helium and hence, the maximum rod-to-wall temperature difference is always at the center of the domain (D4 and D5, $y = 5.2$ cm and 6.6 cm). The simulated rod-to-wall temperature difference follows the measured temperature profiles.

5.3 Statistical Comparison of Simulated and Measured Temperature Differences

5.3.1 All Heater Rod Locations

Figure 26 is a plot of the simulated rod-to-wall temperature difference versus the measured value. Results are given for all 47 measured rods, all three heat generation rates, helium and nitrogen backfill and both the horizontal and vertical rod orientations, totally $N = 3384$ measurement/simulation results. If the simulations modeled the experiment and its measurement errors perfectly, all data would lie on the line marked $\Delta T_{\text{SIM}} = \Delta T_{\text{MEA}}$.

Linear regression gives the line marked " $\Delta T_{\text{SIM,LR}} = 0.97\Delta T_{\text{MEA}} + 0.8^\circ\text{C}$." Systematic errors in the simulation and measurement methods, and in the experimental configuration cause this line to deviate from $\Delta T_{\text{SIM}} = \Delta T_{\text{MEA}}$. The regression line shows that, on average, the simulations slightly but systematically under-predict the higher temperatures, but accurately predict the lower ones.

The actual measurement/simulation results in Fig. 26, $(\Delta T_{\text{SIM},i}, \Delta T_{\text{MEA},i})$ for $i = 1$ to N , deviate somewhat randomly from that line. This is caused by random error in the

simulations, experiment and apparatus configuration. The standard deviation of the *output* describes the vertical deviation of the data from the fit line and quantifies the random errors. It is defined as [21]

$$S_o = \sqrt{\frac{\sum_{i=1}^N [(0.97\Delta T_{MEA,i} + 0.8^\circ C) - \Delta T_{SIM,i}]^2}{N - 2}}$$

For the data in Fig. 26, $S_o = 5.53^\circ C$. We therefore expect that 95% of the simulated results are within $2S_o = 11^\circ C$ of the linear regression correlation.

5.3.2 Peak Heater Rod Temperature Locations

For analysis of spent nuclear fuel casks, it is crucial to predict the temperature of the hottest rods in an assembly to ensure that none of the fuel cladding exceeds its temperature limit. The dashed line shown in Fig. 27 " $\Delta T_{SIM} = 1.01\Delta T_{MEA} - 1.1^\circ C$ " shows linear regression correlation for the hottest heater rods. When using the current simulation methods, the best estimate for the maximum rod temperature is determined from the simulated value ΔT_{SIM} by inverting the regression correlation: $\Delta T = 0.98\Delta T_{SIM} + 1.1^\circ C$.

The data in Fig. 27 show that the deviations of the data of the hottest heater rods in the assembly from the linear regression line are smaller than the deviations of the full

data set from its regression correlation. Based on the standard deviation of the output, 95% of the data for the hottest heater rods are within $2 S_O = 7.3^\circ\text{C}$. of the regression correlation, which is 34% smaller than it was for the full data set. This may be because the hottest heater rods are at the center of the domain where the temperature gradients are low. As a results, the measured temperatures are not as sensitive to the variations of the rod position as they are at the other locations.

CHAPTER 6

CONCLUSIONS

Experiments and computational fluid dynamics/radiation heat transfer simulations of an 8×8 array of heated rods within an aluminum enclosure are performed. This configuration represents a region inside the channel of a spent boiling water reactor (BWR) fuel assembly between two consecutive spacer plates. The heater rods can be oriented horizontally or vertically to represent transport or storage conditions, respectively. The measured and simulated rod-to-wall temperature differences are compared for various heater rod power levels (100, 200, 300, 400 and 500W), gases (Helium and Nitrogen), enclosure wall temperatures, pressures (1, 2 and 3 atm) and orientations (Horizontal and Vertical) to assess the accuracy of the computational fluid dynamics (CFD) code. For analysis of spent nuclear fuel casks, it is crucial to predict the temperature of the hottest rods in an assembly to ensure that none of the fuel cladding exceeds its temperature limit.

The measured temperatures are compared to those determined using CFD code to assess the adequacy of the computer code. Simulations show that temperature gradients are much steeper near the enclosure walls than they are near the center of the heater rod array. The measured maximum heater rod temperatures are above the center of heater rod array for nitrogen experiments in both horizontal and vertical orientations, whereas for helium the maximum temperatures are at the center of heater rod array irrespective of the orientation due to the high thermal conductivity of the helium gas. The measured temperatures of rods at symmetric locations are not identical, and the difference is larger for rods close to the enclosure wall than for those far from it. Small but uncontrolled

deviations of the rod positions away from the design locations may cause these differences. For 2-inch insulated nitrogen experiment in vertical orientation with 1 atm pressure and a total heater rod power of 500 W, the maximum measured heater rod and enclosure wall temperatures are 375°C and 285°C respectively with the measured rod-to-wall temperature difference of 90°C. The simulated rod-to-wall temperature difference for this case is 91.2°C. The simulations reproduce the measured temperature profiles. The ΔT_{SIM} vs. ΔT_{MEA} for all experiments (i.e. N = 3384 measured/simulated temperatures), the linear regression line " $\Delta T_{\text{SIM,LR}} = 0.97\Delta T_{\text{MEA}} + 0.8^\circ\text{C}$ " shows that the simulations slightly but systematically under predict the heater rod temperatures with 95% of the simulated temperatures are within 11°C. The ΔT_{SIM} vs. ΔT_{MEA} for the hottest heater rod temperatures yields a linear regression line " $\Delta T_{\text{SIM}} = 1.01\Delta T_{\text{MEA}} - 1.1^\circ\text{C}$ " with 95% of the simulated temperatures are within 7.3°C which is 34% smaller than it was for all the temperatures. These results can be used to assess the accuracy of using simulations to design spent nuclear fuel transport and storage systems.

FUTURE WORK

The current work has quantified the accuracy of simulations that use computation fluid dynamics (CFD) with surface-to-surface radiation for predicting temperatures of spent nuclear fuel assemblies in horizontal transport and vertical storage configurations. To do this the simulation results were benchmarked against experimental data for a rectangular array of heated rods in a nearly uniform temperature enclosure, with different high and low thermal conductivity cover gases at a range of pressures, and with the rods in both horizontal and vertical orientations. The CFD calculations include the effect of conduction within the heated rods, as well as buoyancy induced fluid motion in, and natural convection and radiation heat transfer across, the cover gas. The calculations used measured values of the heater rod and enclosure wall emissivities. Simulations were performed using a range thermal contact conditions between the heated rods and spacer plates that held them. The contact conditions only affected the rod temperatures close to the spacers, and had only minor effects on the center-rod temperatures. The benchmarked thermal simulations can now be used for a number of other applications.

Simulations can now be performed for a range of heater rod and enclosure surface emissivities. The results may be used to determine the sensitivity of the peak rod temperature to those surface properties, and to develop dimensionless correlations. For example, the Nusselt number, based on the temperature difference between the hottest rod and the enclosure walls, may be determined as a function of the Rayleigh number (which affects natural convection) and the surface emissivities (which affects surface-to-surface radiation).

The current simulations used isothermal enclosure walls. However, the basket temperatures in transport and storage casks can be highly non-uniform. The benchmarked simulations can be used to determine the sensitivity of the rod temperatures to non-isothermal basket temperatures, and then used to design a benchmark experiment. This experiment may employ the heated rod array of the current study, but place it within a lower thermal conductivity enclosure. The walls of the enclosure could be differentially heated, using separate heaters on each wall, to obtain different wall temperatures.

When spent fuel is removed from underwater storage and placed in dry canisters, all moisture must be removed before the canisters can be sealed. Vacuum drying, in which the cover gas is evacuated from the canister to promote water evaporation and vapor removal, has been commonly used for this purpose. Natural convection is virtually eliminated as a mode to remove heat from the assemblies. This may cause the fuel cladding temperature to rise above its allowed limit. Moreover, the gas is rarified to the level that classical continuum models are inaccurate for predicting the fuel rod temperatures. A temperature-jump model, based on rarefied gas theory, has been incorporated into the current CFD simulations. It predicts the temperature difference between the heat surfaces and the rarefied gas that exist under rarefied gas conditions. These simulations can be used to design benchmark experiments. Comparison of the simulation results to the experimental data can be used to test the validity of the temperature-jump model for the fuel assembly configuration.

Fuel assemblies are frequently stored in the vertical orientation. The current benchmark experiment only modeled the length of a BWR assembly between consecutive spacer plates. In real assemblies, the spacer plates are porous, and this allows some gas to pass through them. A more accurate benchmark experiment would involve construction of a full-length assembly in an enclosure, including porous spacer plates. This would more accurately model the conditions of natural convection within spent fuel storage casks than the current experiment.

Finally, fully three-dimensional simulations of whole casks (with multiple fuel assemblies) using the geometrically-accurate fuel assembly grids employed in the current work require extensive computational resources. These resources may not be readily available to design or analysis engineers. It may be more practical to construct course grids in the fuel/cover gas region that model the fuel with a limited number of axial grid points, and a uniform temperature at each axial location. The current benchmarked CFD simulations may be used to test the accuracy of those types of course-grid calculations.

REFERENCES

[1] U.S. Dept. of Energy, Office of Civilian Radioactive Waste Management (OCRWM), 1987, "Characteristics of Spent Nuclear Fuel, High-Level Waste, and Other Radioactive Wastes Which May Require Long-Term Isolation", DOE/RW-0184.

[2] Saling, J.H. and Fentiman, A.W., 2001, *Radioactive Waste Management*, 2nd Edition, Taylor and Francis, New York.

[3] NRC, 2005 "Cladding Considerations for the Transportation and Storage of Spent Fuel," Interim Staff Guidance Report for the Spent Fuel Project Office of the U.S. NRC, ISG-11 R3; available at www.nrc.gov

[4] General Atomics (GA), 1998, "GA-4 Legal Weight Truck From-Reactor Spent Fuel Shipping Cask, Safety Analysis Report for Packaging (SARP)," San Diego, California 92186-5608.

[5] Office of Civilian Radioactive Waste Management (OCRWM), US Department of Energy, 1993, "Multi-Purpose Canister (MPC) Implementation Program Conceptual Design Phase Report," DOC ID: A20000000-00811.

[6] Greiner, M., Gangadharan, K.K., and Gudipati, M., 2007, "Use of Fuel Assembly/Backfill Gas Effective Thermal Conductivity Models to Predict Basket and

Fuel Cladding Temperatures within a Rail Package During Normal Transport," *Nuclear Technology*, Vol. 160, pp. 325-336.

[7] Unterzuber, R., Milnes, R.D., Marinkovich, B.A., and Kubancsek, G.M., 1982, "Spent-Fuel Dry-Storage Testing at E-MAD (March 1978 through March 1982)," prepared for the US DOE Commercial Spent Fuel Management Program Office at the Pacific Northwest Laboratory, B-D3339-A-G.

[8] Manteufel, R. D. and Todreas, N. E., 1994, "Effective Thermal Conductivity and Edge Conductance Model for a Spent-Fuel Assembly", *Nuclear Technology*, Vol. 105, pp. 421-440.

[9] Bahney, R. H. and Lotz, T. L., 1996, "Spent Nuclear Fuel Effective Thermal Conductivity Report" U.S. DOE, Yucca Mountain Site Characterization Project Office, D.I.: BBA000000-01717-5705-00010 REV 00.

[10] Canaan, R E., and Klein, D.E., 1998, "A Numerical Investigation of Natural Convection Heat Transfer within Horizontal Spent-Fuel Assemblies", *Nuclear Technology*, Vol. 123, Aug. pp. 193-208.

[11] Canaan, R.E., and Klein, D.E., 1996, "An Experimental Investigation of Natural Convection Heat Transfer within Horizontal Spent-Fuel Assemblies," *Nuclear Technology*, December, Vol.116, pp. 306-318.

[12] Venigalla, V.V.R., and Greiner, M., 2007, CFD Simulations of Natural Convection/Radiation Heat Transfer within the Fuel Regions of a Truck Cask for Normal Transport," PVP2007-26242, Proceedings of the 2007 ASME Pressure Vessels and Piping Division Conference, July 22-26, 2007, San Antonio, Texas.

[13] Gudipati, M., and Greiner, M., 2007, "CFD Simulations of Fuel Cladding and Basket Surface Temperatures in an MPC Rail Cask during Normal Transport," proceedings of the 15th International Symposium on the Packaging and Transportation of Radioactive Materials (PATRAM).

[14] Gomez, P.E.A., and Greiner, M., 2006, "2D Natural Convection and Radiation Heat Transfer Simulations of a PWR Fuel Assembly within a Constant Temperature Support Structure PVP2006-ICPVT-11-93332, Proceedings of PVP2006-ICPVT-11, 2006 ASME Pressure Vessels and Piping Division Conference, July 23-27, Vancouver, BC, Canada.

[15] Araya, P.E. and Greiner, M., 2007, "Use of Regular Rod Arrays to Model Heat Transfer from BWR Fuel Assemblies inside Transport Casks," *Packaging, Transport, Storage and Security of Radioactive Material*, Vol. 18, pp. 171-179.

[16] Lovett, P. M., 1991, "An Experiment to Simulate the Heat Transfer Properties of a Dry, Horizontal Spent Nuclear Fuel Assembly," M.S. Thesis, Nuclear Eng., Massachusetts Institute of Technology

[17] Gomez, P.E.A., and Greiner, M. 2006, "Benchmark Natural Convection/Radiation Simulations within an Enclosed Array of Horizontal Heat Rods," PVP2006-ICPVT-11-94021, Proceedings of PVP2006-ICPVT-11, 2006 ASME Pressure Vessels and Piping Division Conference, July 23-27, Vancouver, BC, Canada, to appear in *Nuclear Technology*.

[18] Arya, S., 1990, "Convective Heat Transfer in a Sealed Vertical Storage Cask Containing Spent Fuel Canisters," M.S. Thesis, Mechanical Engineering Department, University of Tennessee, Knoxville.

[19] Arya, S., and Keyhani, M., 1990, "Convective Heat Transfer in a Sealed Vertical Storage Cask Containing Spent Fuel Canisters," *Nuclear Science and Engineering*, Vol. 105, pp. 391-403.

[20] Chalasani, N.R., and Greiner, M., 2009, "Natural Convection/Radiation Heat Transfer Simulations of an Enclosed Array of Vertical Rods," *Packaging, Transport, Storage and Security of Radioactive Material*, Vol. 20, no. 3, pp. 117-125.

[21] Doebelin, E.O., 2004, *Measurement Systems, Application and Design*, 5th Edition, McGraw-Hill.

[22] Chalasani, N.R., Araya, P., and Greiner, M., 2009, " Benchmark of Computational Fluid Dynamics Simulations using Temperatures Measured within Enclosed Vertical and Horizontal Arrays of Heated Rods," *Nuclear Technology.*, Vol. 167, No. 3, pp. 371-383.

Symmetry Group name	Rods in Symmetry Group	Rods with TC's in Group	Number of Rods with TC's in Group
R1	A1, A8	A1, A8	2
R2	C3, C6	C3, C6	2
R3	D3, D6	D3, D6	2
R4	D4, D5	D4, D5	2
R5	E3, E6	E3, E6	2
R6	E4, E5	E4, E5	2
R7	F4, F5	F4, F5	2
R8	H1, H8	H1, H8	2

Table 1 Rod symmetry groups for horizontal orientation for determining the axial temperature profiles of archetypical heaters in the assembly.

Symmetry Group name	Rods in Symmetry Group	Rods with TC's in Group	Number of Rods with TC's in Group
S1	A1, A8, H1, H8	A1	1
S2	A2, A7, B1, B8, G1, G8, H2, H7	A2, A7, B1, B8, G1, H2, H7	7
S3	A3, A6, C1, C8, F1, F8, H3, H6	A3, A6, C1, F1, F8, H3	6
S4	A4, A5, D1, D8, E1, E8, H4, H5	A4, A5, D1, D8, E1, H4, H5	7
S5	B2, B7, G2, G7	B7	1
S6	B3, B6, C2, C7, F2, F7, G3, G6	B6	1
S7	B4, B5, D2, D7, E2, E7, G4, G5	B4, B5, D2, D7, G4, G5	6
S8	C3, C6, F3, F6	C3	1
S9	C4, C5, D3, D6, E3, E6, F4, F5	C4, C5	2
S10	D4, D5, E4, E5	D4	1

Table 2 Rod symmetry groups for mid-plane ($Z = 0$) temperature profiles for vertical orientation

Symmetry Group name	Rods in Symmetry Group	Rods with TC's in Group	Number of Rods with TC's in Group
S11	A1, A8, H1, H8	A1, A8, H1, H8	4
S12	C3, C6, F3, F6	C3, C6	2
S13	C4, C5, D3, D6, E3, E6, F4, F5	C4, C5, D3, D6, E3, E6, F4, F5	8
S14	D4, D5, E4, E5	D4, D5, E4, E5	4

Table 3 Rod symmetry groups for vertical orientation for determining the axial temperature profiles of archetypical heaters in the assembly.

Insulation	Al - Walls	SS - Endplates	Gas	Pressure	Orientation	Heat Load	No. of Experiments
No - Insulation	2.5 cm	0	Nitrogen	1, 2 and 3 atm	Horizontal & Vertical	100, 200, 300, 400 and 500 W	30
2.5 cm - Insulation	2.5 cm	2.5 cm	Nitrogen and Helium	1, 2 and 3 atm	Horizontal & Vertical	100, 300 and 500 W	36
5 cm - Insulation	5 cm	5 cm	Nitrogen and Helium	1 atm	Vertical	100, 300 and 500 W	6
Total No. of Experiments = 72							

Table 4 Number of experiments performed in this study and their category

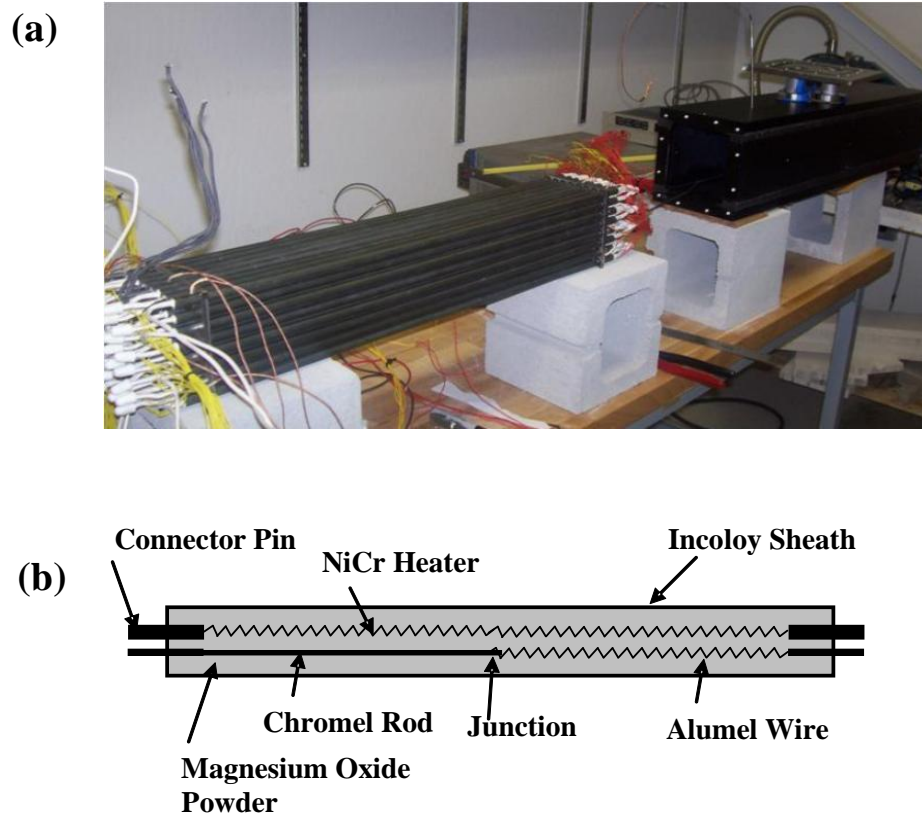


Fig. 1. (a) Photograph of 8 x 8 heater array with empty enclosure in the background (b) Schematic axial cut through one rod showing internal components (not to scale).

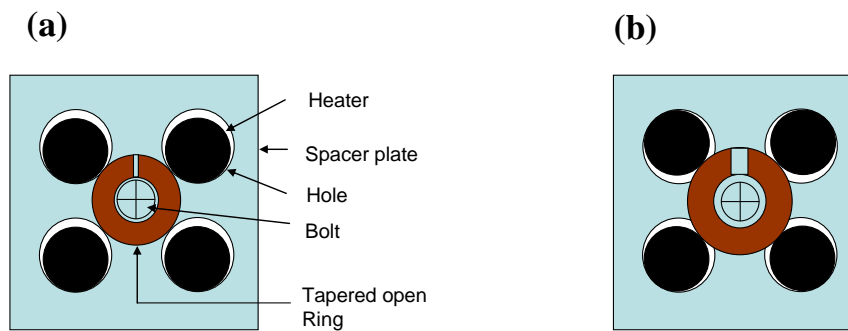


Fig. 2. System for fastening heater rods to spacer plates (a) Schematic of a part of the spacer plate with four holes of 1.15 cm in diameter, heaters in contact with the bottom of the openings and a tapered open ring with a bolt (b) The bolt screwed to the spacer plate with the tapered opened ring pushing the heaters against the holes.

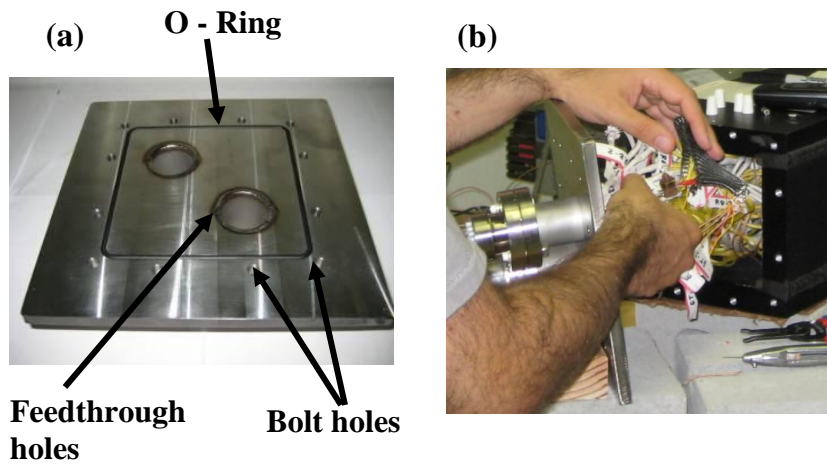


Fig. 3. (a) Endplate with high temperature perfluoroelastomer (315°C) O-ring, two holes for thermocouple and power feedthroughs (not shown) and twelve holes for the bolts (b) Wire and connectors filled gap between the spacer plates and the endplate before closure. Feedthroughs can be seen attached to outer surface of endplate.

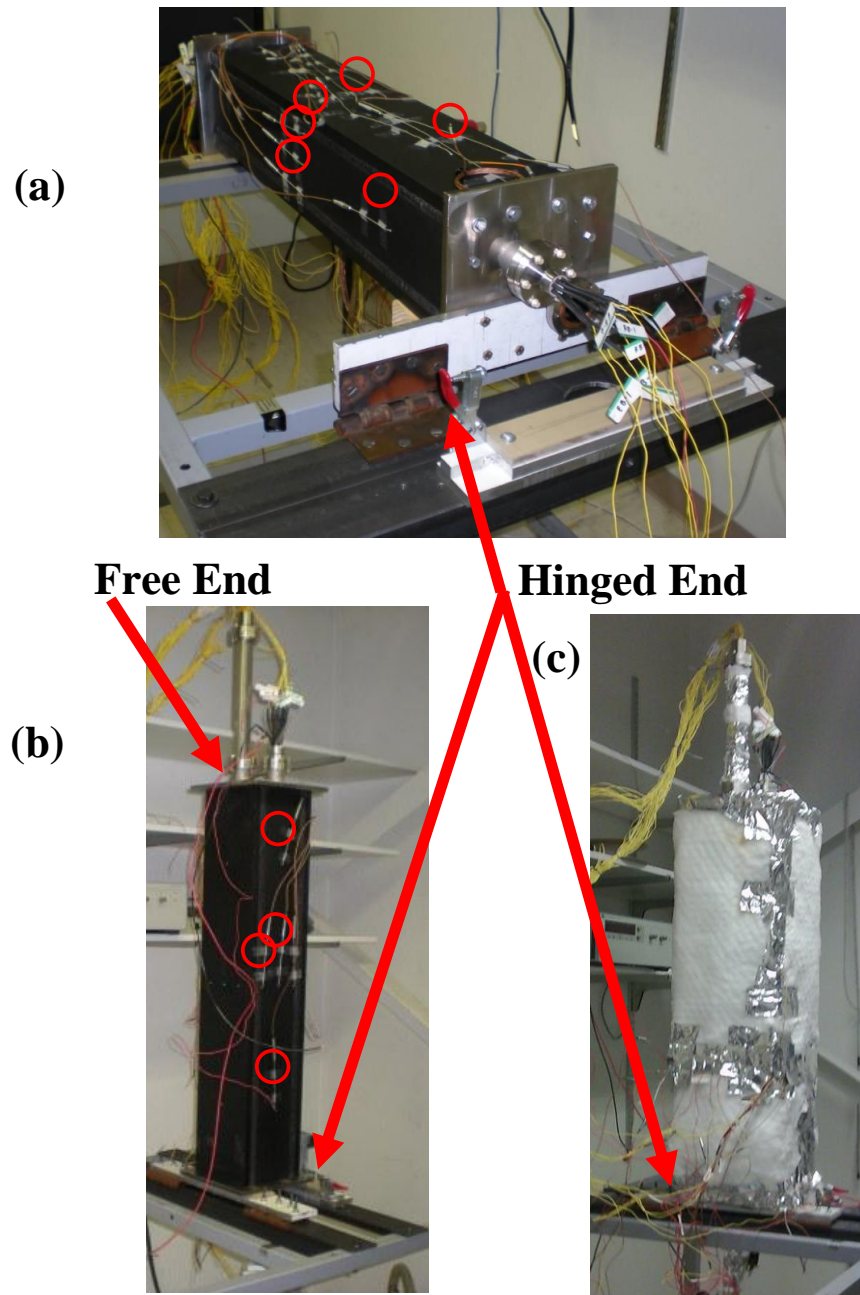


Fig. 4. Apparatus on hinged test stand without insulation. Circles show the locations where thermocouples enter the drilled thermocouple wells in the enclosure walls. Hinged and free ends are indicated. (a) Horizontal orientation (b) Vertical orientation with no insulation (c) Vertical orientation with insulation

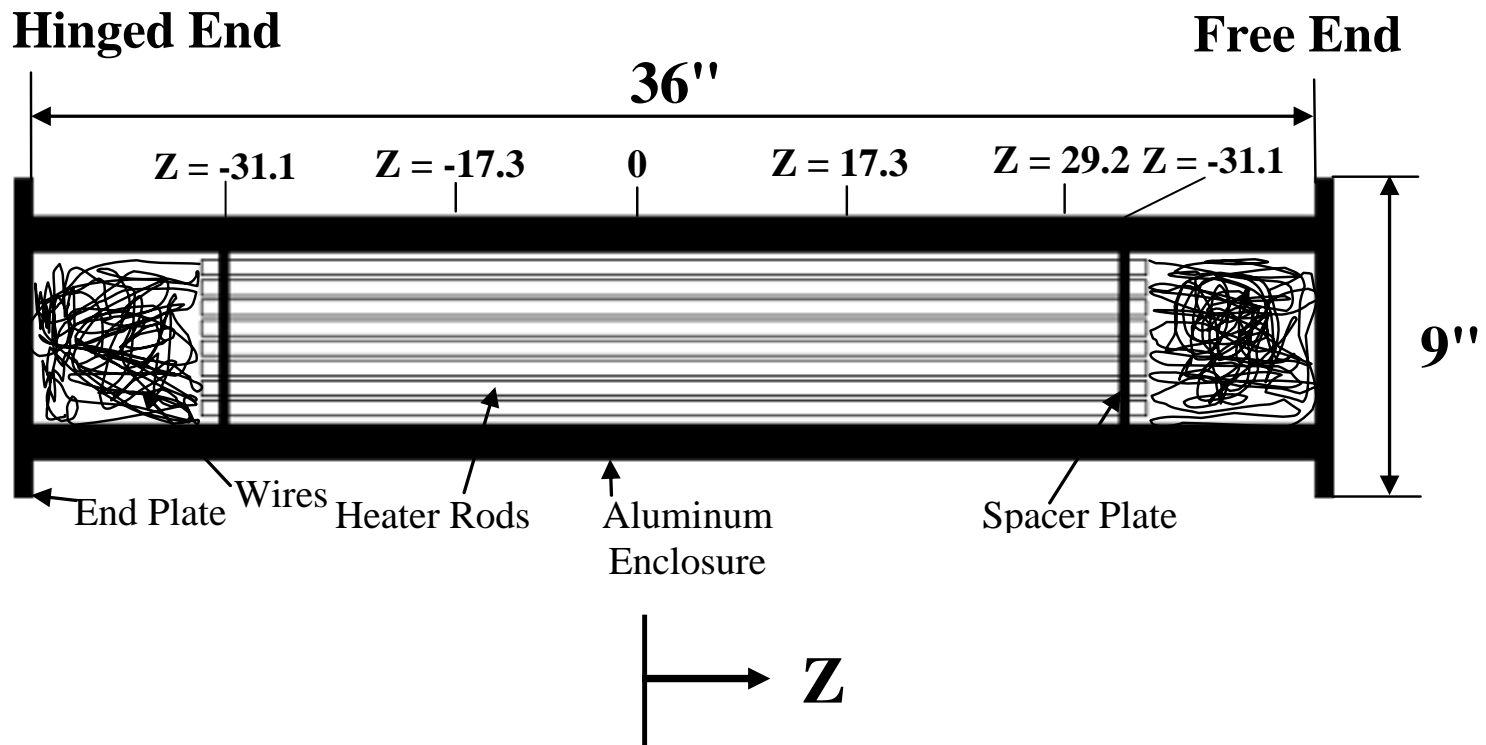


Fig.5. Schematic vertical axial cut view of the apparatus in horizontal orientation. Relative locations of internal components and the z -coordinate are shown. Thermocouples in heaters are located in planes at $Z = -17.3, 0, 17.3$ and 29.2 cm. Spacer plates are located at $Z = -31.1$ and 31.1 cm

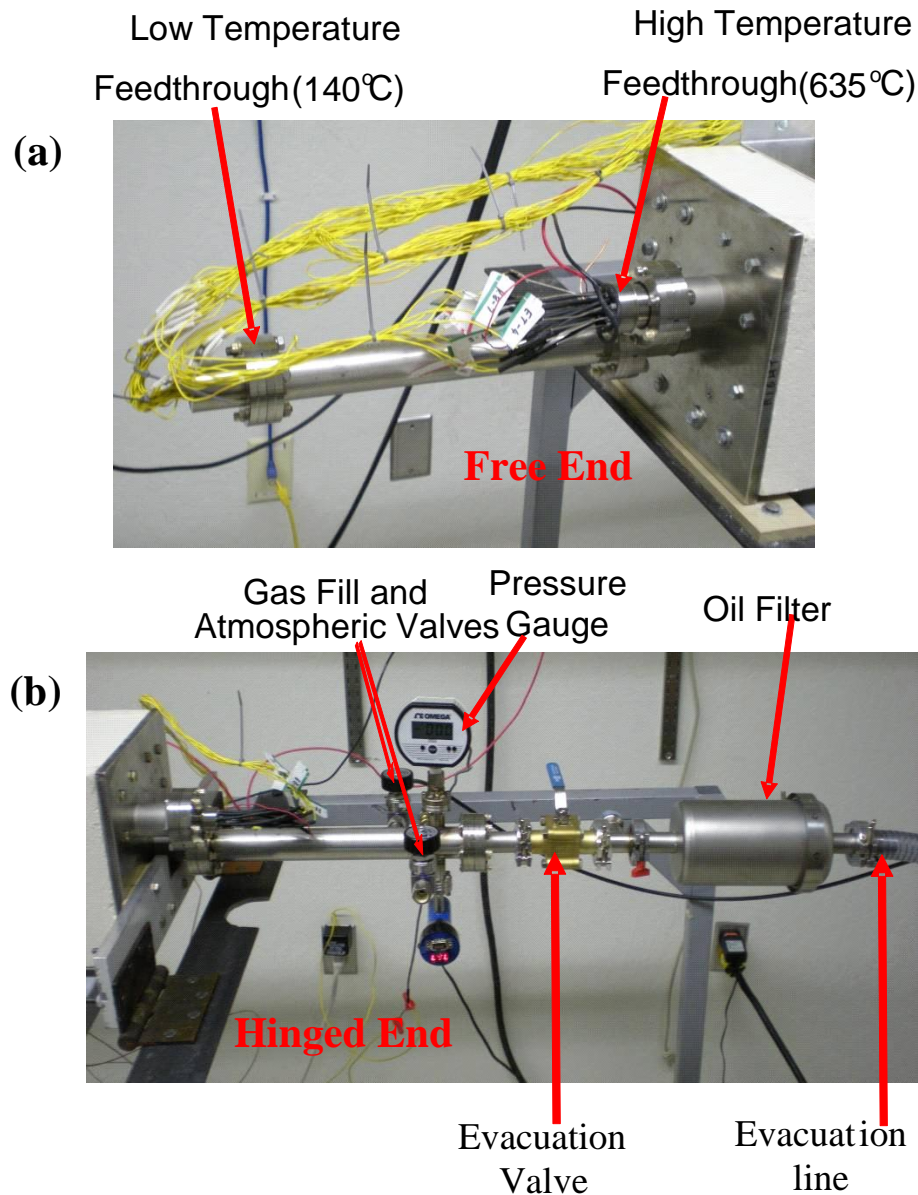


Fig. 6. Photograph of endplates and external components (a) Free end with one high temperature feedthrough (power leads) and one low temperature feedthrough (b) Hinged end with one high temperature feedthrough and a tube for pressure gauge, gas fill and atmospheric valves, evacuation valve, oil filter and evacuation line to the vacuum pump.

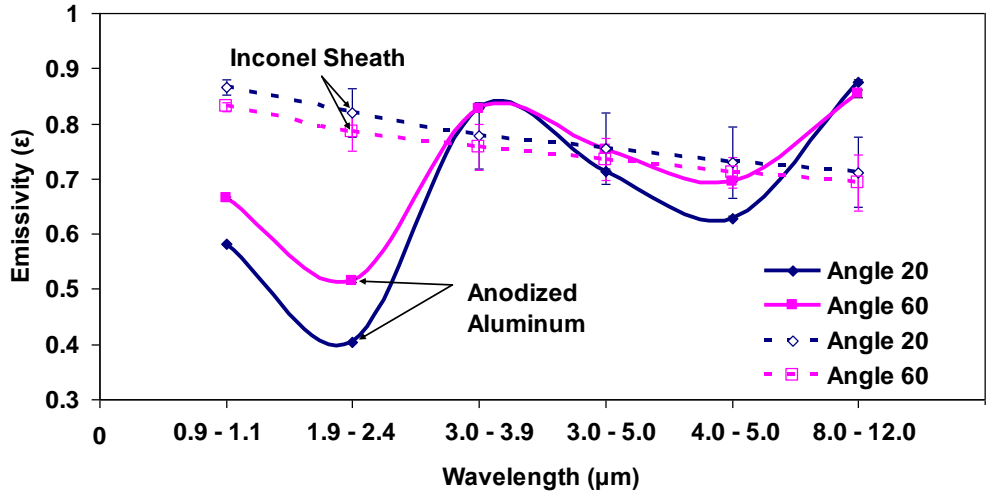
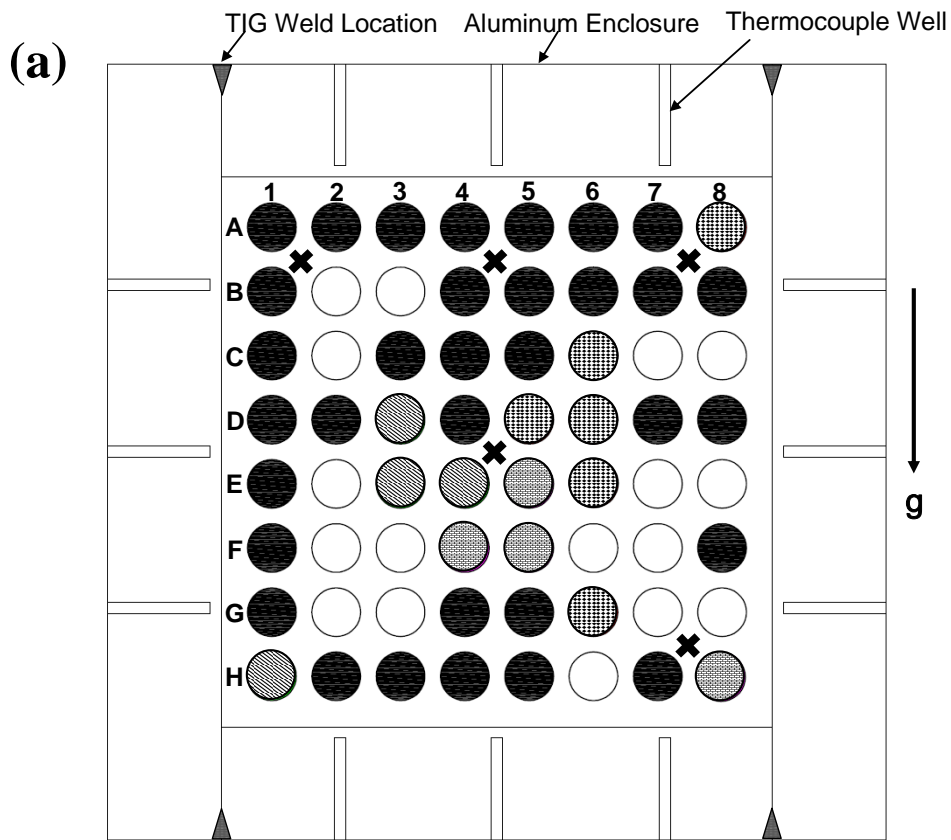


Fig. 7. Measured average (three measurements) emissivity of samples of inconel sheath from Watlow tubular heater rod and anodized black dye aluminum enclosure for different angles (20° and 60° from normal) as a function of wavelength range. Standard deviation for three measurements at each wavelength range are shown as error bars. Emissivities are measured using SOC 410C DHR Reflectometer with an uncertainty of ± 0.03 .



(b)


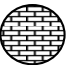


Texture	Z [cm]
	29.2
	17.3
	0
	-17.3

Fig. 8. (a) End view of experimental apparatus showing 64 heater rods (circles), locations of four spacer plate thermocouples (X's), aluminum enclosure walls, and the wall thermocouple wells. Textured circles are the rods that are instrumented with thermocouples. The direction of the gravity vector when the apparatus is in horizontal orientation is shown. Columns 1 through 8 and row A through H are labeled (b) Table shows the z location of the thermocouple for each texture used in Fig. 8(a).

	1&8	2&7	3&6	4&5
A	1	2	2	2
B	2	1	1	2
C	1		1	2
D	2	2		1
E	1			
F	2			
G	1			2
H		2	1	2

Fig. 9. Schematic of rod symmetry groups in the mid-plane for horizontal orientation. Columns labeled 1&8 through 4&5, combining the symmetry columns on either side of symmetry line. Circles with numbers show the locations of heaters with thermocouples at mid-plane ($Z = 0$) whereas open circles for heaters with no thermocouples. circles with 1 denotes for only one heater is instrumented with thermocouple among the two heaters for that horizontal symmetry location whereas 2 denotes that both heaters are instrumented.

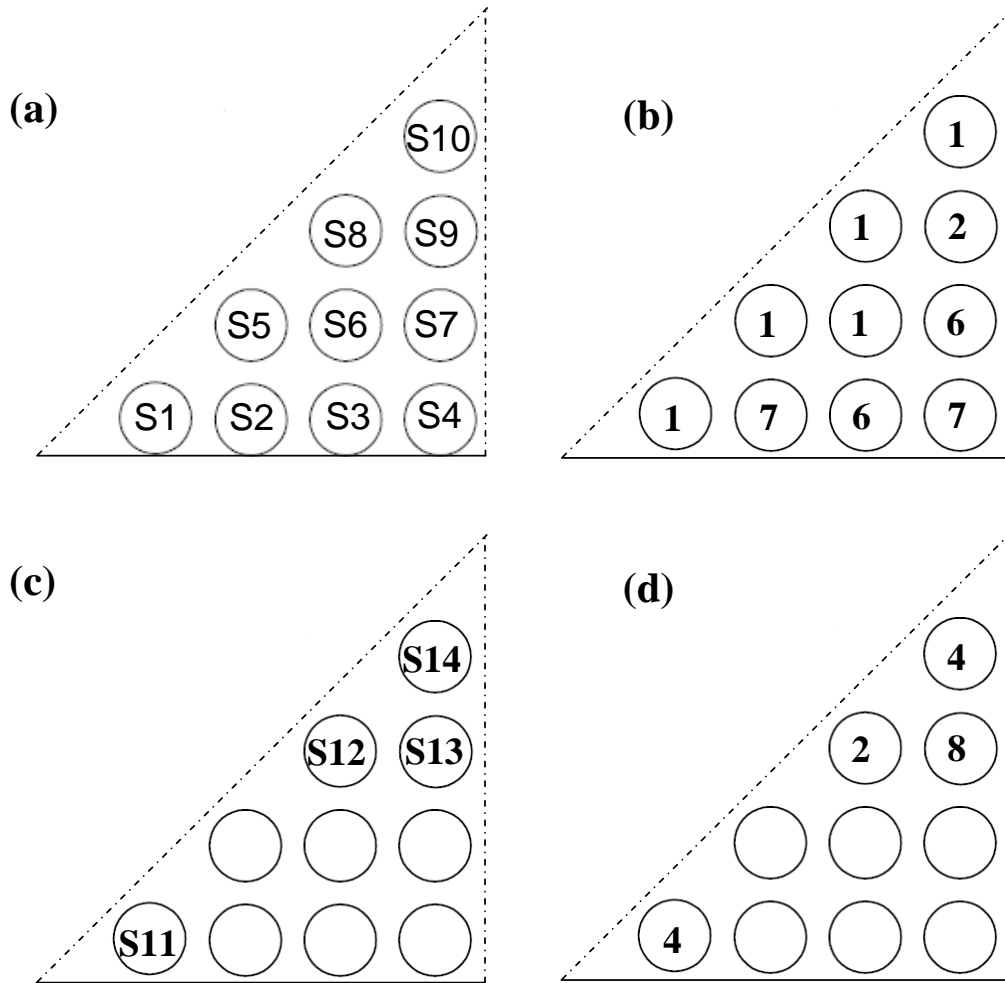


Fig.10 Schematic of one-eighth rod symmetry groups in the mid-plane ($Z = 0$) for vertical orientation. (a) Archetypical rods labeled S1 through S10. (b) Circles with numbers show the number of instrumented heaters for respective symmetry locations in the mid-plane ($Z = 0$). (c) Archetypical rods labeled S11 through S14 for one-eighth rod symmetry groups for axial locations (d) Circles with numbers show number of heaters with thermocouples at different axial locations

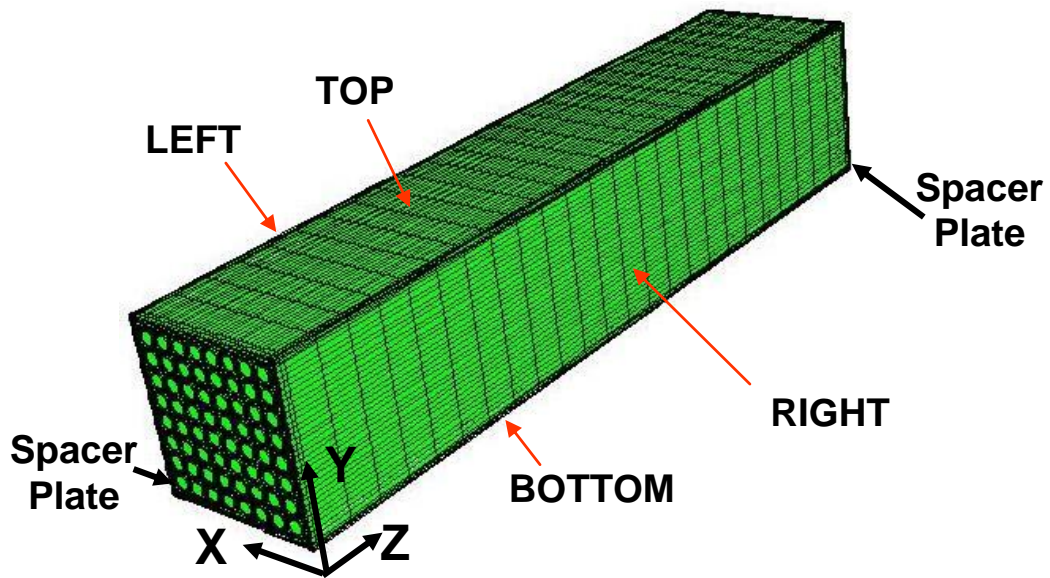


Fig. 11. Three-dimensional finite volume grid mesh and coordinate system

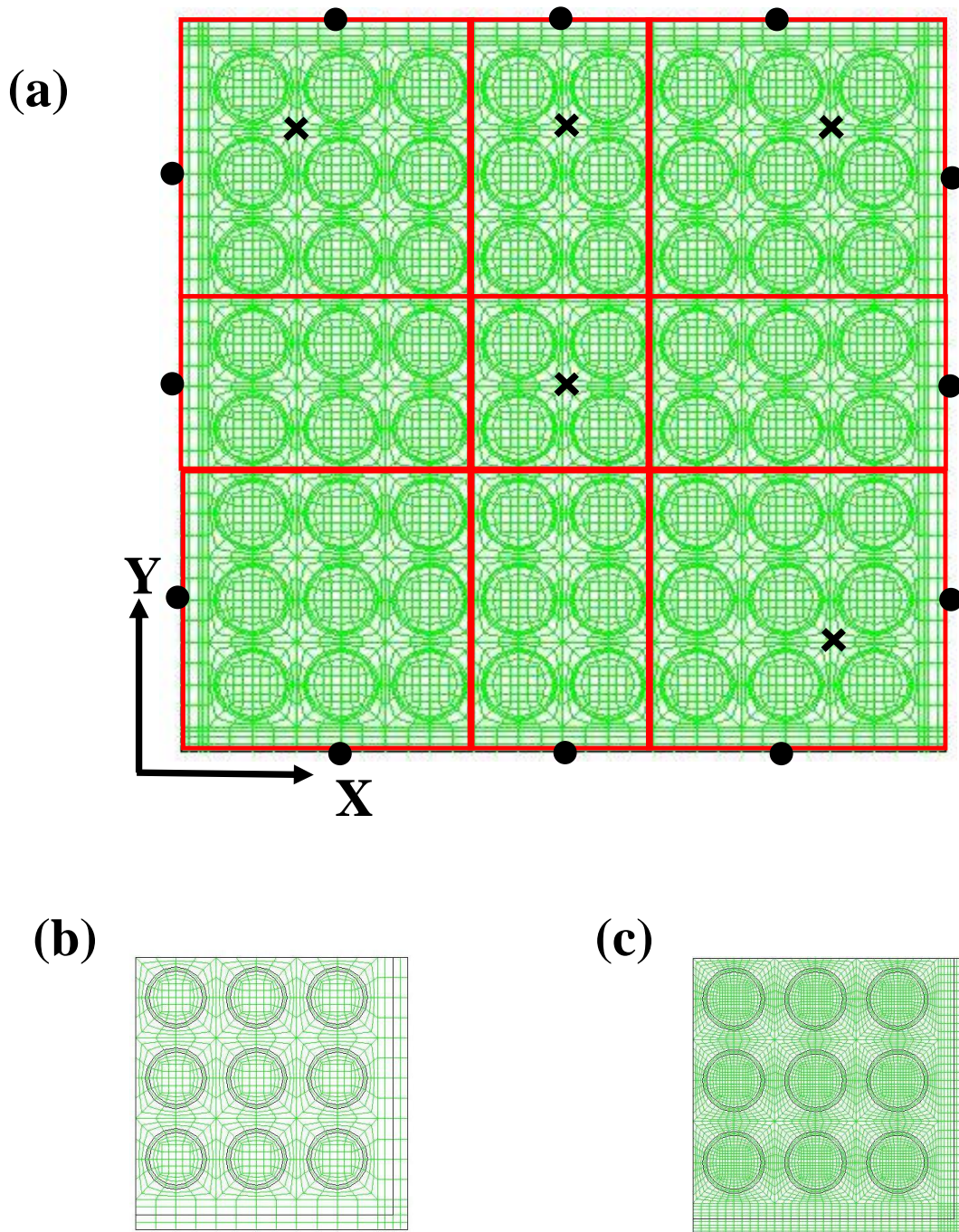


Fig. 12 End view of computational domain divided into nine parts. X's show the locations of the temperatures measured from the experiments on spacer plates and circles show the locations of temperatures measured on the aluminum walls. (a) Coarse mesh (b) Nominal mesh (c) Fine mesh

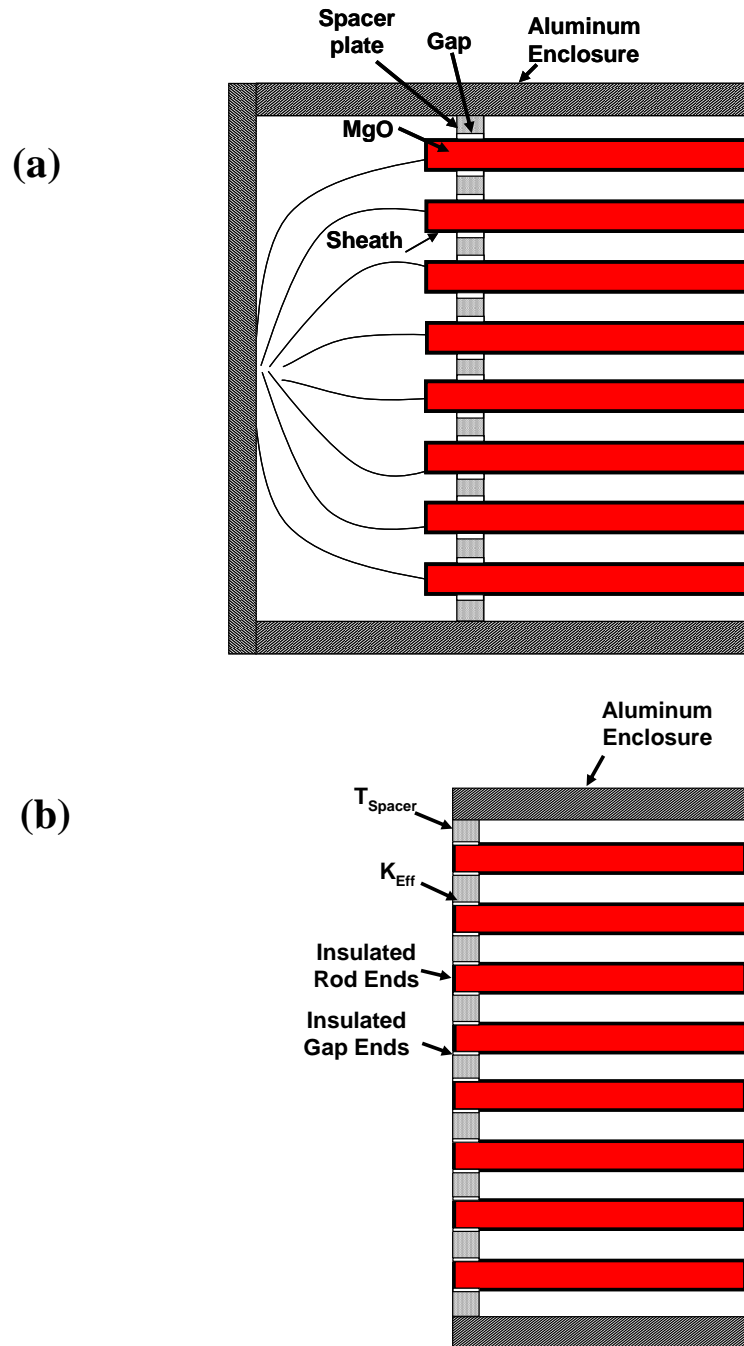


Fig. 13 (a) Schematic of experimental apparatus on the free end. (b) Schematic of computational domain on the free end.

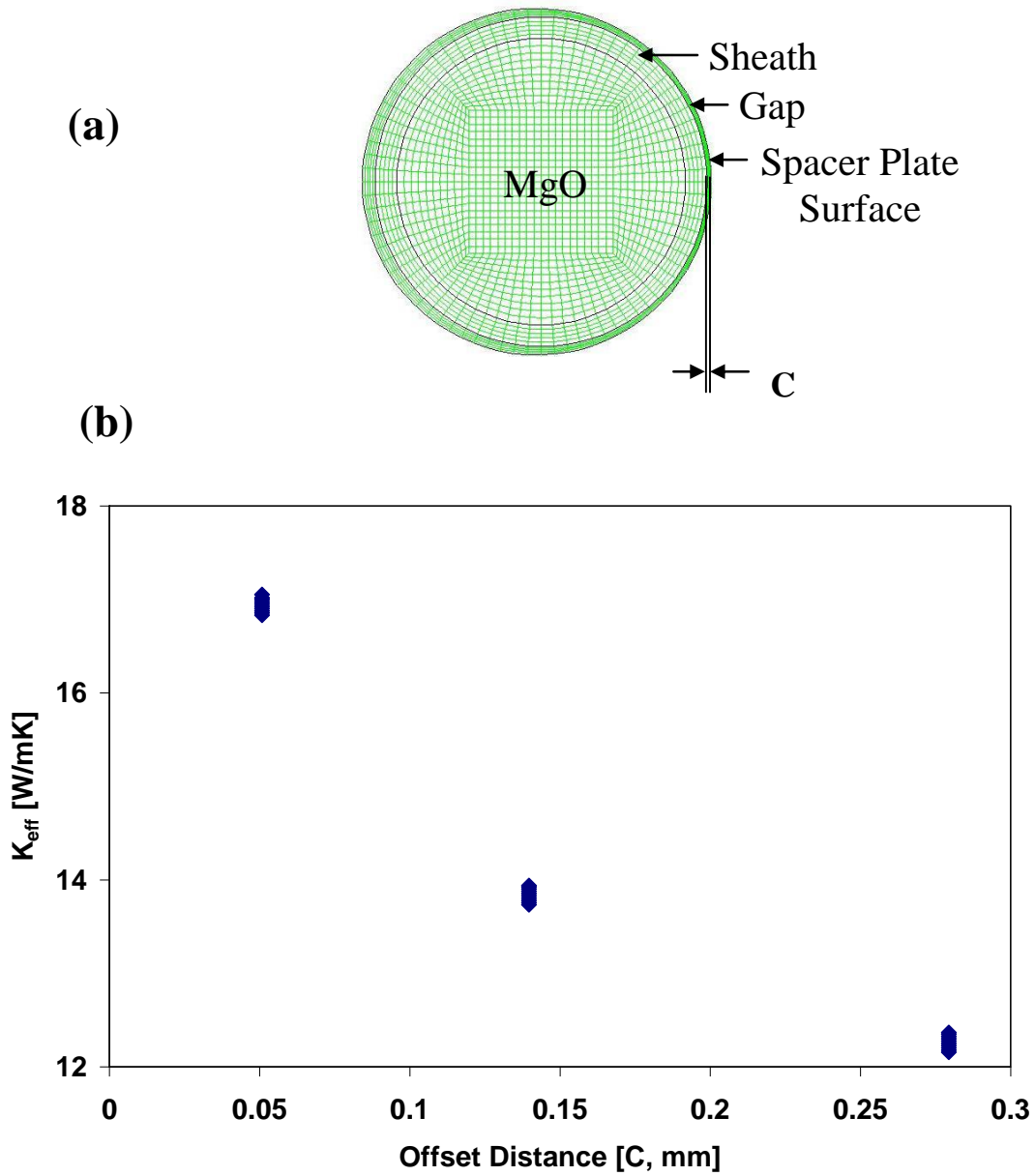


Fig. 14. (a) Numerical model for calculating effective thermal conductivity for cladding and gap associated with spacer plate. (b) Effective thermal conductivity versus offset distance.

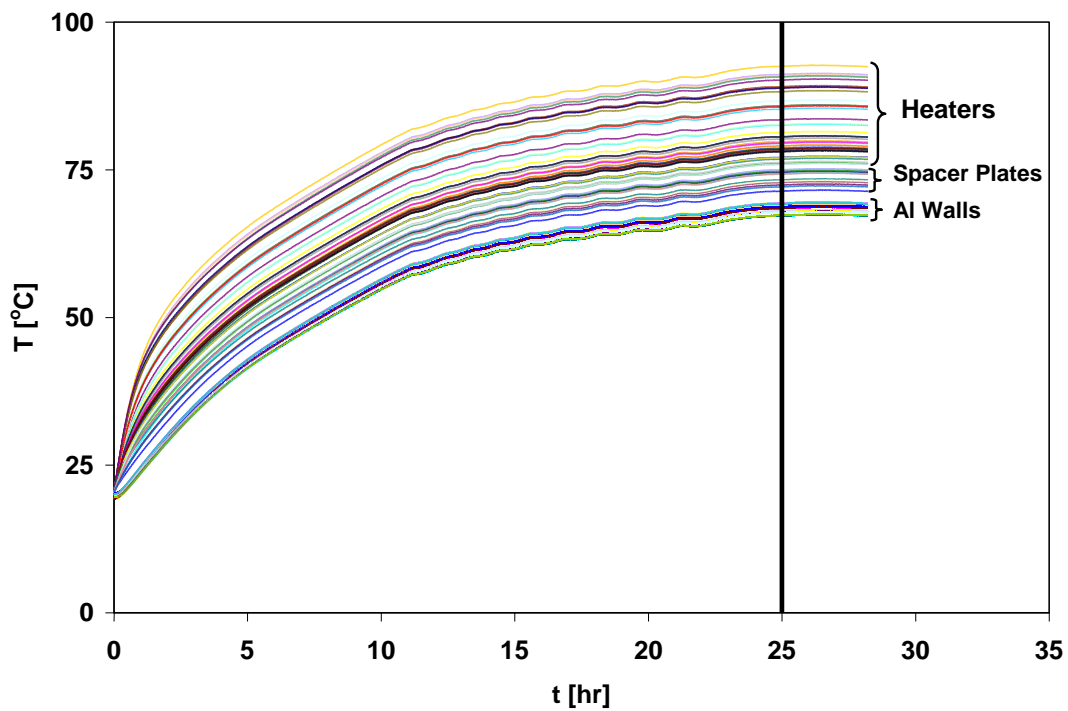


Fig. 15. Measured temperature of all 83 thermocouples versus time with the apparatus filled with helium in the horizontal orientation and $Q = 100$ W and $P = 1$ atm. The enclosure, spacer plate, and rod temperatures are identified

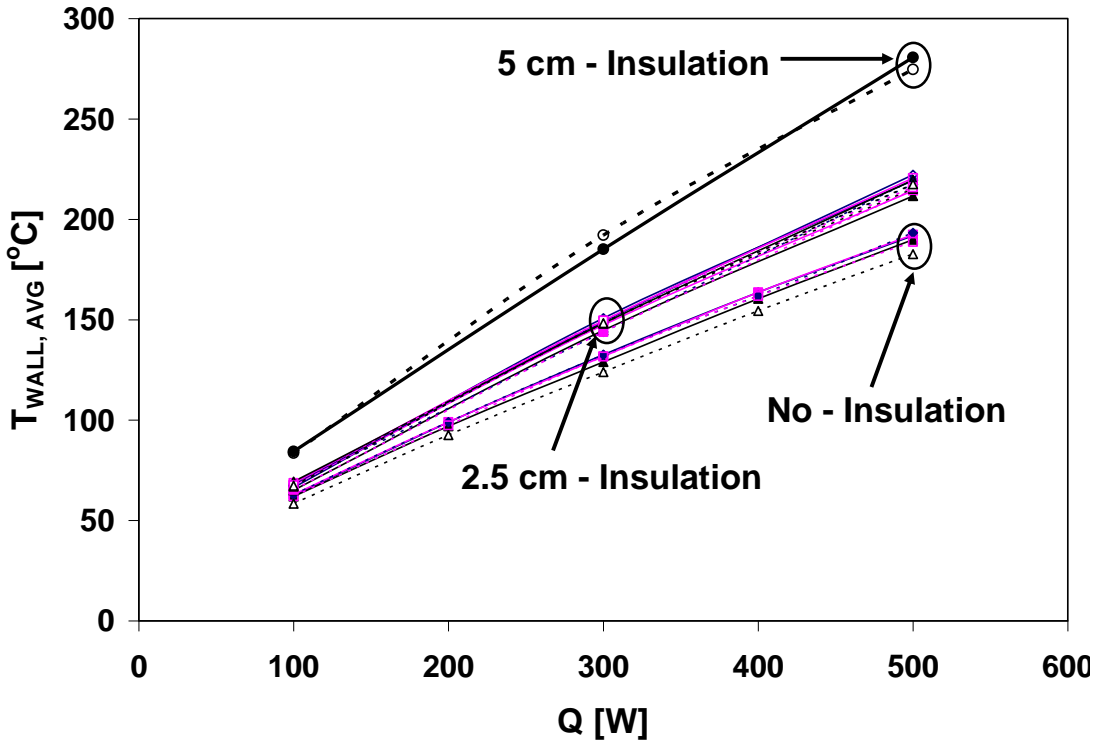


Fig. 16 Average of measured aluminum enclosure temperatures (22 thermocouples) versus rod heat generation rate for, no-insulation, 1"-inch insulation and 2"-inch insulation experiments.

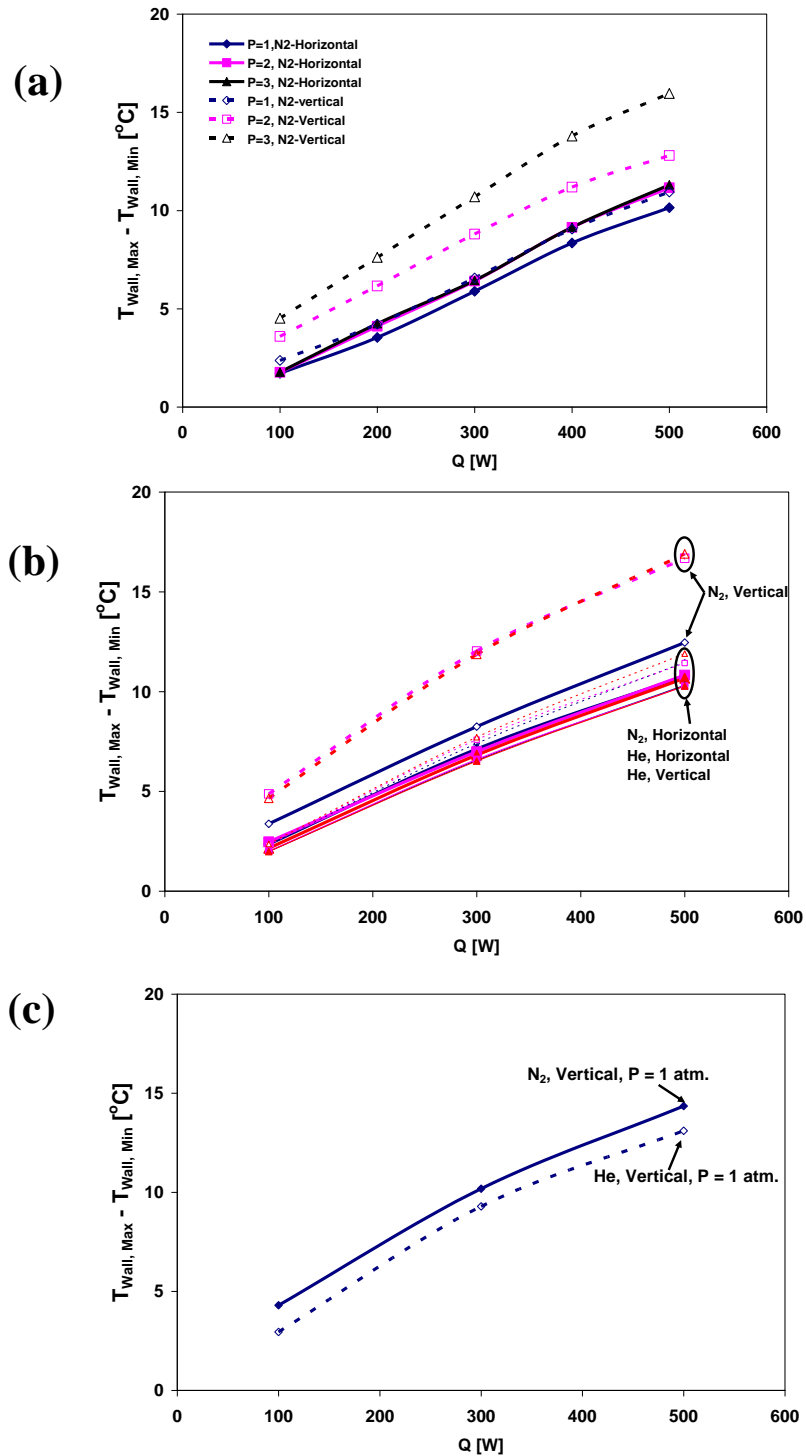


Fig. 17 Temperature difference between maximum and minimum enclosure temperatures (20 thermocouples) (a) No-insulation (b) 2.5 cm insulation (c) 5 cm insulation.

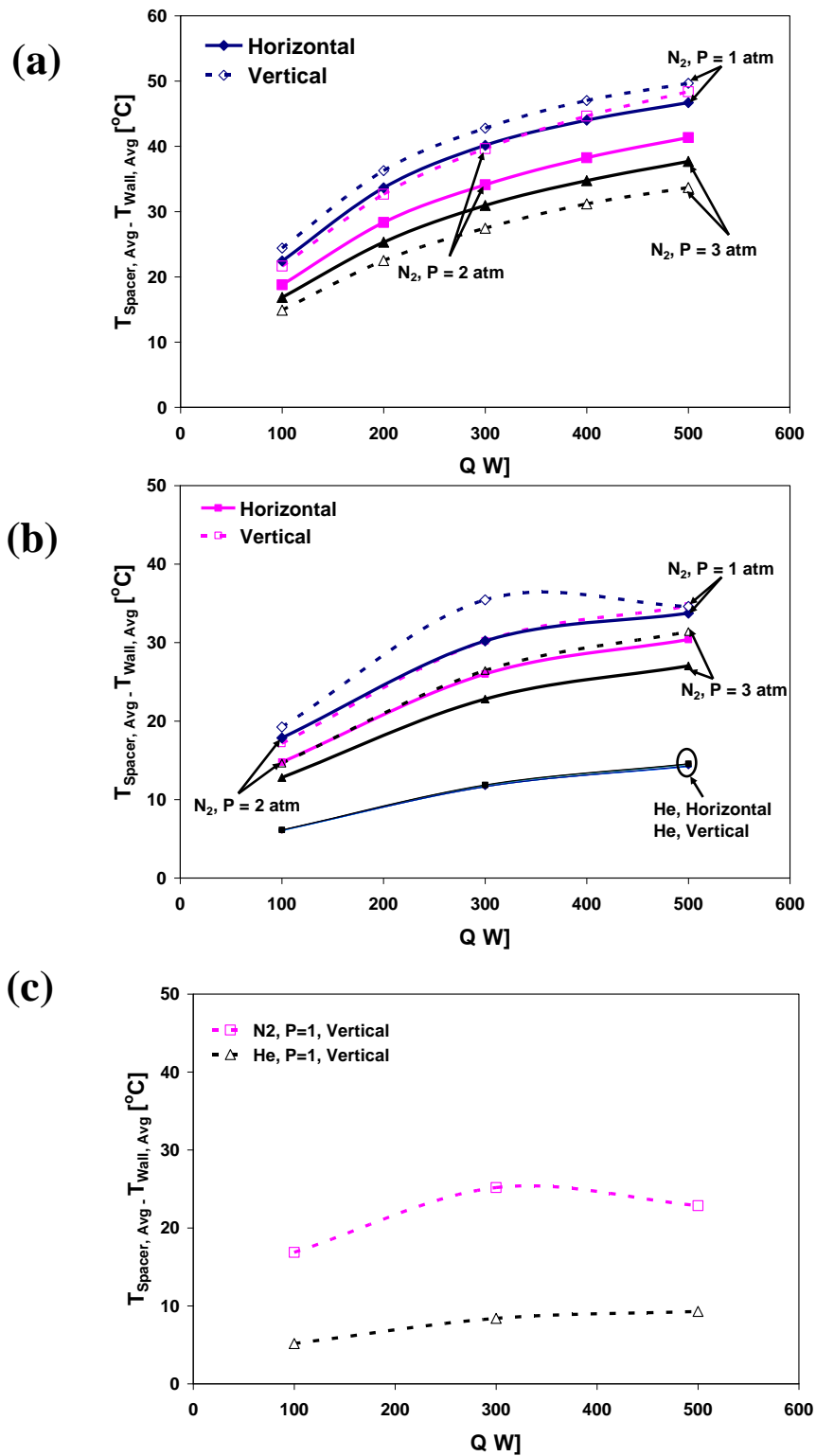


Fig. 18 Stainless steel spacer average temperature minus enclosure average temperature versus heat load (a) No-insulation (b) 2.5 cm insulation (c) 5 cm insulation.

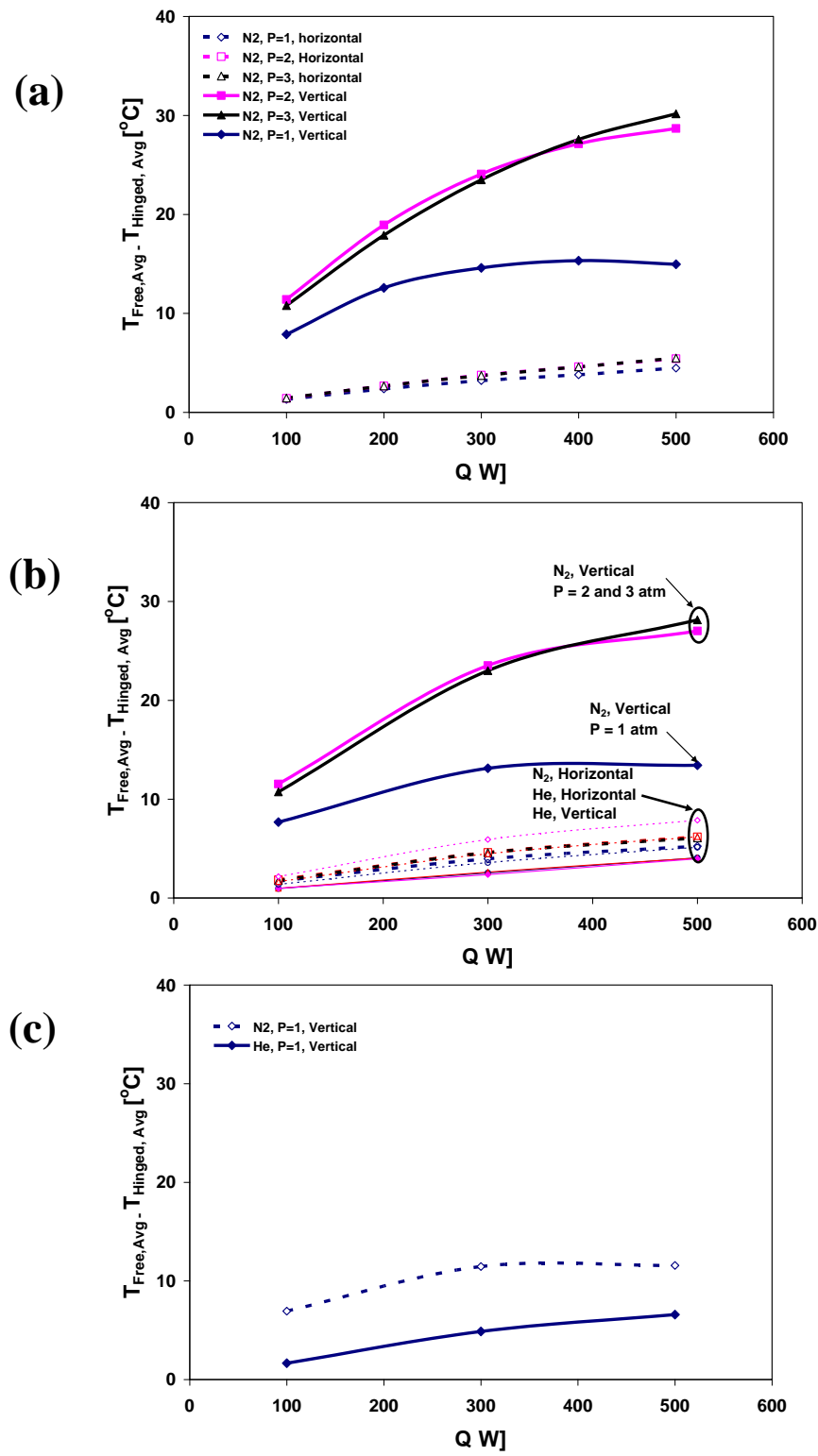


Fig. 19 Spacer free end average minus hinged end average temperatures versus heat load (a) No-insulation (b) 2.5 cm insulation (c) 5 cm insulation.

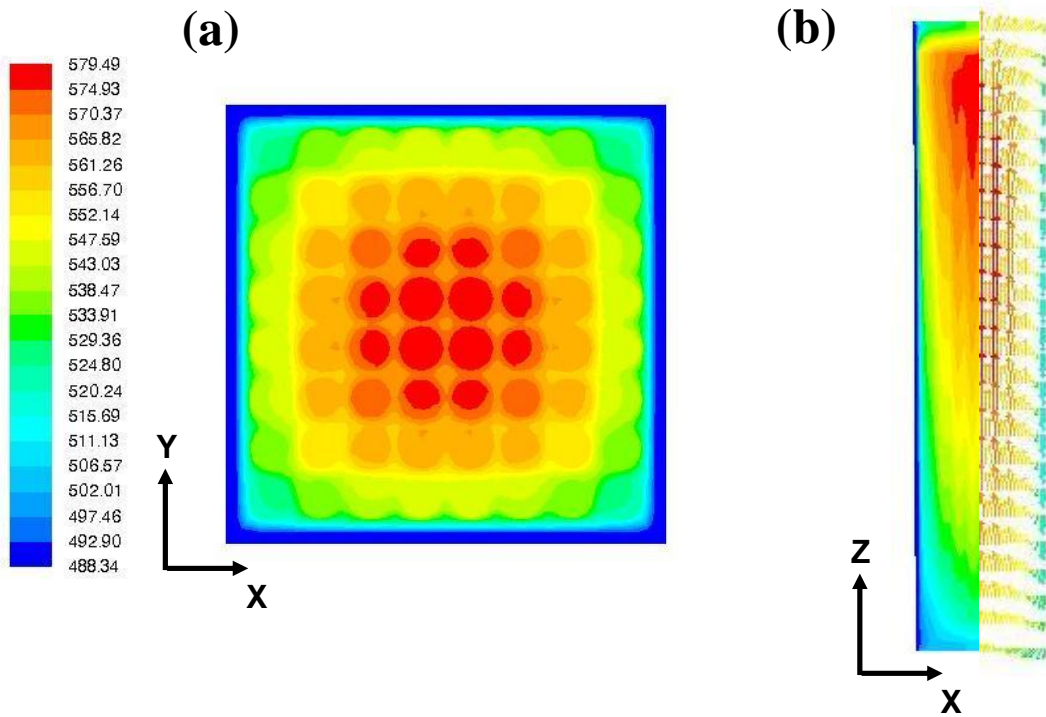


Fig. 20 Simulation results for vertical orientation at $Q = 500 \text{ W}$, $P = 3 \text{ atm}$ with nitrogen backfill (a) Enclosure, gas and rod temperature contours at mid-plane between spacer plates (b) Enclosure, gas and rod temperature contours and gas velocity field vectors in vertical mid-plane.

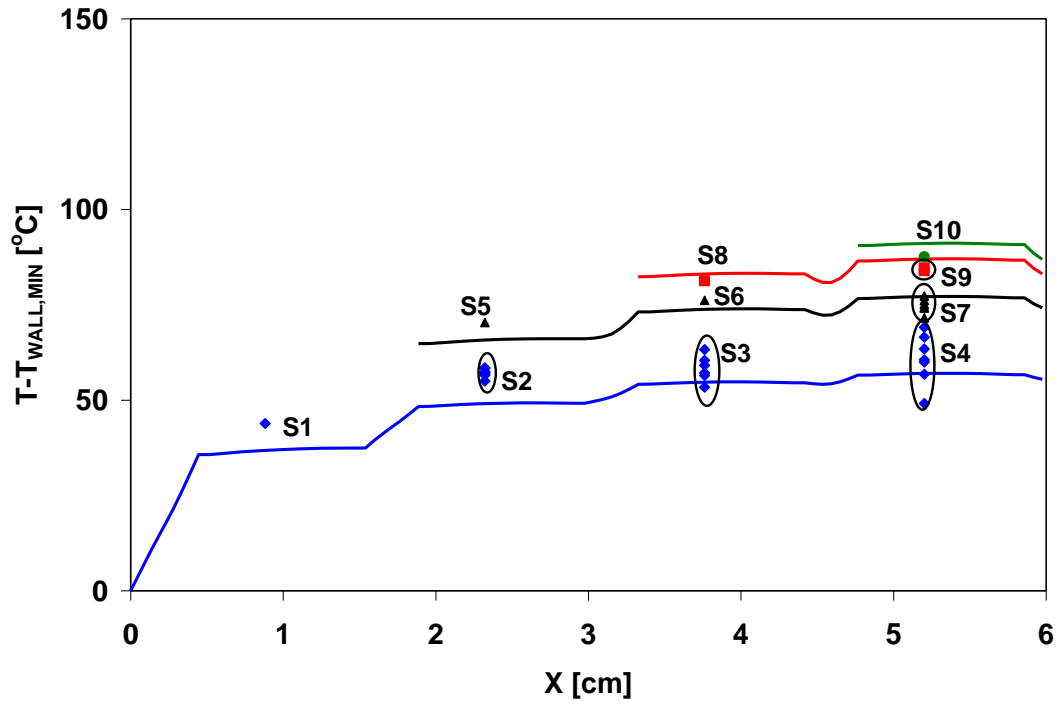


Fig. 21 Measured (symbols) and simulated (lines) mid-plane temperature difference for the vertical orientation. Results for each symmetry group are plotted versus the x-location for the archetypical rod in each group. Ovals enclose data where multiple measurements within a group exist.

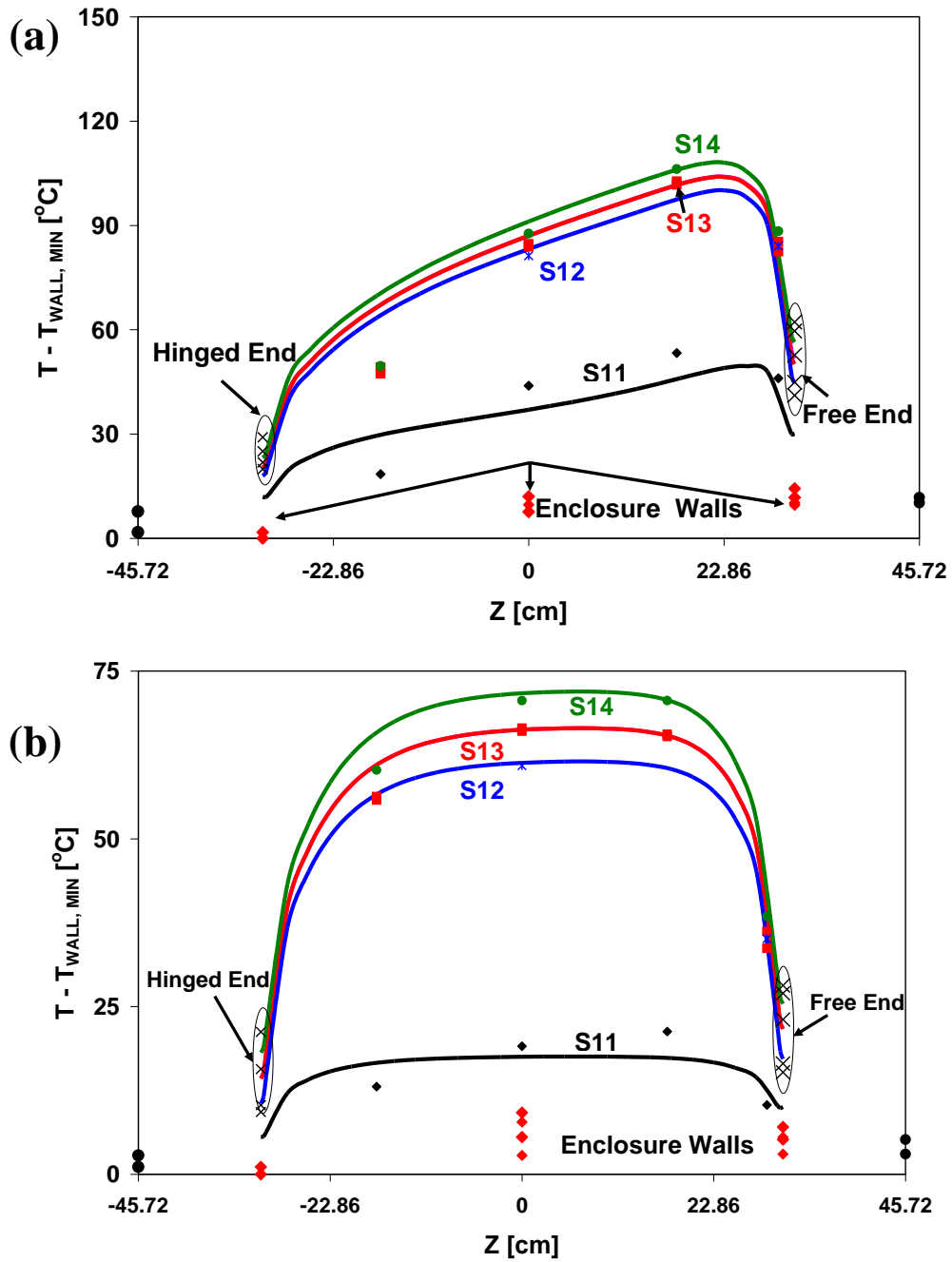
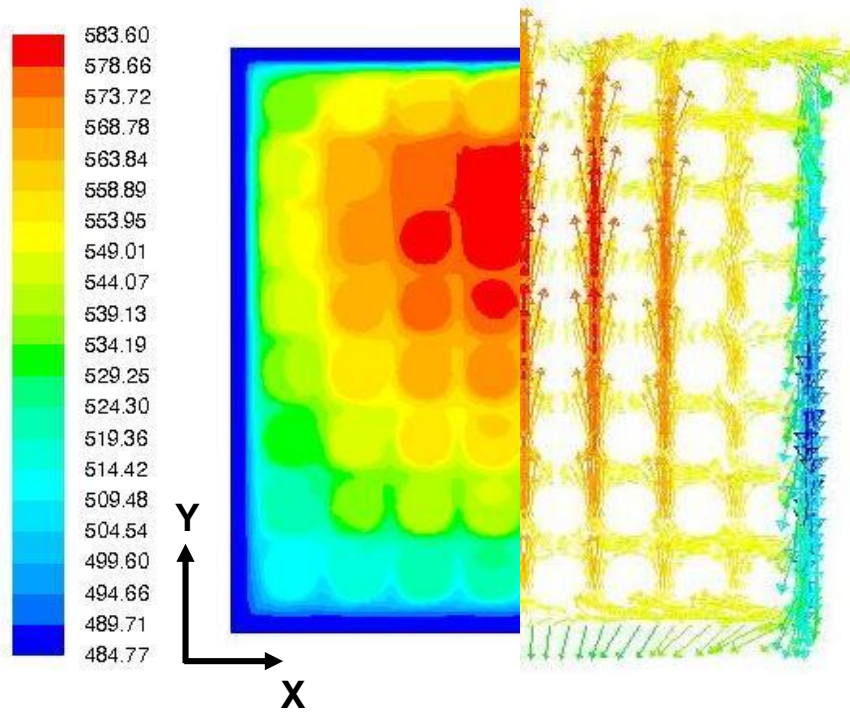


Fig. 22 Measured (symbols) and simulated (lines) temperature difference for the archetypal heaters in vertical orientation. Results for each symmetry group are plotted versus the x-location for the archetypal rod in each group (a) nitrogen (b) helium.

(a)



(b)

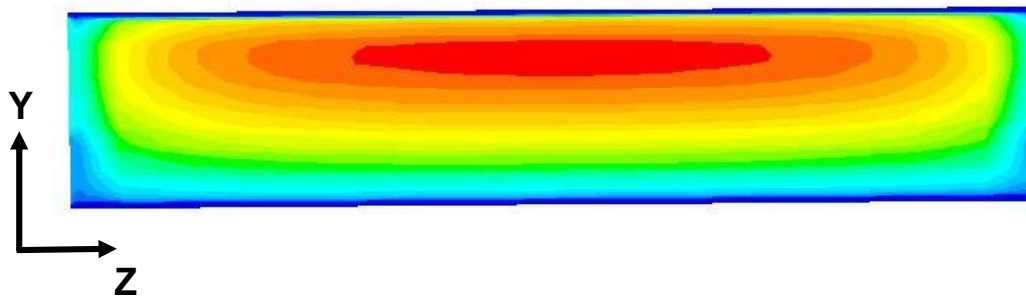


Fig. 23 Simulation results for horizontal orientation at $Q = 500 \text{ W}$, $P = 3 \text{ atm}$ with nitrogen backfill (a) Enclosure, gas and rod temperature contours and velocity vectors at mid-plane between spacer plates (b) Enclosure, gas and rod temperature contours and gas contours at the axial mid-plane.

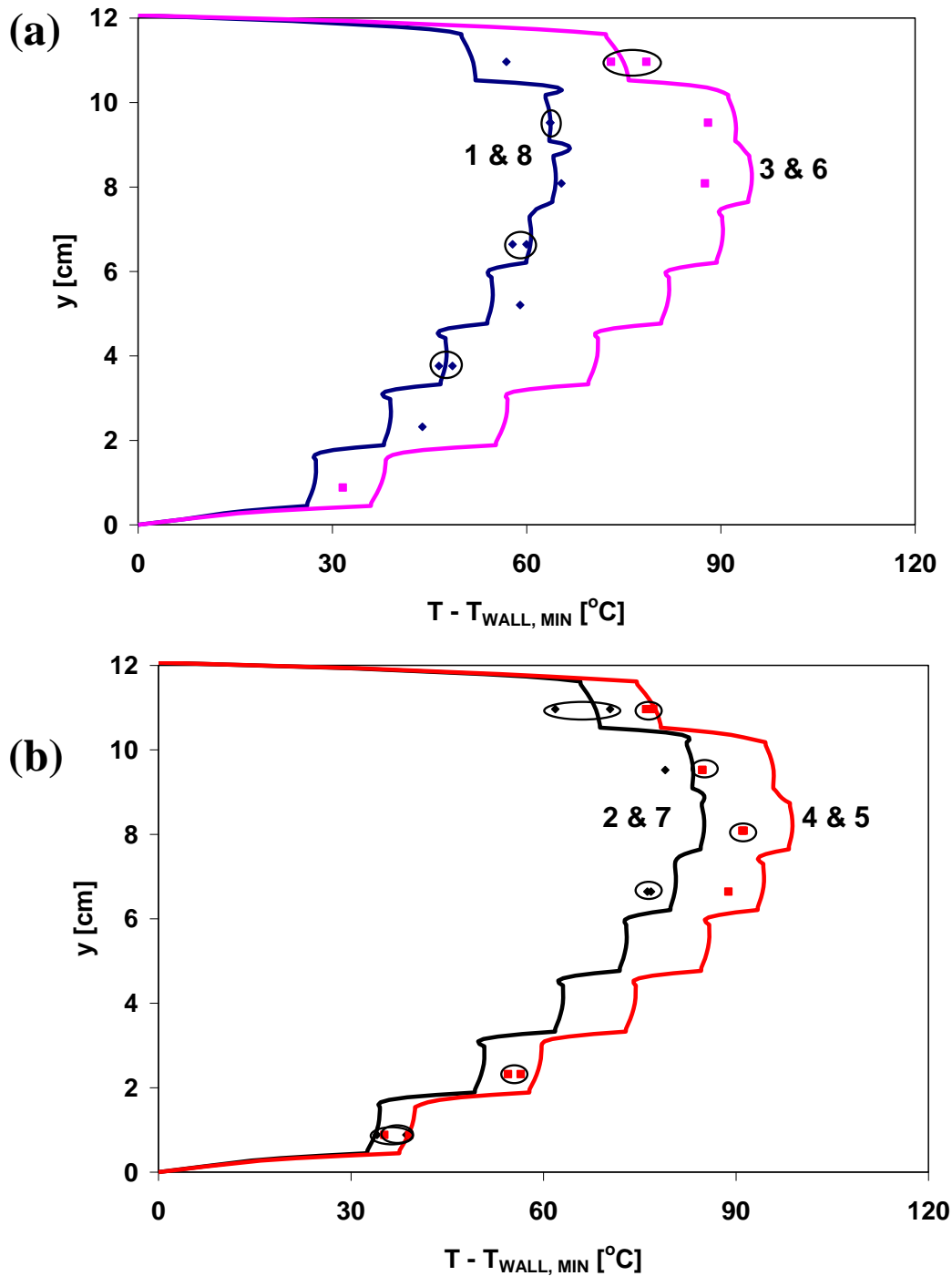


Fig. 24 Measured (symbols) and simulated (lines) mid-plane temperature difference versus y -location for the horizontal orientation. Ovals are used when two measurements were acquired for paired columns. Results from the following symmetric columns are paired together, (a) 1&8 and 3&6 (b) 2&7 and 4&5

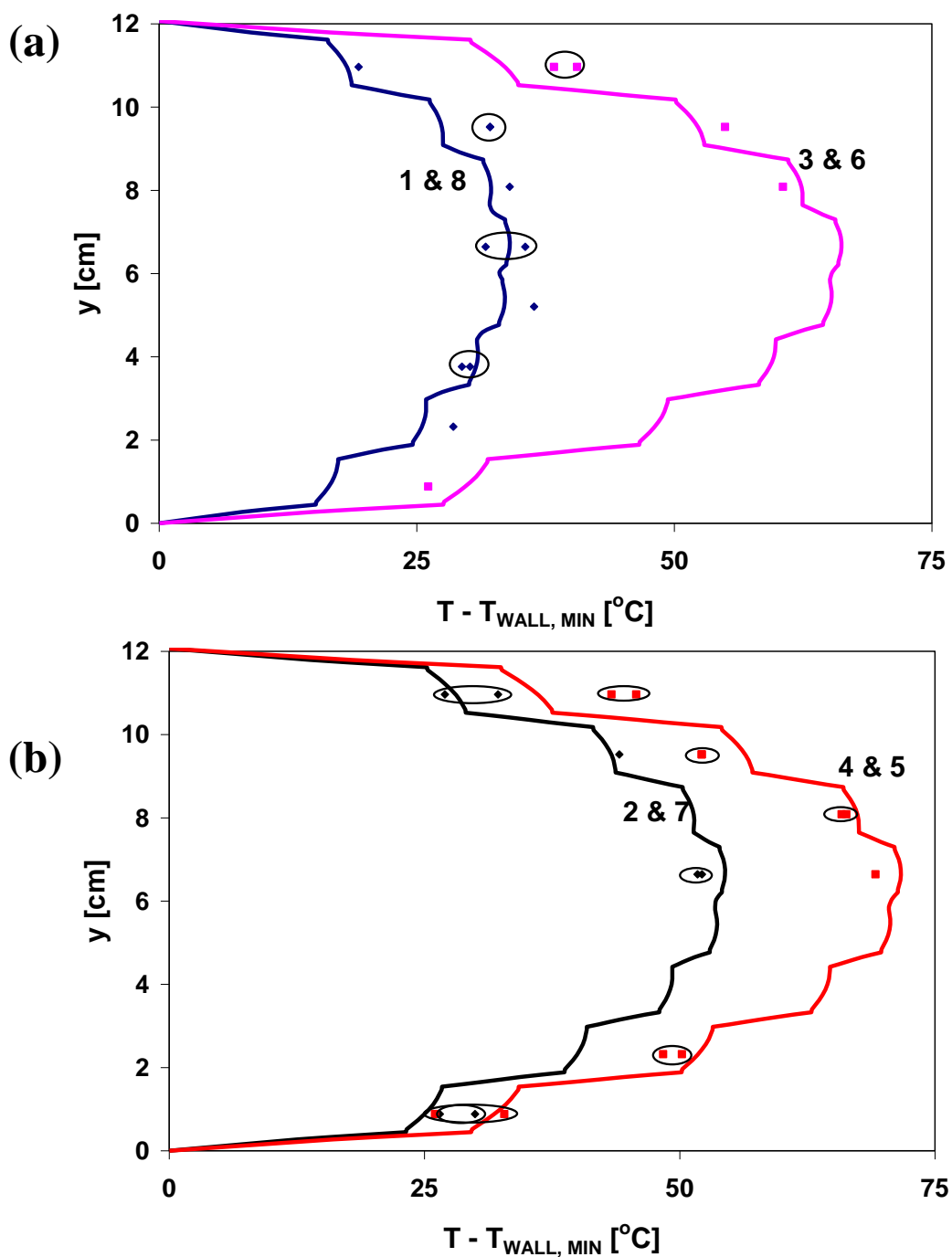


Fig. 25 Measured (symbols) and simulated (lines) mid-plane temperature difference versus y-location for horizontal orientation at $Q = 500$ W, $P = 3$ atm with helium backfill. Ovals are used when two measurements were acquired for in paired columns. Results from the following symmetric columns are paired together, (a) 1&8 and 3&6 (b) 2&7 and 4&5.

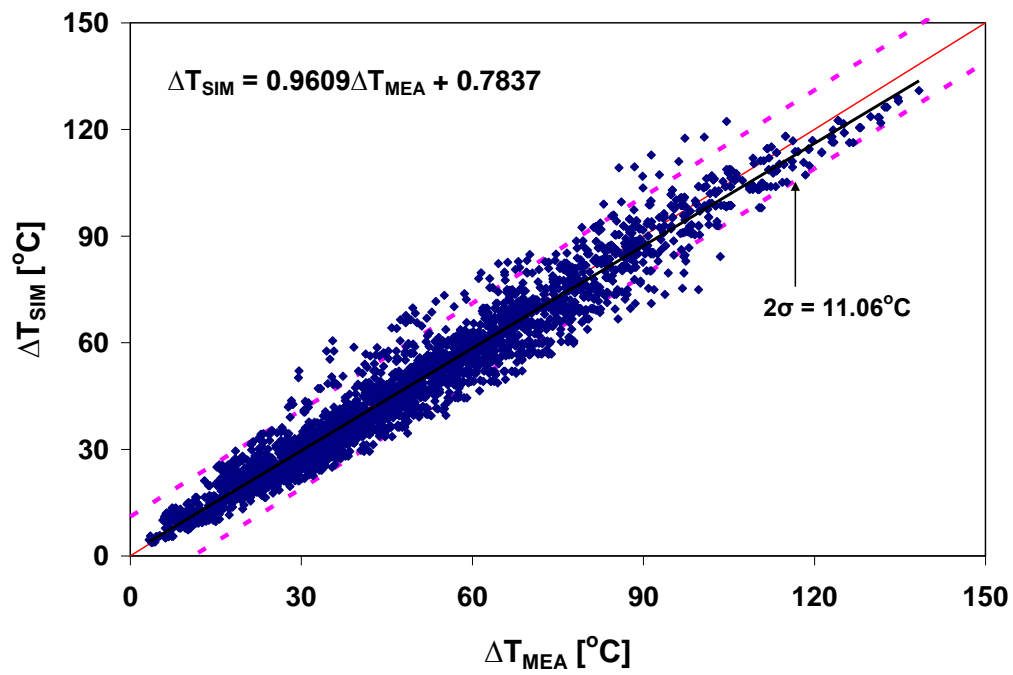


Fig. 26 Simulated versus measured rod temperature differences for all 72 experiments performed

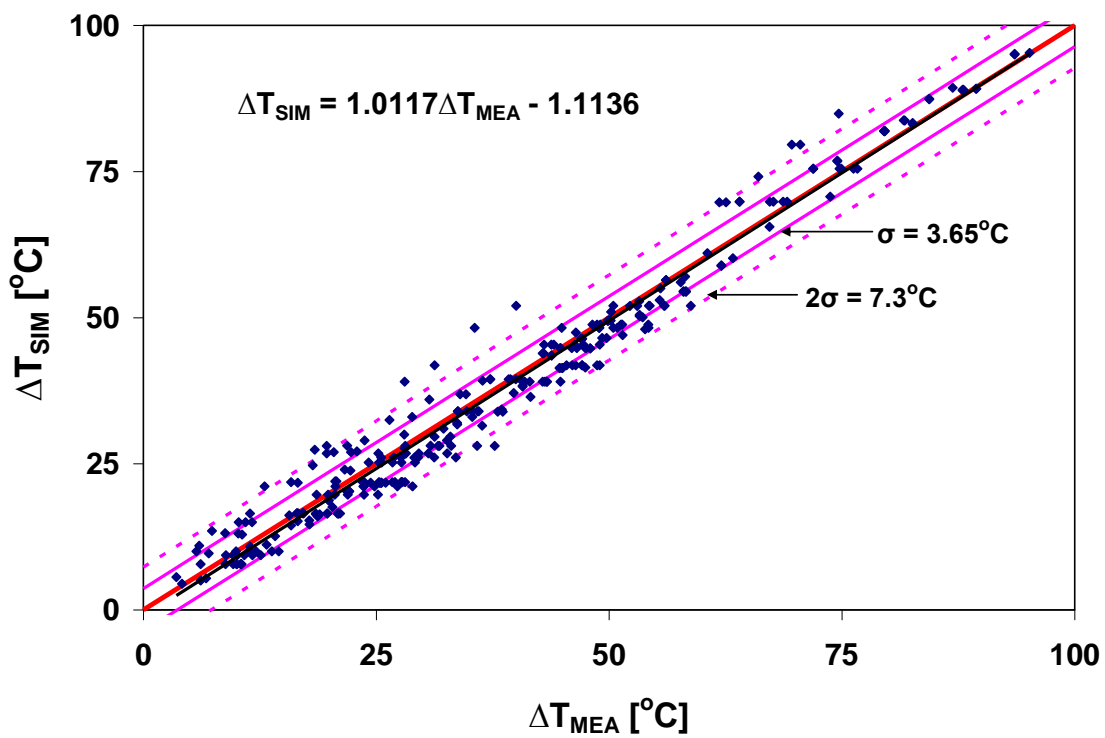


Fig. 27 Simulated versus measured peak temperature differences for all 72 experiments performed

APPENDIX A

NATURAL CONVECTION/RADIATION HEAT TRANSFER SIMULATIONS OF AN ENCLOSED ARRAY OF VERTICAL RODS

ABSTRACT

Experiments performed by Arya and Keyhani [1990] measured the temperature of twelve vertical heated rods within a constant temperature, internally-finned cylindrical enclosure. Measurements were performed with air and helium in the enclosure for ranges of rod heat generation rate and gas pressure. In the current work, steady three-dimensional computational fluid dynamics simulations of conduction, natural convection and radiation heat transfer within the experiment were conducted to benchmark the simulation techniques. In the computational model, different thermal conductivities were applied to a spacer plate between a plate that held the heaters, and one of the enclosure endplates. This was done to model a range of contact resistance between the plates. This was necessary because the experimental endplate conditions were not completely documented. The calculations accurately reproduced the local and average temperatures when a high contact resistance was modeled. These results emphasize that conditions far from data measurement locations can affect experimental results. Those conditions must be well documented if they are to be used to benchmark computational methods.

INTRODUCTION

Nuclear fuel assemblies consist primarily of zircaloy tubes held in square arrays by periodic spacer plates [1]. Boiling water reactor (BWR) assemblies vary from 7x7 to 9x9 arrays, while pressurized water reactor (PWR) assemblies vary from 14x14 to 18x18. The majority of

tubes contain stacked uranium dioxide pellets. The remaining instrument sheath and guide thimble tubes are hollow. BWR assemblies have zircaloy channels around the tube array.

After the assemblies are used in power reactors, the fuel pellets are highly radioactive and generate heat [2]. Spent fuel is typically stored under water for a period of time to allow its heat generation and radioactive decay rates to decrease. It is then moved to thick-walled casks for dry storage or offsite shipment. In the casks, individual assemblies are supported within the square cross-section opening of a basket structure that holds multiple fuel assemblies. The region of the cask containing the fuel and basket is evacuated and backfilled with helium or another non-oxidizing cover gas. In transport, the fuel rods are oriented horizontally. In storage, however, the packages are frequently placed so that the fuel rods are in a vertical orientation.

The zircaloy cladding provides an important containment boundary and its temperature must not exceed 400°C during normal conditions [3]. Solar heat flux and heat generated by the fuel make the package hotter than its surroundings [4, 5]. Package designers and operators must calculate the maximum or peak cladding temperature for different fuel heat generation rates to assure that it does not exceed the allowed limit. The cask thermal dissipation capacity [6] is the fuel heat generation rate that brings the peak clad temperature to its limit. Cask operators can use this capacity to determine how many spent fuel assemblies may be safely loaded into a cask, and/or how long spent fuel must be aged under water before being loaded.

Finite element models of loaded packages are employed to predict cask and fuel temperatures [4, 5]. In the past, computational resources were not available to accurately model the many fuel rods within the multiple fuel assemblies. The rods and cover gas within each basket opening were therefore replaced with homogenized models consisting of solid elements with a uniform heat generation rate. Temperature-dependent effective thermal conductivities

(ETC) were applied to these elements [4, 7, 8, and 9]. They were developed to model the effects of conduction and radiation heat transfer in the directions normal to the rod axes.

Manteufel and Todreas [8] developed an analytical model for one-dimensional conduction and radiation within a rectangular array of heated fuel rods immersed in stagnant gas. They used this model to calculate a temperature-dependent ETC for the region within the fuel assembly, and a conductance model for the thin band between the assembly envelope and the basket walls. This model neglects possible two-dimensional heat transfer effects at the corners, hollow instrument sheath and guide thimble tubes, and external channels, and also natural convection. Manteufel and Todreas used the ETC models they developed to conduct simulations of experiments that had been performed by other investigators. The simulations consistently over-predicted the measured maximum cladding temperature.

Bahney and Lotz [9] performed two-dimensional finite element simulations of conduction and radiation heat transfer within the fuel assembly/backfill gas region. They constructed one-quarter models of several BWR and PWR fuel assemblies. These geometrically-accurate models included unheated instrument sheath and guide thimble tubes, and external channels. The maximum cladding temperature was determined as functions of the assembly heat generation rate and basket wall temperature. These simulations employed a uniform wall temperature to model the fuel assembly/backfill gas cells near the package center, where the hottest fuel cladding resides. Effective thermal conductivity models of these regions were developed based on the simulation results. These models neglect the effect of non-uniform basket wall temperatures and natural convection. The symmetry condition that allowed one-quarter meshes to model full assemblies is not described, and mesh independence was not explicitly demonstrated. The results were not compared to experimental data.

A shortcoming of using thermal conductivity models to calculate temperatures within fuel assembly/backfill gas regions is that they approximate heat flux at a location based only on the temperature and its spatial gradient at that location. This is not universally appropriate when thermal radiation and/or natural convection effects are significant. Radiant heat flux at a location is affected by temperatures at a distance. Natural convection is affected by the local fluid velocity, which depends on temperatures at other locations.

Current computational resources allow the use of meshes that accurately model the many fuel rods and unheated assembly components within a cask. Gomez-Araya and Greiner [10, 11] have conducted two-dimensional simulations of geometrically-accurate PWR and BWR assemblies within uniform temperature basket openings. These simulations have determined the conditions when buoyancy induced gas motion affects peak cladding temperature, as well as the sensitivity to cladding surface emissivity and geometric variations.

Venigalla and Greiner [12] and Gudipati and Greiner [13] performed two-dimensional simulations of whole truck and rail transport casks that included geometrically accurate fuel rods in each basket opening. These simulations used the FLUENT commercial computational fluid dynamics (CFD) package. Simulations that included buoyancy-induced cover gas motion gave temperatures that were very close to those from stagnant gas simulations (in which the gas speed was set to zero). This indicates that natural convection does not strongly affect temperatures within the horizontal transport cask. Results from these geometrically-accurate simulations were compared with a homogenized fuel model using the Manteufel and Todreas [8] ETCs. The geometrically accurate models predicted lower cladding temperatures and higher cask thermal dissipation capacities than the homogenized fuel model.

If the higher cask thermal dissipation capacities can be confirmed, spent fuel may not need to be aged underwater for as long a period as indicated by the earlier homogenized models before being safely transferred to dry storage or transport casks. The computational methods used in the geometrically accurate simulations must be benchmarked against relevant experimental data before it can be used with confidence.

Lovett [14] measured the temperature of an 8x8 array of heated horizontal rods within an aluminum enclosure. Experiments were performed for different gases in the enclosure, and ranges of gas pressure and rod heating rates. These conditions are similar to those of a BWR assembly within a transport cask. Fluent simulations of the experiments were performed that employed different assumptions regarding the thermal conditions of the endplates that held the heaters [15]. This was necessary because the endplate conditions were not completely documented. For a certain set of endplate assumptions, the simulation results accurately reproduced the experimental results. This suggests that all of the boundary conditions of an experiment must be well known if they are to be used to benchmark a simulation.

Arya and Keyhani [16, 17] performed an experiment in which twelve vertical heated rods were enclosed within an internally finned brass tube, as seen in Fig. 1. These conditions are similar to spent fuel within a vertical storage cask. The rod temperatures were measured at different elevations for a range of heat generation rates. Experiments were performed with helium and with air at a range of pressures (including a near vacuum). The close spacing between the rods, enclosure walls and fins in this experiment caused the flow to be steady at the lower heat generation rates. This experiment was chosen for benchmarking CFD in this work because preliminary simulations within a typical fuel assembly/cover gas region show that its

natural convection is steady. Moreover, steady flows are less computationally intensive to simulate than unsteady ones.

PURPOSE OF WORK

In the current work, three-dimensional simulations of the Arya and Keyhani experiment are performed. Since the experiment was performed by other investigators, the details of the test facility, thermal boundary conditions, and experimental method are not completely known. The current simulation results are compared to the experimental data for the following purposes: (a) to develop methods to compare simulation results with measured data and use them to assess the computational methods, (b) to determine appropriate boundary conditions and material properties (some of which are not reported by Arya and Keyhani) that bring the simulation results as close as possible to the data, and (c) to gain information that may be useful to us in developing future benchmark experiments.

ARYA AND KEYHANI EXPERIMENT

Figures 1a and 1b show horizontal and vertical cross sections through the experimental apparatus used by Arya and Keyhani [16, 17]. The apparatus is a one-twelfth scaled model of a Material Retrievable Storage cask [18]. The enclosure is an internally-finned brass tube. Its inner diameter, length and wall thickness are $D = 13.97$ cm, $L = 48.6$ cm, and $T = 0.32$ cm, respectively. Eight brass fins are silver soldered to its inner surface, with equal angular spacing. All are 34.9 cm in the vertical direction and 0.32 cm thick. Four are 6.84 cm wide in the radial direction and divide the enclosure into four quadrants. Between the long fins, shorter fins that

are 2.59 cm wide in the radial direction each equally bisect the quadrant. Two 20 cm diameter, 0.95 cm thick brass flanges are silver soldered to each end of the cylinder.

Two 0.95-cm-thick, 20-cm-diameter brass end plates are fastened to the flanges. The enclosure is not gas tight and gas is constantly supplied to the enclosure through a regulator connected to a port in the top endplate. It makes up for losses and maintains the desired pressure. Experiments are performed for air and helium at pressures of $P = 1$ to 8 atm, and near vacuum. Two separate cooling coils on the upper and lower portions of the enclosure outer surface are used to maintain it at a nearly uniform temperature.

Within the enclosure are twelve vertical Watlow Firerod cartridge heaters of diameter 2.54 cm and length 34.3 cm. Within each quadrant the rod center-to-center spacing is 3.2 cm. From quadrant to quadrant, the center-to-center spacing is 3.8 cm. Each rod is composed of a compressed powder magnesium oxide (MgO) core encapsulated within an Incoloy sheath of 1.2 mm thickness. Electrical current flows through a coiled wire within the MgO. It generates heat uniformly along the rod length except for 12.7 mm (0.5 inch) unheated regions at each end. The heaters are wired together so that all twelve generate the same amount of heat. The heaters are held in place with two 1.27 cm thick, 13.94 cm diameter phenolite guides at their top and bottom. The heater power wires are connected to another phenolite plate above the heaters, and exit the enclosure through a Conax brand feed-through in the top endplate. Experiments are performed for rod heat loads from $Q = 1$ to 16 W/rod.

There are 24 thermocouple beads fastened to the outer surfaces of the rods. Their lead wires run to the top of the chamber and exit through two feed-through connectors in the top end plate. Due to the symmetry of the geometry and thermal boundary conditions, the four central rods are expected to have nearly the same temperature profile. They are all referred to as Rod 1.

The eight outer rods are also expected to have nearly the same temperatures and are collectively referred to as Rod 2 (numbers 1 and 2 are placed on the appropriate rods in Fig. 1a).

Either two or three thermocouples are fastened to each rod. Most are placed at the angular positions closest to the enclosure center at the following five elevations above the enclosure floor: $z = 5.7, 11.4, 17.2, 22.9$ and 28.6 cm. Data from different rods are combined together to assemble axial profiles for Rod 1 and 2 for each heat generation rate and gas condition. Rod surface temperatures were also made at the angular position farthest from the enclosure center, but these data were not reported. The average enclosure temperature T_{EA} is reported but the phenolite temperatures are not given. The temperature measurement uncertainty is reported to be $\pm 0.2^\circ\text{C}$.

A 0.32 cm thick steel disk is between the lower guide and the brass endplate. No information is given about the thermal contact resistance between these plates. An 11.4 cm high gap above the top phenolite guide facilitates the connection of the heater and thermocouple leads, and contains the same gas that surrounds the heaters.

In this work, certain experiments were selected for study because they did not require unsteady simulations. For the air experiments, simulations were performed for $P = 1$ to 3 atm and $Q = 1$ to 3 W/rod. Air experiments with higher heat loads required unsteady natural convection simulations. Helium simulations were performed for $P = 1$ to 5 atm and $Q = 10$ to 26 W/rod. None of the helium experiments required unsteady natural convection calculations. The enclosure temperatures were nearly the same for all the experiments considered in this paper. T_{EA} varied from 22.0°C to 26.6°C for the air experiments, and 22.9°C to 24.4°C for helium.

Figure 2 shows the Grashof number versus heat generation rate for different gas pressures from the selected air and helium experiments. The Grashof number is the dimensional ratio of buoyancy to viscous forces and is defined as:

$$Gr_D = \frac{g\beta D^3 \rho^2 (T_{R1A} - T_{EA})}{\mu^2}$$

In this expression, g is the acceleration of gravity and T_{R1A} is the average measured temperature of Rod 1. The thermal expansion coefficient, density and dynamic viscosity of the gas β , ρ and μ respectively, are all evaluated at $(T_{R1A} + T_{EA})/2$. The Grashof number increases with Q (which increases $T_{R1A}-T_{EA}$) and P (which increases ρ). The helium experiments were performed at considerably higher heat generation rates than the air tests. However, the helium Grashof numbers are lower due to helium's lower density, higher thermal conductivity (which makes $T_{R1A}-T_{EA}$ smaller) and higher viscosity. The effects of natural convection and flow unsteadiness are expected to increase with as Gr_D increases.

COMPUTATIONAL MODEL

Figure 3 shows a horizontal cross section through the nominal finite volume mesh used for the majority of simulations in this work. It includes the magnesium oxide and Incoloy regions of the heaters, brass enclosure and internal fins, as well as the gas filled region. The three dimensional grid was created by sweeping this x-y-mesh in the z direction. The phenolite guides at the top and bottom of the heaters, and bottom steel and brass plates are included in the three-dimensional mesh. The flanges at the bottom of Fig. 1b, and the gas filled region above the phenolite plate that touches the heaters, are not modeled. The nominal three-dimensional mesh

has 868,068 elements. Coarse and fine grids with 459,264 and 1,685,934 elements, respectively, are used for mesh independence studies.

Conduction is modeled within all solid elements. Temperature dependent thermal conductivities are used for the magnesium oxide, Incoloy, steel, brass and phenolite material. Different sets of simulations were performed with helium (He) or air in the void space at the various pressures. Temperature and pressure dependent gas properties are employed [19-21]. The simulations model laminar natural convection motion and heat transfer using the Boussinesq approximation. Surface-to-surface radiation is modeled across the spaces between solid elements assuming the gas is non-participating. In this work, the emissivity of all interior surfaces is $\epsilon = 0.6$. Future work may consider a range of emissivity values.

A volumetric heat generation equal to $Q/(AL_h)$ [W/m^3] was applied to the MgO regions of each rod. In this expression Q is the heat generation per rod, $A = 5.06 \text{ cm}^2$ the cross sectional area of the MgO regions, and $L_h = 31.8 \text{ cm}$ is the heated length. The top of the phenolite guide holding the top of the heaters, and bottom of the lower brass end plate (see Fig. 1b) are insulated.

In this work, simulations are performed for air and for helium gas at the heat load and pressures for which experimental data is given in Fig. 2. For each simulation a uniform outer wall temperature is applied to the outer vertical surfaces of the computational domain. It is equal to the average measured enclosure temperature for that experimental condition.

The simulations presented in this study were performed using the FLUENT 6.2 finite volume code. FLUENT is a commercial computational fluid dynamics (CFD) software that solves the conservation of mass, momentum and energy constraints in a domain with given boundary conditions. This work uses steady state conditions. The buoyancy induced flow is included by adding the gravitational force and considering temperature dependent density of the

backfill gas. Radiation is solved for gray diffuse surfaces using the surface-to-surface (S2S) method. The governing equations are solved using a finite volume method with the discretized governing equations. The grids are constructed and the governing equations are solved with double precision. A second order upwind scheme is used for solving the momentum and energy equations.

In this work the contact resistance between solid elements is neglected. In order to understand the influence of the contact resistance between the steel plate at the bottom of the apparatus and the phenolite and brass plates touching it, some simulations are performed with the steel thermal conductivity set to zero.

RESULTS

Gas Speed Figure 4 shows simulated contours of the vertical velocity in the plane midway between the top and bottom phenolite guides. Only one-eighth of the plane is shown due to the symmetry of the results. Figure 4a shows results for air with $Q = 1$ W/rod and $P = 1$ atm, and Fig. 4b shows helium with $Q = 26$ W/rod and $P = 3$ atm. Even though these dimensional parameters are quite different, the Grashof numbers for these cases (Fig. 2) are within an order of magnitude. In both cases the location of the maximum upward velocity (marked with a circle) is in the region between Rods 1 and 2. The maximum downward speed (marked with an x) is in the corner to the right of Rod 2.

For the air simulation, the maximum magnitude of the upward (positive) speed is three times larger than the maximum downward (negative) magnitude. Since the net mass flow rate through the plane is zero, this indicates the flow moves downward in a larger fraction of the open

area than it moves upward. For the helium simulation the maximum magnitudes of the upward and downward speeds are roughly equal.

The maximum gas speed S_{MAX} (velocity magnitude) within the domain varies from 1 to 9 cm/s for the air simulations, and 2 to 17 cm/s for helium. Figure 5 shows the simulated Reynolds number as a function of rod heat generation rate Q . Results are shown for helium and for air at different pressures. The Reynolds number is the dimensionless ratio of inertial to viscous forces and is defined as

$$\text{Re}_D = \frac{D\rho S_{MAX}}{\mu}$$

The trends for the simulated Reynolds number in Fig. 5 are very similar to those for the measured Grashof numbers in Fig. 2.

Temperature Profiles Figure 6 shows temperature contours within one-eighth of the plane midway between phenolite guides. Air and helium results in Figs. 6a and 6b, respectively, are for the same pressures and rod heat generation rates as Figs. 4a and 4b. Small circles and X's in the figure show, respectively, the hottest and coldest locations on the surfaces of each rod. In both cases Rod 1 (the one closer to the enclosure center) is hotter than Rod 2. The rod temperatures for air are more nearly uniform than they are for helium.

For pure conduction (no gas motion) the hottest and coldest rod surface locations would be those farthest from and closest to the enclosure external surface, respectively. However, gas motion causes these locations to reverse on Rod 1 (the coldest and hottest locations are, respectively, far from and close to the edge).

Figure 7 shows the rod surface temperature difference versus elevation for Rod 1. This is the difference between the local surface temperature and the average enclosure temperature $T_R - T_{EA}$. Figure 7a is for air at $P = 2$ atm and a heat generation rate of $Q = 1$ W/rod, and Fig. 7b is for helium at $P = 3$ atm and $Q = 26$ W/rod. The symbols with error bars show experimental data with its uncertainty [16, 17]. The solid thicker lines show the maximum and minimum simulated rod surface temperatures at each elevation.

The thinner lines show temperatures from simulations that apply the actual thermal conductivity of steel to the plate between the phenolite and brass plates at the bottom of the apparatus (see Fig. 1b). Those simulations assume no contact resistance between the plates. The thicker lines, marked $k_{plate} = 0$, are results with the spacer plate thermal conductivity set to zero. Those simulations are performed to model very high contact resistance between the steel plate and phenolite guide. Arya and Keyhani do not give any information about that contact.

The $k_{plate} = 0$ simulations give higher rod temperatures especially at the bottom of the rods. The measured temperatures at the bottom of the enclosure are better characterized by the thick lines than by the thin ones. This trend is observed in both gases and for the other gas pressures. We conclude that there is a significant thermal resistance between the bottom phenolite guide and steel plate, and it must be included in the computational model. We use $k_{plate} = 0$ in all subsequent calculations in this paper.

Figures 8 and 9 show measured (symbols with error bars) and simulated (lines) rod surface temperature difference versus elevation for Rods 1 and 2. The solid and dashed lines show the maximum and minimum simulated temperature for each rod. Figure 8 presents results for air at $Q = 1$ W/rod, and Fig. 9 is for helium with $Q = 26$ W/rod. Different plots show results

for different gas pressures (the pressures and heating rates in these figures are the only ones for which local temperature measurements are available [16, 17]).

Results from the nominal computational mesh are presented at each condition. Fine and coarse mesh results for the maximum rod temperature are also presented for air at $P = 1$ and 3 atm in Figs 8a and 8c, and for helium at $P = 2$ and 5 atm in Figs. 9a and 9d. The maximum difference for the different meshes is 0.5%, which is indistinguishable in the figures. This indicates the results of these simulations are mesh-independent.

For air, the maximum difference between the hottest and coldest surface locations (solid and dashed lines) is 0.3°C . For helium it is 8°C . At low pressures ($P \leq 2$ atm) and in both gases, the simulated temperature profiles peak nearly midway between the upper and lower phenolite guides. This is the expected shape if there is no fluid motion, and heat is transferred by conduction and radiation only. At higher pressures, the peaks of the simulated temperature profiles are above the mid-height.

For both gases, at each pressure and on both rods, the temperature at the highest measurement elevation is greater than it is at the lowest elevation. The temperature difference between those locations increases as pressure increases. This is an indication of the increased effect of natural convection. The simulated temperature profile shapes change as the pressure increases, with the hottest locations moving to higher elevations. However, the measurements do not show this shift as dramatically as the simulations.

For air, all thirty of the measured surface temperatures are bracketed by the simulated maximum and minimum temperatures. For helium, ten of the forty measured temperatures are above the simulated range. They are all located near the enclosure mid-height. Moreover, for helium, the hottest measured temperature on Rod 1 is always located at the mid-height. We do

not have enough information about the experiment to know why the mid-height locations are hotter than the simulations.

Average Temperatures Figures 10 and 11 show the difference between average temperature of Rod 1 and the enclosure, $T_{R1A}-T_{EA}$, versus rod heat generation rate for different gas pressures. Experimental data are presented using symbols and simulated results are shown using lines. Results for air and helium are given in Figs. 10 and 11, respectively.

The measured temperature difference increases with heat load and decreases with gas pressure. For air the temperature decreases more rapidly as pressure increases at the highest heat load than at the lower two loads. For helium, the dependence on gas pressure is not as strong as it is for air.

For air, the simulated average temperature differences for Rod 1 are within 1% of the data. For Rod 2, the simulated average is 1% to 8% above the measured values. The simulated average for all rods is 1% to 4% above the data. For helium, the simulated average temperature differences for Rod 1 are less than 1% below the data. For Rod 2, the simulated average temperature difference is 6% to 15% above the measured values. The simulated average for all rods is 2% to 7% above the data.

SUMMARY

Experiments performed by Arya and Keyhani [16, 17] measured the temperature of twelve vertical heated rods within a constant temperature, internally-finned cylindrical enclosure. Measurements were performed with air and with helium in the enclosure for ranges of rod heat generation rate and gas pressure. In the current work, steady three-dimensional computational fluid dynamics simulations of conduction, natural convection and radiation heat transfer within the experiments were conducted to benchmark the simulation techniques. In the computational

model, different thermal conductivities were applied to a spacer plate between a plate that held the heaters, and one of the enclosure endplates. This was done to model a range of contact resistance between the plates. This was necessary because the experimental endplate conditions were not completely documented. The calculations accurately reproduced the local and average temperatures when a high contact resistance was modeled. These results emphasize that conditions far from the measurement locations can affect experimental results. Those conditions must be well documented if they are to be used to benchmark computational methods.

NOMENCLATURE

D	inner diameter of the enclosure cylinder
g	gravitational constant
Gr_D	Grashof number based on enclosure inner diameter
P	pressure
Q	rod power input (W/rod)
S_{MAX}	Maximum gas speed
Re_D	Reynolds number based on enclosure inner diameter
T_{R1A}	average temperature of rod 1
T_{EA}	average temperature of the enclosure cylinder
z	Elevation about enclosure floor
β	volumetric thermal expansion coefficient
ρ	Gas density
μ	gas dynamic viscosity

ACKNOWLEDGMENT

This work was sponsored by the US Department of Energy, through Sandia National Laboratories under contract DE-C04-94AL85000, and by its Global Nuclear Energy Partnership (GNEP) under contract DEFC07-06ID14782.

REFERENCES

- [1] U.S. Dept. of Energy, Office of Civilian Radioactive Waste Management (OCRWM), 1987, "Characteristics of Spent Nuclear Fuel, High-Level Waste, and Other Radioactive Wastes Which May Require Long-Term Isolation", DOE/RW-0184.
- [2] Saling, J.H. and Fentiman, A.W., 2001, *Radioactive Waste Management*, 2nd Edition, Taylor and Francis, New York.
- [3] NRC, 2005 "Cladding Considerations for the Transportation and Storage of Spent Fuel," Interim Staff Guidance Report for the Spent Fuel Project Office of the U.S. NRC, ISG-11 R3; available at www.nrc.gov
- [4] General Atomics (GA), 1998, "GA-4 Legal Weight Truck From-Reactor Spent Fuel Shipping Cask, Safety Analysis Report for Packaging (SARP)," San Diego, California 92186-5608.
- [5] Office of Civilian Radioactive Waste Management (OCRWM), US Department of Energy, 1993, "Multi-Purpose Canister (MPC) Implementation Program Conceptual Design Phase Report," DOC ID: A20000000-00811.

[6] Greiner, M., Gangadharan, K.K., and Gudipati, M., 2007, "Use of Fuel Assembly/Backfill Gas Effective Thermal Conductivity Models to Predict Basket and Fuel Cladding Temperatures within a Rail Package During Normal Transport," *Nuclear Technology*, Vol. 160, pp. 325-336.

[7] Unterzuber, R., Milnes, R.D., Marinkovich, B.A., and Kubancsek, G.M., 1982, "Spent-Fuel Dry-Storage Testing at E-MAD (March 1978 through March 1982)," prepared for the US DOE Commercial Spent Fuel Management Program Office at the Pacific Northwest Laboratory, B-D3339-A-G.

[8] Manteufel, R. D. and Todreas, N. E., 1994, "Effective Thermal Conductivity and Edge Conductance Model for a Spent-Fuel Assembly", *Nuclear Technology*, Vol. 105, pp. 421-440.

[9] Bahney, R. H. and Lotz, T. L., 1996, "Spent Nuclear Fuel Effective Thermal Conductivity Report" U.S. DOE, Yucca Mountain Site Characterization Project Office, D.I.: BBA000000-01717-5705-00010 REV 00.

[10] Gomez, P.E.A., and Greiner, M., 2006, "2D Natural Convection and Radiation Heat Transfer Simulations of a PWR Fuel Assembly within a Constant Temperature Support Structure PVP2006-ICPVT-11-93332, Proceedings of PVP2006-ICPVT-11, 2006 ASME Pressure Vessels and Piping Division Conference, July 23-27, Vancouver, BC, Canada.

[11] Araya, P.E. and Greiner, M., 2007, "Use of Regular Rod Arrays to Model Heat Transfer from BWR Fuel Assemblies inside Transport Casks," *Packaging, Transport, Storage and Security of Radioactive Material*, Vol. 18, pp. 171-179.

[12] Venigalla, V.V.R., and Greiner, M., 2007, CFD Simulations of Natural Convection/Radiation Heat Transfer within the Fuel Regions of a Truck Cask for Normal Transport," PVP2007-26242, Proceedings of the 2007 ASME Pressure Vessels and Piping Division Conference, July 22-26, 2007, San Antonio, Texas.

[13] Gudipati, M., and Greiner, M., 2007, "CFD Simulations of Fuel Cladding and Basket Surface Temperatures in an MPC Rail Cask during Normal Transport," proceedings of the 15th International Symposium on the Packaging and Transportation of Radioactive Materials (PATRAM).

[14] Lovett, P. M., 1991, "An Experiment to Simulate the Heat Transfer Properties of a Dry, Horizontal Spent Nuclear Fuel Assembly," M.S. Thesis, Nuclear Eng., Massachusetts Institute of Technology

[15] Gomez, P.E.A., and Greiner, M. 2006, "Benchmark Natural Convection/Radiation Simulations within an Enclosed Array of Horizontal Heat Rods," PVP2006-ICPVT-11-94021, Proceedings of PVP2006-ICPVT-11, 2006 ASME Pressure Vessels and Piping Division Conference, July 23-27, Vancouver, BC, Canada.

[16] Arya, S., 1990, "Convective Heat Transfer in a Sealed Vertical Storage Cask Containing Spent Fuel Canisters," M.S. Thesis, Mechanical Engineering Department, University of Tennessee, Knoxville.

[17] Arya, S., and Keyhani, M., 1990, "Convective Heat Transfer in a Sealed Vertical Storage Cask Containing Spent Fuel Canisters," *Nuclear Science and Engineering*, Vol. 105, pp. 391-403.

[18] U.S. Department of Energy, Richland Operations Office, 1985, "Integral Monitored Retrievable Storage (MRS) Facility-Conceptual Design Report," prepared by The Ralph M. Parsons Company of Delaware, Westinghouse Electric Corporation, and Golden Associates, Report No. MRS 11, contract DE-AC06-84RL 10436.

[19] Hands, B.A.; Arp, V.D., 1981, *A Correlation of Thermal Conductivity Data for Helium*, Cryogenics, 697-703; available at <http://webbook.nist.gov/chemistry/fluid/>, as of 04-10-2006.

[20] McCarty, R.D.; Arp, V.D., 1990, *A New Wide Range Equation of State for Helium.*, Adv. Cryo. Eng, 1465-1475; available at <http://webbook.nist.gov/chemistry/fluid/>, as of 04-10-2006.

[21] Arp, V.D., McCarty, R.D.; Friend, D.G., 1998, "Thermophysical Properties of Helium-4 from 0.8 to 1500 K with Pressures to 2000 MPa," Technical Note 1334, National Institute of Standards and Technology, Boulder; available at <http://webbook.nist.gov/chemistry/fluid/>, as of 04-10-2006.

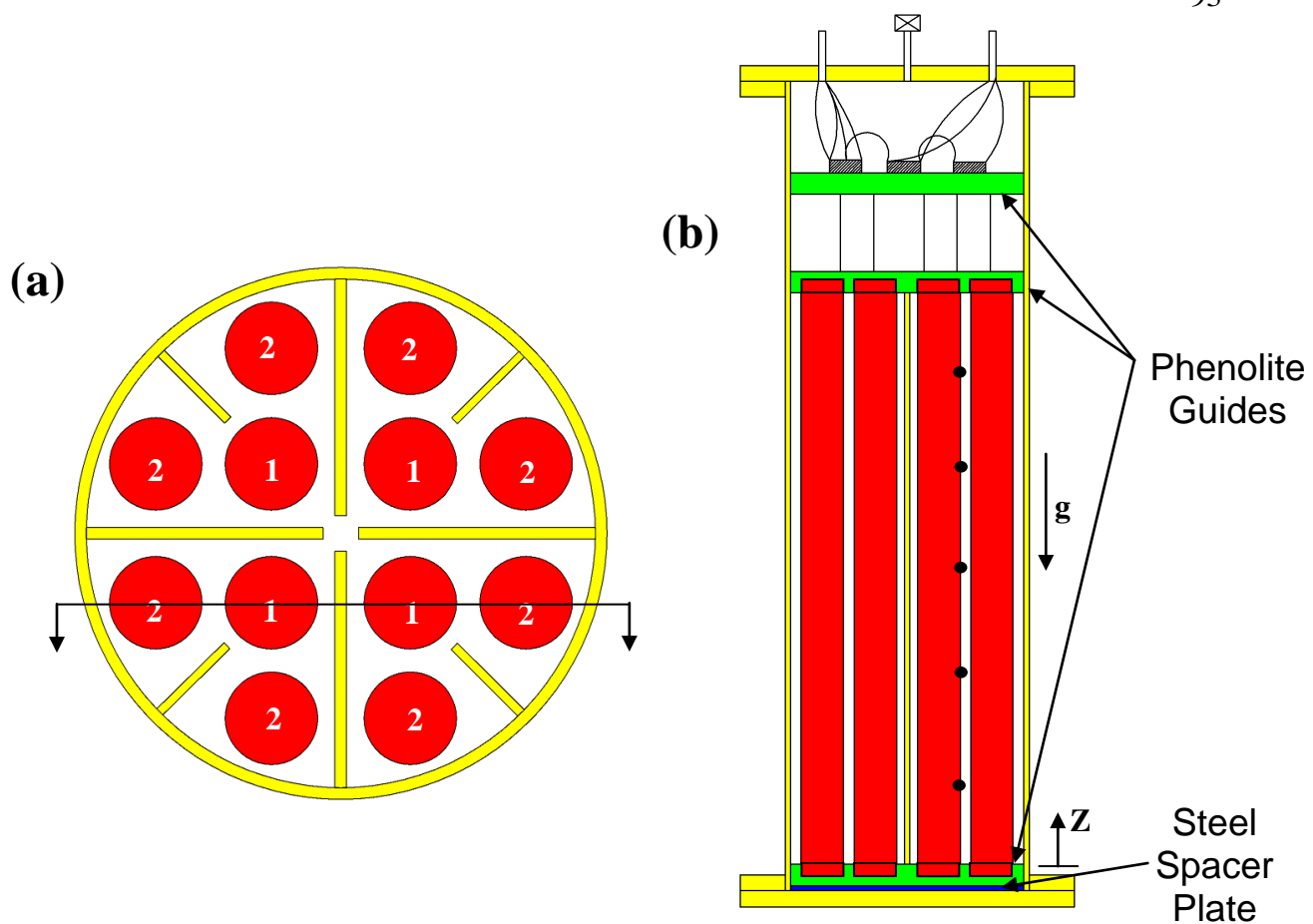


Figure 1 Experimental apparatus cross sections [16, 17] (a) Horizontal (b) Vertical

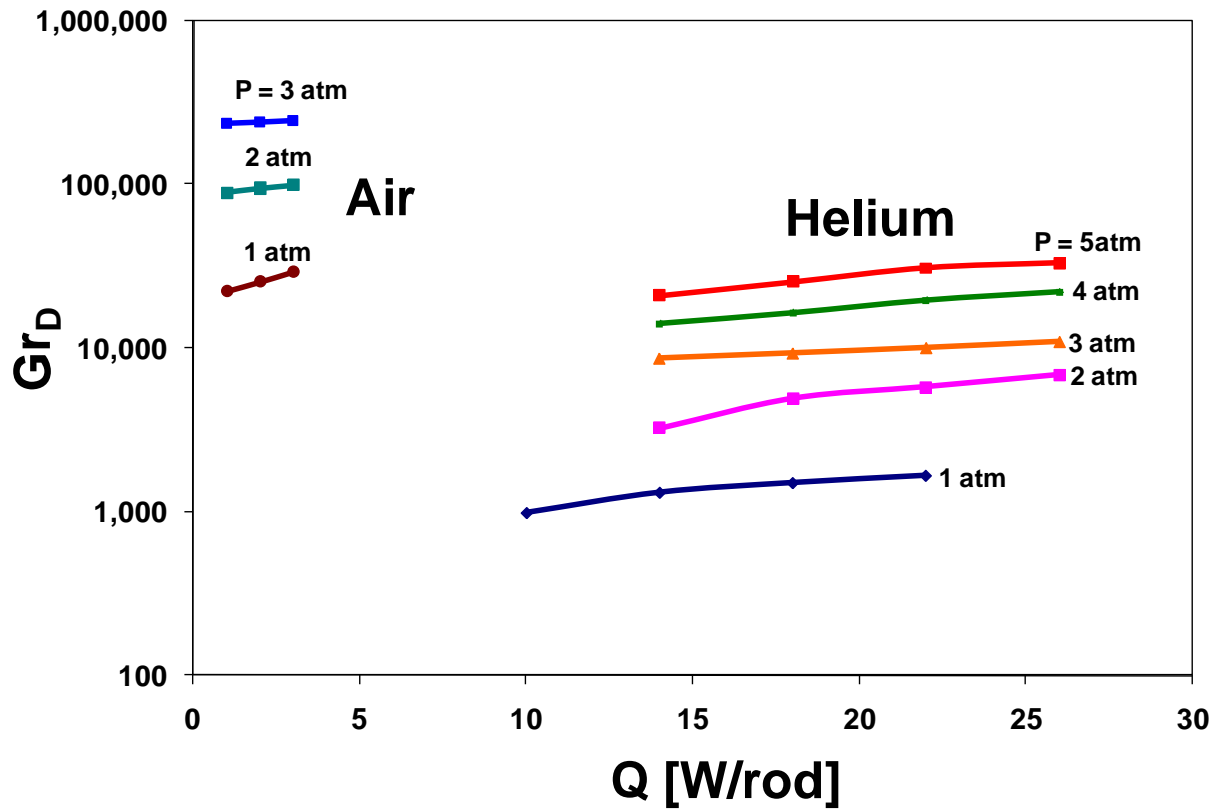


Figure 2 Experimental [16, 17] Grashof number versus heat generation rate for air and helium and different gas pressures

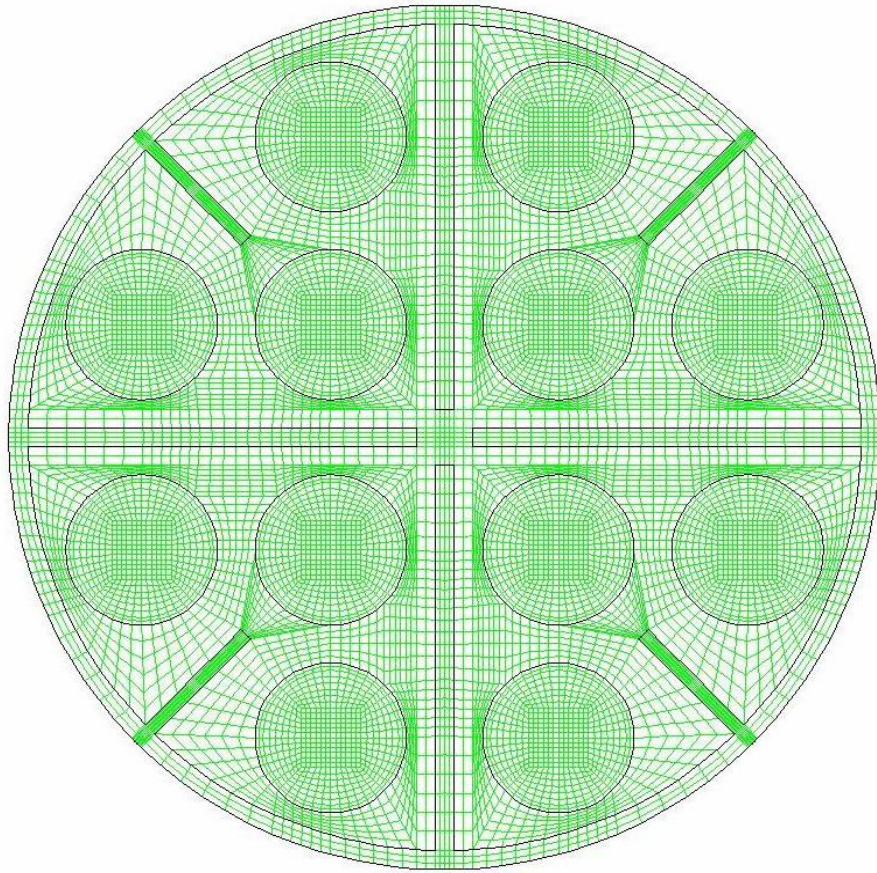


Figure 3 Horizontal cross section through the coarse three-dimensional computational mesh

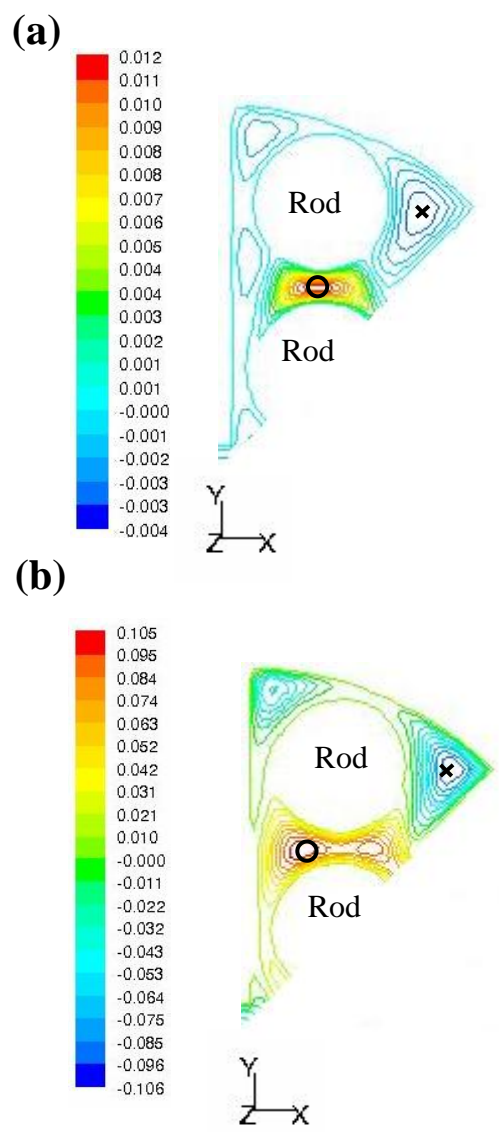


Figure 4 Vertical velocity component contours in one-eighth of the mid-height cross-section. Circles and X's show the location of the maximum upward and downward speeds respectively. (a) Air with $Q = 1$ W/rod and $P = 1$ atm. (b) Helium for $Q = 26$ W/rod and $P = 3$ atm.

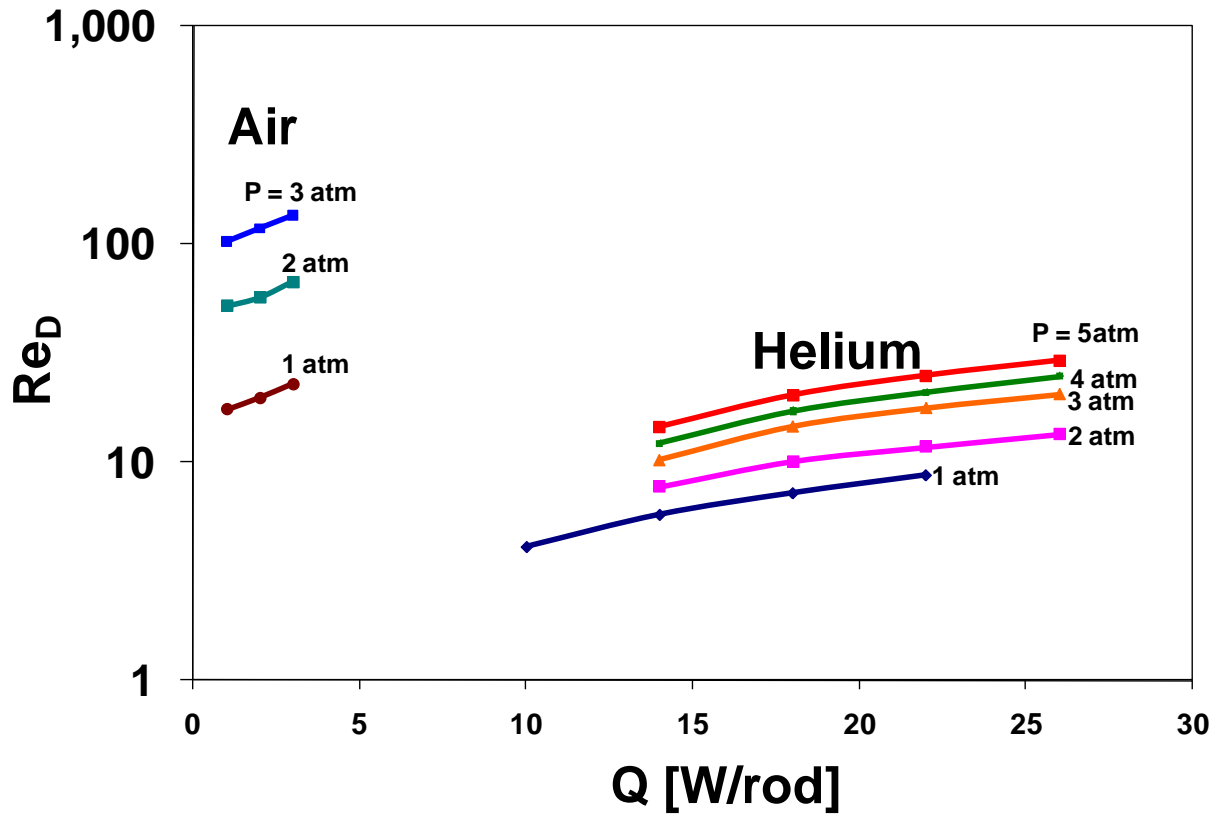


Figure 5 Simulated maximum Reynolds Numbers within the domain versus rod heat load for different gases and pressures.

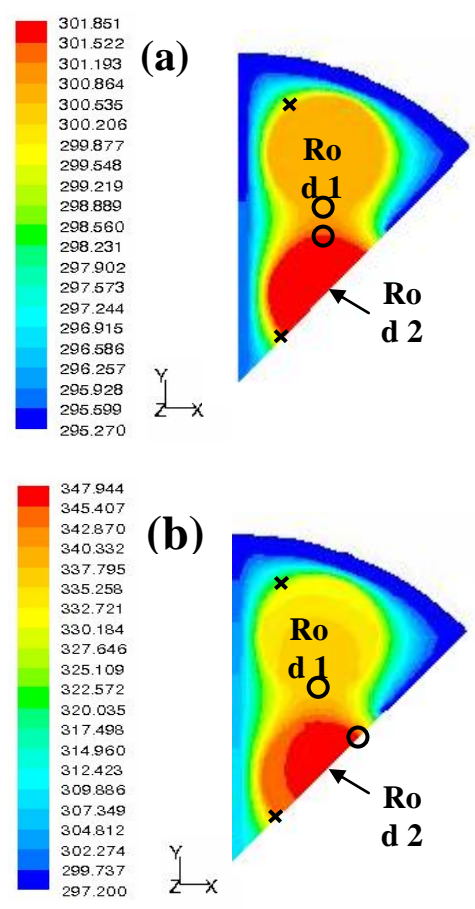


Figure 6 Temperature contours in one-eighth of the cross-section at the mid-height. Circles and X's show the hottest and coldest rod locations for each rod (a) Air with $Q = 1$ W/rod and $P = 1$ atm (b) Helium for $Q = 26$ W/rod and $P = 3$ atm

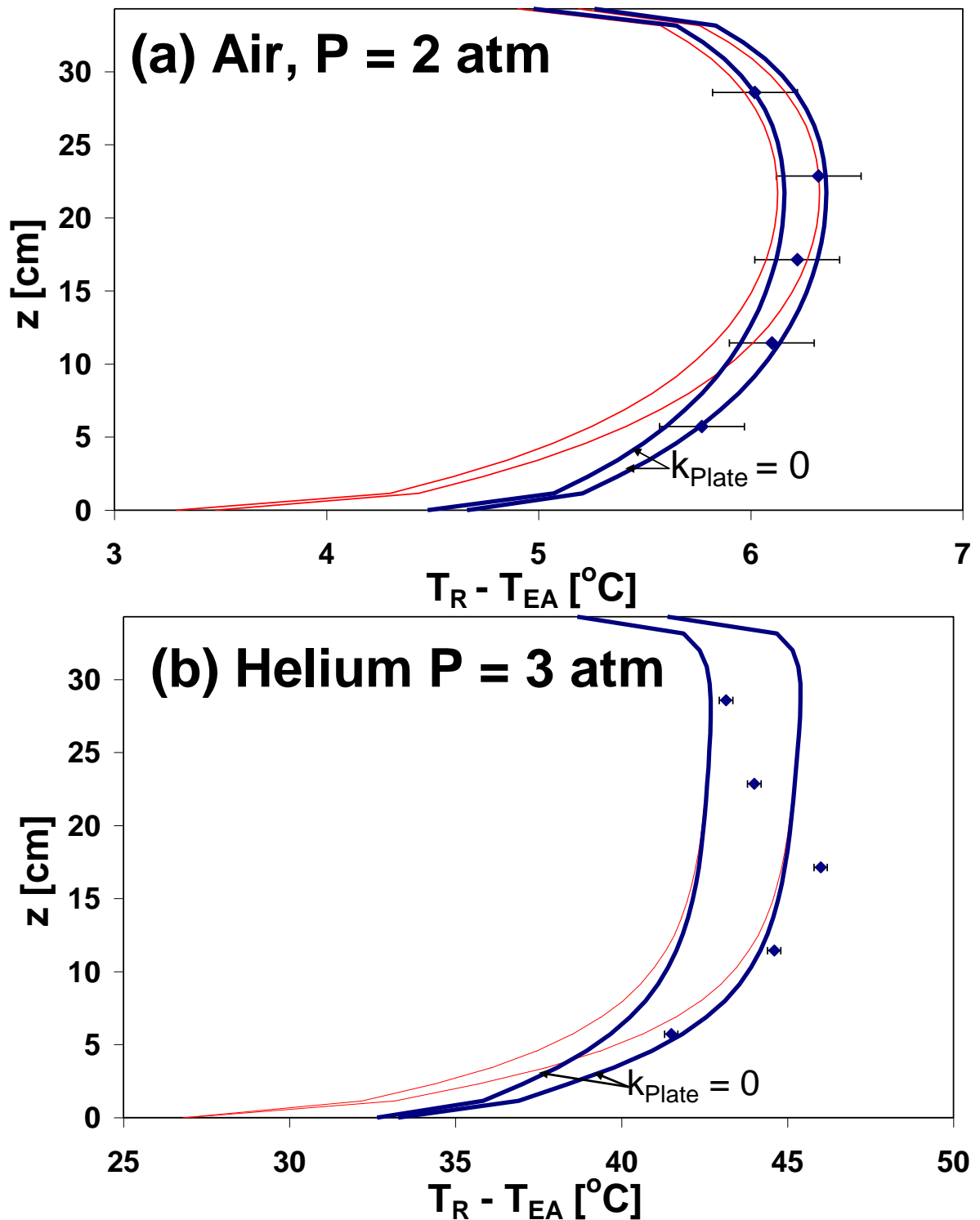


Figure 7 Measured and simulated maximum and minimum rod/enclousure temperature difference versus elevation. Thin lines show simulation results using steel conductivity for the bottom spacer plate. Thick lines marked $k_{\text{Plate}} = 0$, show results for an insulating plate. (a) Air with $P = 2$ atm and $Q = 1$ W/rod. (b) Helium with $P = 3$ atm and $Q = 26$ W/rod.

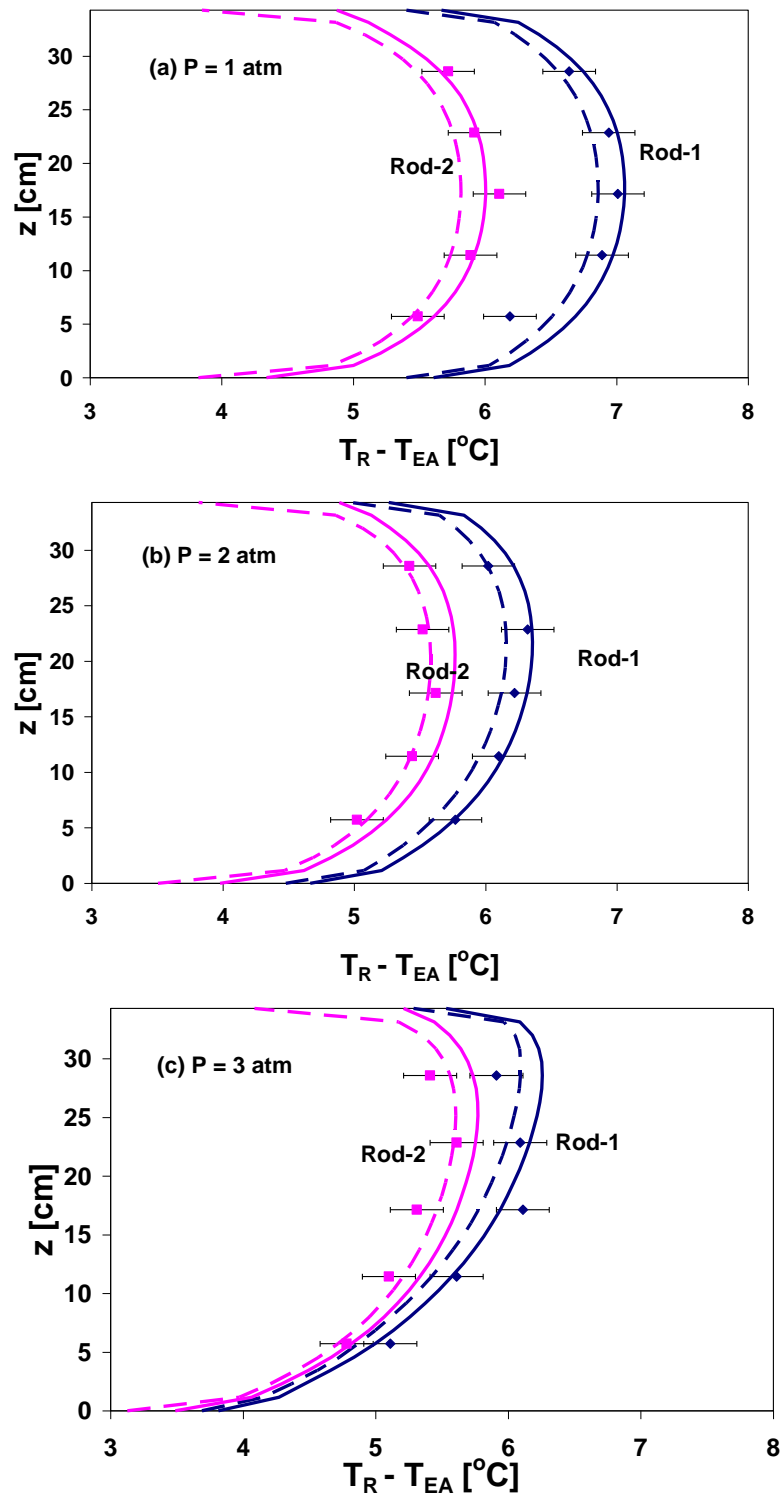


Figure 8 Simulated (maximum and minimum) and measured rod surface temperatures versus elevation for air with $Q = 1$ W/rod from nominal mesh calculation (a) $P = 1$ atm. (b) $P = 2$ atm. (c) $P = 3$ atm. Fine and coarse mesh results are presented for $P = 1$ atm and 3 atm.

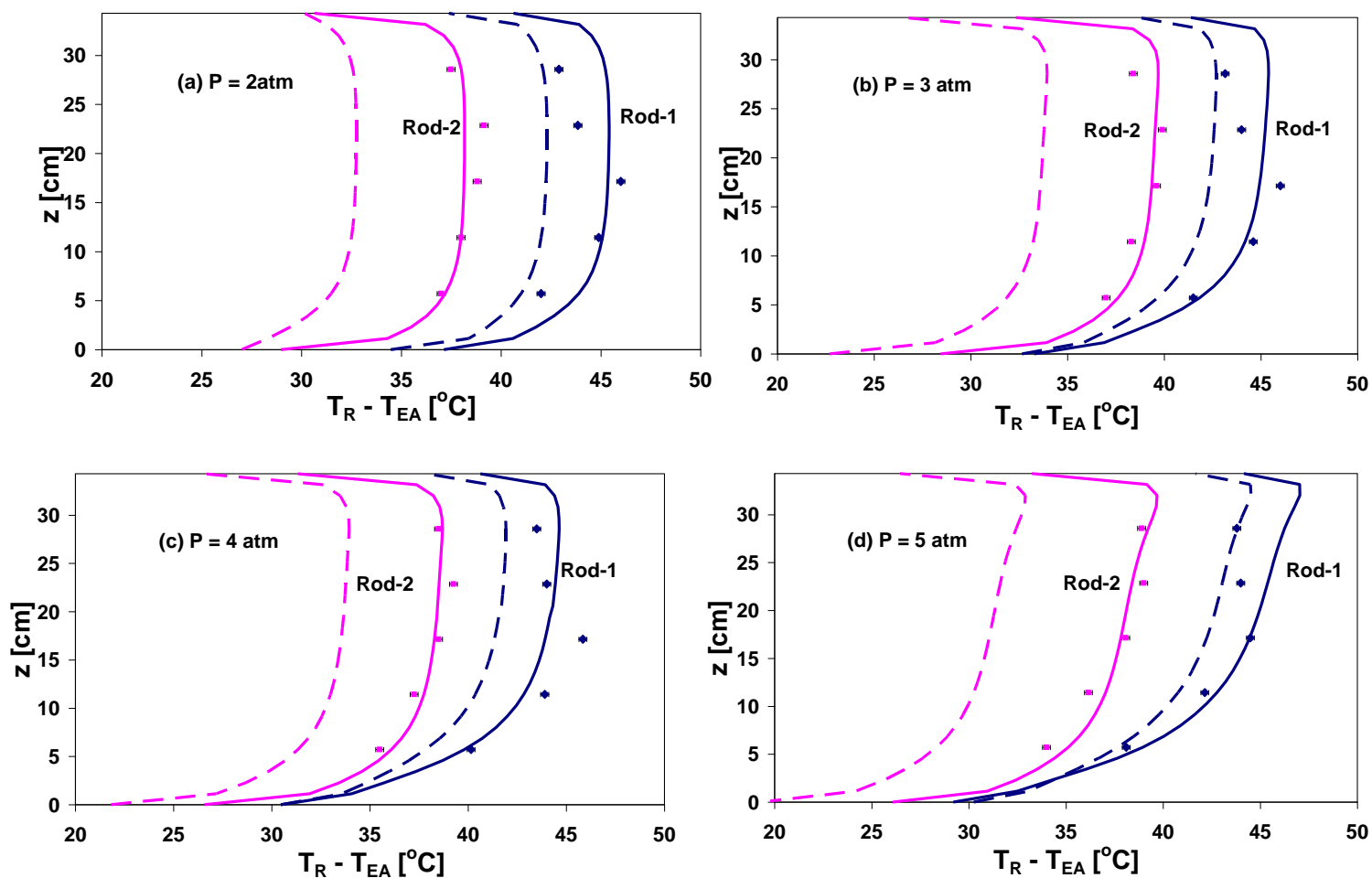


Figure 9 Simulated (maximum and minimum) and measured rod surface temperatures versus elevation for helium with $Q = 26$ W/rod from nominal mesh calculation (a) $P = 2$ atm. (b) $P = 3$ atm. (c) $P = 4$ atm (d) $P = 5$ atm. Fine and coarse mesh results are presented for $P = 2$ and 5 atm.

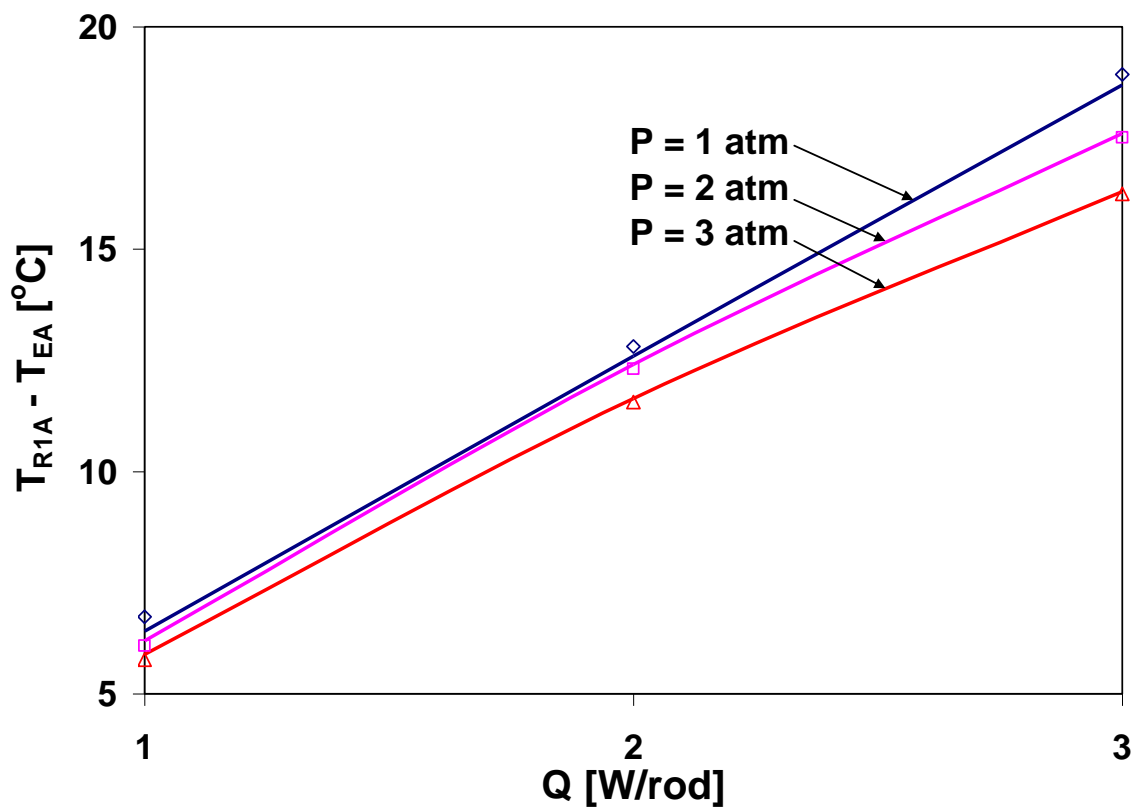


Figure 10 Average Rod 1 temperature difference versus heat load for air at different pressure. Symbols show the measured data. Lines show the average of the maximum simulated temperatures at the height of each measurement thermocouple.

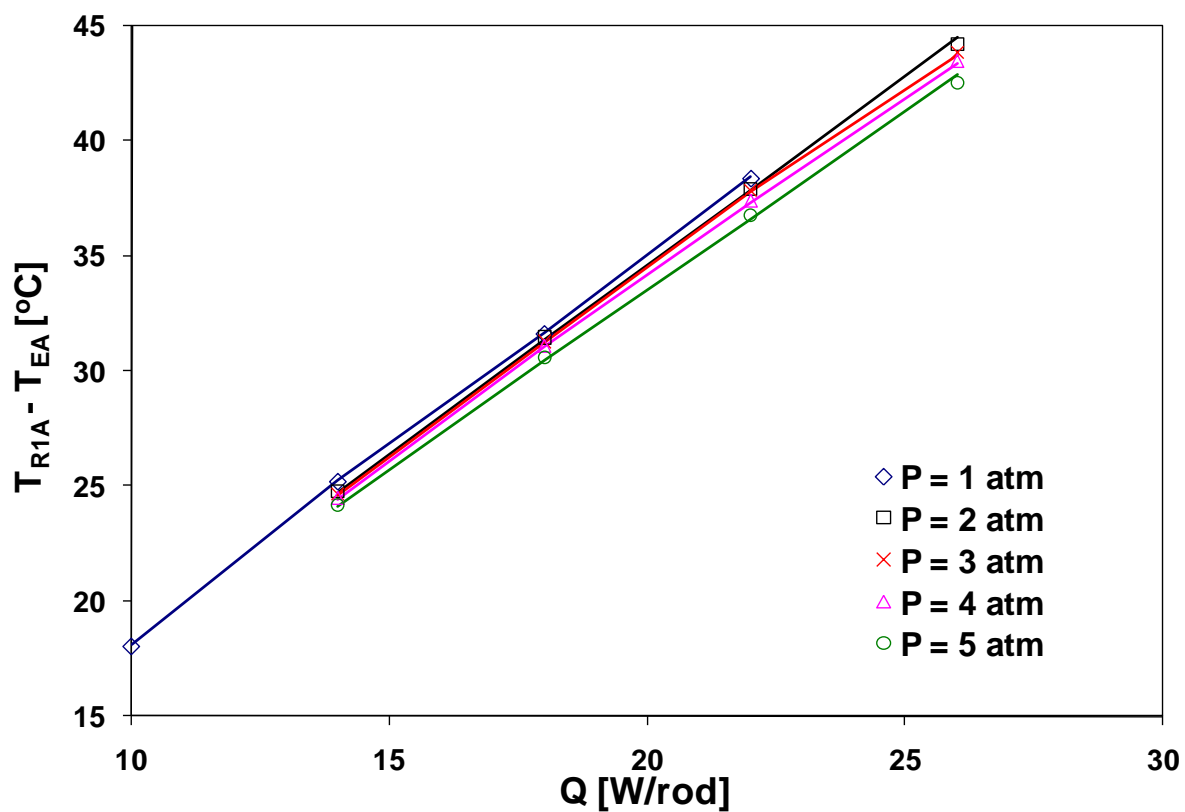


Figure 11 Average Rod-1 temperature difference versus heat load for helium at different pressure. Symbols show the measured data. Lines show the average of the maximum simulated temperatures at the height of each measurement thermocouple.

APPENDIX B

Benchmark of Computational Fluid Dynamics Simulations using Temperatures Measured within Enclosed Vertical and Horizontal Arrays of Heated Rods

ABSTRACT

Experiments and computational fluid dynamics/radiation heat transfer simulations of an 8×8 array of heated rods within an air-filled aluminum enclosure are performed. This configuration represents a region inside the channel of a boiling water reactor fuel assembly between two consecutive spacer plates. The rods are oriented horizontally or vertically to represent transport or storage conditions. The measured and simulated rod temperatures are compared for three different rod heat generation rates to assess the accuracy of the simulation technique. Simulations show that temperature gradients in the air are much steeper near the enclosure walls than they are near the center of the rod array. The measured temperatures of rods at symmetric locations are not identical, and the difference is larger for rods close to the wall than for those far from it. Small but uncontrolled deviations of the rod positions away from the design locations may cause these differences. The simulations reproduce the measured temperature profiles. For a total rod heat generation rate of 300 W, the maximum rod-to-enclosure temperature difference is 150°C. Linear regression shows that the simulations slightly but systematically over predict the hotter rod temperatures but under predict the cooler ones. For all rod locations, heat generation rates and rod orientations, 95% of the simulated temperatures are within 11°C of the correlation values. For the hottest rods, which reside

in the center of the domain where the air temperature gradients are small, 95% of the simulated temperatures are within 4.3°C of the correlation values. These results can be used to assess the accuracy of using simulations to design spent nuclear fuel transport and storage systems.

INTRODUCTION

Light water reactor fuel assemblies consist of zircaloy tubes held in square arrays by periodic spacer plates [1]. Boiling water reactor (BWR) assemblies vary from 7x7 to 9x9 arrays, while pressurized water reactor (PWR) assemblies vary from 14x14 to 18x18. The majority of tubes contain stacked uranium dioxide pellets. The remaining instrument sheath and guide thimble tubes are hollow. BWR assemblies have zircaloy channels around the tube array.

After the assemblies are used in power reactors, the fuel pellets are highly radioactive and generate heat [2]. Spent fuel is stored under water for a period of time to allow its heat generation and radioactive decay rates to decrease. It is then moved to thick-walled casks for dry storage or offsite shipment. In the casks, individual assemblies are supported within square cross-section openings of a basket structure. The region containing the fuel and basket is evacuated and backfilled with helium or another non-oxidizing cover gas. In transport the fuel rods are oriented horizontally. In storage the packages are frequently placed so that the fuel rods are vertical.

The zircaloy cladding provides an important containment boundary and its temperature must not exceed 400°C during normal conditions [3]. Solar heat flux and heat generated by the fuel make the package hotter than its surroundings [4, 5]. Package designers and operators must calculate the maximum or peak cladding temperature to assure that it does not exceed the allowed limit. The cask thermal dissipation capacity [6] is the fuel heat generation rate that brings the peak clad temperature to this limit. Cask operators can use this capacity to determine how many fuel assemblies may be safely loaded into a cask, and/or how long the fuel must be aged under water before being loaded.

Finite element models of loaded packages are employed to predict cask and fuel temperatures [4, 5]. In the past, computational resources were not available to accurately model the many fuel rods within the multiple fuel assemblies (some rail and truck transport cask have room for up to 21 and 4 PWR assemblies, respectively [4, 5]). The rods and cover gas within each basket opening were therefore replaced with homogenized solid elements with a uniform heat generation rate. Temperature-dependent Effective Thermal Conductivities (ETC) were applied to these elements [4, 7, 8, and 9]. They were developed to model the effects of conduction and radiation heat transfer in the directions normal to the rod axes.

Manteufel and Todreas [8] developed an analytical model for one-dimensional conduction and radiation within a rectangular array of heated fuel rods immersed in stagnant gas. They used this model to calculate a temperature-dependent ETC for the region within the fuel assembly, and a conductance model for the thin band between the

assembly envelope and the basket walls. This model neglects possible two-dimensional heat transfer effects at the corners, hollow instrument sheath and guide thimble tubes, external channels, and natural convection. Manteufel and Todreas used the ETC models they developed to conduct simulations of experiments that had been performed by other investigators. The simulations consistently over-predict the measured maximum cladding temperature.

Bahney and Lotz [9] performed two-dimensional finite element simulations of conduction and radiation heat transfer within the fuel assembly/cover gas region. They constructed one-quarter models of several BWR and PWR fuel assemblies. These geometrically-accurate models included unheated instrument sheath and guide thimble tubes, and external channels. The maximum cladding temperature was determined as functions of assembly heat generation rate and basket wall temperature. These simulations employed a uniform wall temperature to model fuel assembly/backfill gas cells near the package center, where the hottest fuel cladding resides. Effective thermal conductivity models of these regions were developed based on the simulation results. These models neglect the effect of non-uniform basket wall temperatures and natural convection. The symmetry condition that allowed one-quarter meshes to model full assemblies were not described, and mesh independence was not explicitly demonstrated. The results were not compared to experimental data.

A shortcoming of using thermal conductivity models to calculate temperatures within fuel assembly/cover gas regions is that they approximate heat flux at a location based

only on the temperature and its spatial gradient at that location. This is not universally appropriate when thermal radiation and/or natural convection effects are significant.

Radiant heat flux at a location is affected by temperatures at a distance. Natural convection is affected by the local fluid velocity, which depends on temperatures at other locations. As a result, an effective thermal conductivity that is appropriate for a basket opening whose walls are isothermal may not be accurate for openings with highly non-isothermal walls.

Current computational resources allow the use of meshes that accurately include the many fuel rods and unheated assembly components within a cask. Canaan and Klein performed two-dimensional computational fluid dynamics (CFD) simulations of an 8×8 array of heated rods in a uniform temperature enclosure [10], and benchmarked the results using experimental temperature measurements [11]. However, their wall boundary temperatures were much cooler and more isothermal than those expected on the walls of a transport cask basket opening [6, 12, 13]. Gomez-Araya and Greiner [14, 15] conducted two-dimensional simulations of geometrically-accurate PWR and BWR assemblies within high-temperature isothermal basket openings. Those simulations used the Fluent commercial CFD package. The simulations determined the conditions when buoyancy induced gas motion affects peak cladding temperature, as well as the sensitivity to cladding surface emissivity and geometric variations.

Venigalla and Greiner [12] and Gudipati and Greiner [13] performed two-dimensional simulations of whole truck and rail transport cask cross sections that included

geometrically accurate fuel rods in each basket opening. These simulations also used Fluent. Simulations that included buoyancy induced cover gas motion gave temperatures that were very close to those from stagnant gas simulations (in which the gas speed was set to zero). This indicates that natural convection does not strongly affect temperatures within horizontal transport cask. Results from these geometrically-accurate simulations were compared with a homogenized fuel model using the Manteufel and Todreas [8] ETCs. The geometrically accurate models predicted lower cladding temperatures and higher cask thermal dissipation capacities than the homogenized fuel model.

If the higher cask thermal dissipation capacities can be confirmed, spent fuel may not need to be aged under water for as long as indicated by the earlier homogenized models before being transferred to dry casks. The computational methods used in the geometrically accurate simulations must be benchmarked against relevant experimental data before it can be used with confidence.

Lovett [16] measured the temperature of an 8x8 array of heated horizontal rods within an aluminum enclosure. Experiments were performed for different gases in the enclosure, and ranges of gas pressure and rod heating rates. These conditions are similar to those of a BWR assembly within a transport cask. Fluent simulations of the experiments were performed that employed different assumptions regarding the thermal conditions of the endplates that held the heaters [17]. This was necessary because the endplate conditions were not completely documented. For a certain set of endplate assumptions, the simulation results accurately reproduced the experimental results.

Experiments performed by Arya and Keyhani [18, 19] measured the temperature of twelve vertical heated rods within a constant temperature, internally-finned cylindrical enclosure. Measurements were performed with air or helium in the enclosure for ranges of rod heat generation rates and gas pressures. Steady three-dimensional computational fluid dynamics simulations of conduction, natural convection and radiation heat transfer within the experiment were conducted to benchmark the simulation techniques [20]. In the computational model, different thermal conductivities were applied to a spacer plate between a plate that held the heaters and one of the enclosure endplates. This was done to model a range of contact resistance between the plates. This was necessary because the experimental endplate conditions were not completely documented. The calculations accurately reproduced the local and average temperatures when a low plate conductivity (corresponding to a high contact resistance) was modeled. These results emphasize that conditions far from measurement locations can affect experimental results. Those conditions must be well documented if they are to be used to benchmark computational methods.

In the current work an experimental facility is constructed consisting of an 8x8 array of heater rods within a square cross-section aluminum enclosure. It models a section of a spent BWR assembly between consecutive spacer plates, and within the assembly channel. The rod diameter, spacing between rods, and distance from the outermost rods to the enclosure wall are all 10% smaller than the dimensions inside the channel of a GE 8x8 BWR assembly [1]. Araya and Greiner [15] performed two-dimensional CFD

simulations of natural convection and radiation heat transfer for a horizontal BWR assembly within a uniform temperature basket cell. They showed that the channel surrounding the fuel rods and the gap between the channel and outer basket can be modeled analytically. As a result, only the region inside the channel is modeled in the current experiment.

The test facility can be placed so the rods are horizontal to simulate the conditions in a transport cask, or vertical to simulate storage conditions. The rod and enclosure temperatures are measured for a range of rod heat generation rates with atmospheric pressure air in the enclosure. These data are compared to three-dimensional simulations of conduction, natural convection and radiation heat transfer within the same domain using the Fluent CFD code. The goal of this work is to develop methods to quantitatively assess the accuracy of the computational method. This is done by benchmarking simulation results against data acquired in a facility with well documented boundary conditions.

EXPERIMENTAL FACILITY

Figure 1a is a picture of the 8×8 heater rod array used in the current experiment. Each rod is a Watlow Inc. tubular heater that is 1.1 cm in diameter and 67.3 cm long. The rods are made from 0.7-mm-thick Incoloy sheath with compressed magnesium oxide (MgO) powder inside. They are nearly straight, but when laid on a flat surface some exhibit gaps from bowing which are as large as 2 mm near the center. Each rod contains

a nichrome (NiCr) heater coil. The coil ends are connected to metal pins that are connected to external power leads. When current passes through the rods the heat generation is nearly uniform except for 3.2 cm (1.25 inch) unheated sections on both ends (where the connector pins are located). For the 64 rods, the average and standard deviation of the measured resistance are respectively, 4.0Ω and 0.12Ω . The rod surface emittance specified by the manufacturer is 0.8.

The sixty-four heaters are divided into eight sets of eight. Each set is wired in series. The sets are then wired in parallel with a 1000 W regulated DC power supply (HP 6218B). Experiments are performed for total heat generation rates of $Q = 100, 200$ and 300 W (1.56, 3.13 and 4.69 W/rod). The heat from each rod is the same to within 6%.

Thirty of the rods have a type-K (chromel/alumel) thermocouple at their mid-planes (additional rods had thermocouples that did not operate during this experiment). Figure 1b shows that they are constructed by inserting a chromel (Cr) rod into one end that is roughly half as long as the heater. A thermocouple junction is formed by wrapping an alumel (Al) wire around the end of the chromel rod. The other end of the alumel wire is connected to an alumel pin at the end of the heater. Thermocouple lead wires are connected to the chromel rod and alumel pin. In rods that contain thermocouples, both the heater and thermocouple are offset from the rod centerline. The heater coil is centered in rods that do not contain thermocouples. The positions of the heaters and thermocouples are not specified by the manufacturer, so their exact location and variation from rod to rod is not known.

Figure 2 shows the assembled apparatus. The heater array is inside a square cross section aluminum enclosure and is held by stainless steel plates on both ends. The

picture shows the apparatus in the horizontal position, but experiments are also performed with it vertical. The ends of the heaters protrude through holes in the endplates, and heater power and thermocouple lead wires are connected to them.

The enclosure is constructed by tungsten inert gas (TIG) welding of four 2.54-cm thick aluminum plates. The enclosure interior height and width are 11.8 cm, and they are uniform to within 0.3 cm. Its length is 60.9 cm, which is the same as the heated length of the rods. The aluminum surface emittance is estimated to be 0.5 [21].

The circles in Fig. 2 show the locations where type-K thermocouple probes (Watlow Mineral Insulated thermocouples) are inserted into wells in the enclosure. On each of the enclosure's four surfaces there are three wells halfway between the end plates, one on the centerline and two 2.1 cm from either edge. There are two more on each surface centerline, 2.54 cm from each endplate. Each well is a 1.7 mm-diameter blind hole, 2.29 cm deep (2.5 mm from the inner surface). The thermocouple probes were coated with thermally conducting grease, inserted to the bottom of its well, and glued near the well opening.

Two 15.24-cm-square, 6.4-mm-thick stainless steel plates are bolted to each end of the enclosure. Each has sixty-four holes drilled in a square array with center-to-center spacing 1.45 cm. The diameter of the holes is 1.13 cm, which is 0.38 mm larger than the rod diameter. The heaters are held by silicon rubber O-rings sandwiched between the pairs of plates on each end. The holes are beveled to accommodate the O-rings. The emittance of the stainless steel endplates is estimated to be 0.6 [21].

Figure 3 is a schematic from one end of the apparatus. The sixty-four circles represent heater rods, and the thirty filled circles are the ones that contain working

thermocouples. The rows and columns of rods are labeled A-H and 1-8. A gravity vector shows row H is at the bottom when the apparatus is horizontal. When the apparatus is vertical the gravity vector is aligned with the rod axes. The four X's among the heater rods show the locations where K-type Watlow grommet-terminal thermocouple assemblies are bolted to the exterior surface of the end plates. The figure also shows thermocouple wells in the aluminum enclosure walls. One additional thermocouple is placed 12.5 mm from the thermocouple at the center of the enclosure wall closest to row H. It is used to measure the enclosure reference temperature, T_{REF} .

The apparatus is located in a windowless laboratory with standard environmental temperature control ($\pm 3^\circ$). A thermocouple placed within 1 m of the apparatus is used to measure the laboratory environment temperature, T_{ENV} . Heat generated by the rods is ultimately transferred from the enclosure outer surfaces to the laboratory by natural convection and radiation. As a result the enclosure temperature increases with the rod heat generation rate. The enclosure is not gas tight so it is filled with laboratory pressure air (86 kPa at 1400 m elevation).

The laboratory environment and enclosure reference thermocouples (T_{ENV} and T_{REF}) are connected to electronic reference junction signal conditioners (Omega DRF-TC). The conditioner outputs are connected to an 80-channel data acquisition board (National Instruments NI-6225) installed in a personal computer. LabVIEW software is used to control the data acquisition card, as well as process and record the data.

The apparatus has 58 thermocouples (30 in the rods, 20 in the aluminum walls, and 8 on the endplates) in addition to the one that measured T_{REF} . All the alumel wires from those 58 thermocouples were connected together. The thermocouple at the center of

the wall nearest row H (Fig. 3) is used as a common reference. Its chromel wire is connected to the ground terminal of the data acquisition board. The chromel wires of the other 58 “sensing” thermocouples are connected to individual input channels of the data acquisition board. Assuming the data acquisition board terminals are at nearly the same temperature, this circuit essentially measures the temperature difference between the sensing thermocouples and the common. The common thermocouple temperature is assumed to be the same as that of the enclosure reference thermocouple, T_{REF} (they are 12.5 mm away from each other in the aluminum wall). This circuit is used to avoid the need for signal conditioners for each thermocouple.

The voltage differences between sensing and common thermocouples are measured by the data acquisition system as non-referenced, single-ended signals. All voltages were measured at a rate of 3000 samples/sec and averaged for 60 seconds to reduce the effects of radio frequency noise. The average sensed voltage V_S from each channel is recorded every second for the duration of the experiment.

The temperature of the sensing thermocouple for each channel T_S is determined from the voltage V_S for that channel and the temperature T_{REF} using the following expression [22]:

$$V_K(T_S) = V_S + V_K(T_{REF}). \quad (1)$$

In this expression, the function $V_K(T)$ is the type-K thermocouple output voltage for a sensing temperature of T referenced to a thermocouple at 0°C . In the LabVIEW program, a table look-up is used to find $V_K(T_{REF})$ from T_{REF} . A (reverse) table look-up is then used

to find T_S from $V_K(T_S)$. The confidence interval for this temperature measurement is estimated to be 2.1°C with a confidence level of 95%.

When the apparatus is horizontal, the measured temperatures are expected to be nearly equal at pairs of rods that are located symmetrically across a plane midway between rod columns 4 and 5 (Fig. 3). For example, the temperatures measured in rods D1 and D8 (see row letters and column numbers in Fig. 3) are expected to be nearly the same. When the apparatus is vertical, near symmetry is expected across that plane, the plane midway between rows D and E, and the diagonal planes (the planes connecting rods A1 and H8, and connecting rods A8 and H1). For the vertical orientation the rods may be broken into 10 symmetry groups. Table 1 shows the name of each group, the rods in each, and the name and number of rods in each group that are instrumented with thermocouples. The archetypical rod for each group is also indicated (these rods are indicated in Fig. 3 using asterisks (*)). If the experimental configuration (geometry and boundary conditions) is perfectly realized, and there are no measurement errors, then all the measured temperatures within each symmetry group will be the same.

However, some factors of the experimental configuration are not rigidly controlled and may disturb this symmetry. These factors include non-uniformity of: the rod spacing (due to rod curvature, the enclosure wall temperature, clearance between rod and endplate holes, and non-uniformity of the enclosure inner dimensions); the rod heat generation rate (due to differences in heater resistance), the rod and enclosure surface emittance; as well as variation of the apparatus from vertical or horizontal alignment. Variations of temperatures within each symmetry group are also caused by random measurement errors. The apparatus was designed so that the heater rods with

thermocouples are positioned so they measure temperatures of the expected hottest and coldest rods, and so that multiple measurements are made within each symmetry group. Unfortunately none of the thermocouples at the center of the array (Group S10 in Table 1) functioned during this study.

NUMERICAL MODEL

Figure 4 shows the finite volume computational meshes used in this work. They were created using the PATRAM mesh generator. Figure 4a shows a full three-dimensional domain and coordinate system. It includes sixty-four heater rods immersed in air and surrounded by the aluminum enclosure and stainless steel endplates. The dimensions and emissivities given in the last section, and temperature-dependent properties of the indicated materials were applied to the model. The region of the rods that protrudes outside the enclosure, the heater power and thermocouple lead wires, and contact resistance between solid components are not included in the model. Variations due to rod curvature, clearance between the rods and endplates, and possible non-uniformity of surface emissivity were also not included.

Figures 4b and 4c show detailed end views of a small region inside the enclosure. They include four the heater rods (Incoloy sheaths with magnesium oxide power inside) and atmospheric pressure air. Figures 4b and 4c show the course and fine meshes, which contain 174,928 and 330,167 grids, respectively. All results presented in the paper use the course mesh. Simulations using a fine mesh (which are not included in this paper) exhibit the same temperatures to within 0.16°C.

Conduction, natural convection and radiation heat transfer within the domain are simulated using the Fluent commercial computational fluid dynamics (CFD) package (version 6.3.26). Fluent solves for conservation of mass, momentum and energy equations using a finite-volume method with discretized governing equations. Pressure-velocity coupling is solved using the SIMPLE method. The mesh is constructed and the governing equations are solved with double precision. The steady solver and a second-order upwind scheme are used for the momentum and energy equations. The buoyancy-induced flow is generated by adding gravitational acceleration (9.81 m/s^2) in the $-y$ or $-z$ directions for the horizontal or vertical orientation, respectively. The temperature-dependent air density is included in the natural convection calculation. Radiation is solved for gray diffuse surfaces using the discrete ordinates method.

Simulations of each experiment were performed. As described in the last section, for each experiment the temperature of each enclosure wall was measured at five locations, and the temperature of each endplate was measured at four points. The average temperature on each of these walls was applied uniformly to the corresponding outer boundary of the computational mesh (future simulations will apply the measured temperatures closer to its inner surface, where it was actually measured). Uniform volumetric heating was applied throughout the magnesium oxide powder (the localized heating caused by the nichrome heater coil is neglected). The total simulated heat generation rate is the same as that of the corresponding experiment.

RESULTS

Initial Start-up and Wall Temperature Measurements

Figure 5 shows the measured thermocouple temperatures versus time after heater power was set to $Q = 200$ Watts, with the apparatus in the horizontal orientation. The temperatures of the laboratory environment, T_{ENV} , enclosure, endplates, and rods are identified. Initially, all temperatures increase until steady state was reached at approximately 9 hours. After 12 hours the environment temperature increases by roughly 2°C , and this caused the apparatus temperatures to increase by roughly the same amount. A new steady state was reached after $t = 17$ hr. The experiment was run for a total 22 hours. The steady state temperatures were determined by averaging the measured temperatures for the last 10 hours. The standard deviation of each temperature during this period was less than 0.7°C for the horizontal orientation, and 0.8°C for vertical.

Figure 6 shows the average of the steady state temperatures on both endplates and all four enclosure walls as functions of heat generation rate Q . Figures 6a and 6b show results for the apparatus in the horizontal and vertical orientation, respectively. For the horizontal orientation, all twenty aluminum enclosure wall thermocouples were isothermal to within $\pm 2.5^{\circ}\text{C}$. The average endplate temperatures are nearly the same as each other. However the endplates are roughly 5°C hotter than the aluminum walls because they are in direct contact with the heater rods. When the apparatus is vertical, the upper endplate is 3.5°C hotter than the lower one due to buoyancy-induced air motion inside and outside the enclosure. The aluminum wall thermocouples are isothermal within $\pm 0.5^{\circ}\text{C}$ for the vertical orientation, which is a smaller variation than for horizontal.

The average enclosure and endplate temperatures presented in Fig. 6 are applied as boundary conditions in the CFD simulations presented in the next section.

Simulation Results

Figure 7 shows simulation results for a heat load of 200 W and the apparatus in the horizontal orientation. Figure 7a shows rod temperature contours, while Fig. 7b presents temperature contours and velocity vectors in the plane halfway between the endplates. The vectors show that buoyancy induces upward air motion in the center of the domain and downward near the sides. As a result the highest temperatures are above the domain center. Figures 8a and 8b show similar results for the simulated apparatus in the vertical orientation. Again buoyancy causes the hottest region to be above the domain center.

Figure 9 shows the maximum air speed S_{MAX} within the domain versus rod heat generation rate from for both horizontal and vertical simulations. Vertical simulations exhibit significantly higher speeds because they involve a much larger vertical dimension. For both orientations the relative increase of S_{MAX} with heat load is lower at higher heat loads because a larger fraction of the total heat is transported by radiation.

Comparison of Measured and Simulated Temperatures

Figure 10 shows measured and simulated rod temperature in the plane midway between the endplates for the horizontal orientation. Figures 10a, 10b and 10c show results for $Q = 100, 200$ and 300 W, respectively. The temperature-difference between each location and the coolest wall location, $\Delta T = T(y) - T_{WALL,MIN}$, is plotted versus

elevation above the bottom aluminum wall, y . The lines show simulation results along vertical lines that bisect all eight rod columns. Even though the temperature boundary conditions applied to the enclosure walls are not exactly equal, the lines from symmetric column pairs 1&8, 2&7, 3&6, and 4&5 cannot be distinguished. To reduce crowding, results from columns 1&8 and 3&6 are presented in plots on the left, and those for columns 2&7 and 4&5 are presented on the right. The simulations show the rods are nearly isothermal and relatively large temperature gradients exist in the air.

Measured rod-to-wall temperature differences are presented using symbols. The data from symmetric column pairs (1&8, 2&7, 3&6, and 4&5) are given the same symbol. Ovals enclose data when more than two measurements were acquired at symmetric positions. We note that there are ten locations where symmetric measurements are made.

As discussed earlier, differences between measurements at symmetric points are caused by both random measurement errors and uncontrolled aspects of the apparatus (configuration errors). For all three heat-generation rates the largest difference between symmetric locations is near the upper wall of Columns 4&5 (rods A4 and A5 in Fig. 3). For $Q = 300 \text{ W}$ the difference is 22°C . The differences are significantly smaller at other positions, and they decrease as the heat generation rate decreases. We note that the simulated temperature profiles exhibit very steep gradients near the walls. As a result, displacements of the near-wall rods from their design location of 0.7 to 1.0 mm have the potential to cause the measured differences.

The rods in columns 4&5 near $y = 0.8$ (Rods C4 and C5) are near the center of the domain and exhibit the hottest measured temperatures. The measurements from this symmetric pair are very close. Small position variations of these rods are not expected to

cause as large a temperature variation as they would for rods near the walls. This is because the simulated temperature profiles exhibit much smaller temperature gradients in the vicinity of these rods than they do near the walls.

Comparing the simulated temperatures to the measurements, for many locations the temperature measurement relative to the simulated one is nearly the same for all heat generation rates. This may indicate systematic errors in the simulation methods, temperature measurements, or it may be caused by uncontrolled variations of the rod locations. However, close examination shows that the simulations under-predict the measured temperatures at more locations for the lowest heat generation rate than for the highest. For example, at $Q = 100$ W the simulations under-predict the maximum measured rod temperature (Rods C4 and C5), but over predict it at $Q = 300$ W.

Figure 11 shows the measured and simulated rod-to-wall temperature difference with the apparatus in the vertical orientation for $Q = 100, 200$ and 300 W. Results are presented for each symmetry group (described in Table 1) versus the x-location of the archetypical rod for that group. Once again, ovals encircle data when multiple measurements were performed for a given group. Symmetry group S4 contains rods that are near the enclosure walls and it exhibits the largest difference between measurements. As with the horizontal orientation, the temperature gradients normal to the wall are very steep, and shifts in rod position of 1.2 to 2.2 mm are sufficient to cause the measured temperature variations. Once again, the simulated rod-to-wall temperature difference follows the measured temperature profiles. While the simulations under predict the maximum measured temperature difference (in symmetry group S9) at the lowest heat generation rate, it over-predicts it high two highest rates.

Figure 12 is a plot of the simulated rod-to-wall temperature difference versus the measured value. Results are given for all 30 measured rods, all three heat generation rates, and both the horizontal and vertical rod orientations, totally $N = 180$ measurement/simulation results. Solid symbols are used for the hottest rods, C4 and C5. If the simulations modeled the experiment and its measurement errors perfectly, all data would lie on the line marked $\Delta T_{SIM} = \Delta T_{MEA}$.

Linear regression gives the solid line marked “ $\Delta T_{SIM,LR} = 1.037\Delta T_{MEA} - 3.9^\circ C$.” Systematic errors in the simulation and measurement methods, and in the experimental configuration cause this line to deviate from thin line marked “ $\Delta T_{SIM} = \Delta T_{MEA}$.” For example, using an incorrect value of the rod or wall surface emissivity, or an inappropriate end plate boundary condition in the simulations can cause systematic errors since it affects all simulation results. The regression line shows that, on average, the simulations slightly but systematically under-predict the lower temperatures, but over-predict the higher ones.

The actual measurement/simulation results in Fig. 12, $(\Delta T_{MEA,i}, \Delta T_{SIM,i})$ for $i = 1$ to N , deviate somewhat randomly from the regression line. This is caused by random errors in the simulations, experiment and apparatus configuration. The standard deviation of the *output* describes the vertical deviation of the data from the regression line and quantifies the random errors. It is defined as [23]

$$S_o = \sqrt{\frac{\sum_{i=1}^N [(1.037\Delta T_{MEA,i} - 3.9^\circ C) - \Delta T_{SIM,i}]^2}{N - 2}}$$

For the data in Fig. 12, $S_0 = 5.5^\circ\text{C}$. We therefore expect that 95% of the simulated results are within $2S_0 = 11^\circ\text{C}$ of the linear regression correlation.

For analysis of spent nuclear fuel casks it is crucial to predict the temperature of the hottest rods in an assembly to assure that none of the fuel cladding exceeds its temperature limit. The dashed line in Fig. 12 marked “ $\Delta T_{\text{SIM,LR}} = 1.11\Delta T_{\text{MEA}} - 10.6^\circ\text{C}$ ” shows the linear regression correlation for the hottest heater rods (C4 and C5). When using the current simulation methods, the best estimate for the maximum rod temperature is determined from the simulated value ΔT_{SIM} by inverting the regression correlation: $\Delta T = 0.90\Delta T_{\text{SIM}} + 9.5^\circ\text{C}$.

The data in Fig. 12 shows that the deviations of the data for rods C4 and C5 from their linear regression line are smaller than the deviations of the full data set from its regression correlation. Based on the standard deviation of the output, 95% of the data for rods C4 and C5 are within $2S_0 = 4.3^\circ\text{C}$ of the regression correlation, which is 61% smaller than it was for the full data set. This may be because the hottest rods are at the center of the domain where the temperature gradients are low. As a result, the measured temperatures are not as sensitive to variations of the rod position as they are at other locations.

CONCLUSIONS

Experiments and computational fluid dynamics/radiation heat transfer simulations of an 8×8 array of heated rods within an air-filled aluminum enclosure are performed.

This configuration represents a region inside the channel of a boiling water reactor fuel assembly between two consecutive spacer plates. The rods are oriented horizontally or vertically to represent transport or storage conditions. The measured and simulated rod temperatures are compared for three different rod heat generation rates to assess the accuracy of the simulation technique.

Simulations show that temperature gradients in the air are much steeper near the enclosure walls than they are near the center of the rod array. The measured temperatures of rods at symmetric locations are not identical, and the difference is larger for rods close to the wall than for those far from it. Small but uncontrolled deviations of the rod positions away from the design locations may cause these differences.

The simulations reproduce the measured temperature profiles. For a total rod heat generation rate of 300 W, the maximum rod-to-enclosure temperature difference is 150°C. Linear regression shows that the simulations slightly but systematically over predict the hotter rod temperatures but under predict the cooler ones. For all rod locations, heat generation rates and rod orientations, 95% of the simulated temperatures are within 11°C of the correlation values. For the hottest rods, which reside in the center of the domain where the air temperature gradients are small, 95% of the simulated temperatures are within 4.3°C of the correlation values. These results can be used to assess the accuracy of using simulations to design spent nuclear fuel transport and storage systems.

NOMENCLATURE

N	Number of measurements
Q	Total heat load
S_{MAX}	Maximum flow speed
t	Time
T	Local temperature
T_{ENV}	Environment temperature
T_{MAX}	Maximum temperature
T_{REF}	Enclosure reference temperature
$T_{WALL,MIN}$	Minimum wall temperature
x, y, z	Coordinate system
ΔT	Rod to wall temperature difference, $T - T_{MIN}$
ΔT_{MEA}	Measured rod to wall temperature difference
ΔT_{SIM}	Simulated rod to wall temperature difference

ACKNOWLEDGMENTS

This work was sponsored by the US Department of Energy, through Sandia National Laboratories under contract DE-C04-94AL85000, and by the Advanced Fuel Cycle Initiative under contract DE-FC07-06ID14782.

REFERENCES

- [1] U.S. Dept. of Energy, Office of Civilian Radioactive Waste Management (OCRWM), 1987, "Characteristics of Spent Nuclear Fuel, High-Level Waste, and Other Radioactive Wastes Which May Require Long-Term Isolation", DOE/RW-0184.

- [2] Saling, J.H. and Fentiman, A.W., 2001, *Radioactive Waste Management*, 2nd Edition, Taylor and Francis, New York.
- [3] NRC, 2005 "Cladding Considerations for the Transportation and Storage of Spent Fuel," Interim Staff Guidance Report for the Spent Fuel Project Office of the U.S. NRC, ISG-11 R3; available at www.nrc.gov
- [4] General Atomics (GA), 1998, "GA-4 Legal Weight Truck From-Reactor Spent Fuel Shipping Cask, Safety Analysis Report for Packaging (SARP)," San Diego, California 92186-5608.
- [5] Office of Civilian Radioactive Waste Management (OCRWM), US Department of Energy, 1993, "Multi-Purpose Canister (MPC) Implementation Program Conceptual Design Phase Report," DOC ID: A20000000-00811.
- [6] Greiner, M., Gangadharan, K.K., and Gudipati, M., 2007, "Use of Fuel Assembly/Backfill Gas Effective Thermal Conductivity Models to Predict Basket and Fuel Cladding Temperatures within a Rail Package During Normal Transport," *Nuclear Technology*, Vol. 160, pp. 325-336.
- [7] Unterzuber, R., Milnes, R.D., Marinkovich, B.A., and Kubancsek, G.M., 1982, "Spent-Fuel Dry-Storage Testing at E-MAD (March 1978 through March 1982)," prepared for the US DOE Commercial Spent Fuel Management Program Office at the Pacific Northwest Laboratory, B-D3339-A-G.
- [8] Manteufel, R. D. and Todreas, N. E., 1994, "Effective Thermal Conductivity and

Edge Conductance Model for a Spent-Fuel Assembly”, *Nuclear Technology*, Vol. 105, pp. 421-440.

[9] Bahney, R. H. and Lotz, T. L., 1996, “Spent Nuclear Fuel Effective Thermal Conductivity Report” U.S. DOE, Yucca Mountain Site Characterization Project Office, D.I.: BBA000000-01717-5705-00010 REV 00.

[10] Canaan, R E., and Klein, D.E., 1998, “A Numerical Investigation of Natural Convection Heat Transfer within Horizontal Spent-Fuel Assemblies”, *Nuclear Technology*, Vol. 123, Aug. pp. 193-208.

[11] Canaan, R.E., and Klein, D.E., 1996, "An Experimental Investigation of Natural Convection Heat Transfer within Horizontal Spent-Fuel Assemblies," *Nuclear Technology*, December, Vol.116, pp. 306-318.

[12] Venigalla, V.V.R., and Greiner, M., 2007, CFD Simulations of Natural Convection/Radiation Heat Transfer within the Fuel Regions of a Truck Cask for Normal Transport," PVP2007-26242, Proceedings of the 2007 ASME Pressure Vessels and Piping Division Conference, July 22-26, 2007, San Antonio, Texas.

[13] Gudipati, M., and Greiner, M., 2007, "CFD Simulations of Fuel Cladding and Basket Surface Temperatures in an MPC Rail Cask during Normal Transport," proceedings of the 15th International Symposium on the Packaging and Transportation of Radioactive Materials (PATRAM).

[14] Gomez, P.E.A., and Greiner, M., 2006, "2D Natural Convection and Radiation Heat Transfer Simulations of a PWR Fuel Assembly within a Constant Temperature Support Structure PVP2006-ICPVT-11-93332, Proceedings of PVP2006-ICPVT-11, 2006 ASME Pressure Vessels and Piping Division Conference, July 23-27, Vancouver, BC, Canada.

[15] Araya, P.E. and Greiner, M., 2007, "Use of Regular Rod Arrays to Model Heat Transfer from BWR Fuel Assemblies inside Transport Casks," *Packaging, Transport, Storage and Security of Radioactive Material*, Vol. 18, pp. 171-179.

[16] Lovett, P. M., 1991, "An Experiment to Simulate the Heat Transfer Properties of a Dry, Horizontal Spent Nuclear Fuel Assembly," M.S. Thesis, Nuclear Eng., Massachusetts Institute of Technology

[17] Gomez, P.E.A., and Greiner, M. 2006, "Benchmark Natural Convection/Radiation Simulations within an Enclosed Array of Horizontal Heat Rods," PVP2006-ICPVT-11-94021, Proceedings of PVP2006-ICPVT-11, 2006 ASME Pressure Vessels and Piping Division Conference, July 23-27, Vancouver, BC, Canada, to appear in *Nuclear Technology*.

[18] Arya, S., 1990, "Convective Heat Transfer in a Sealed Vertical Storage Cask Containing Spent Fuel Canisters," M.S. Thesis, Mechanical Engineering Department, University of Tennessee, Knoxville.

[19] Arya, S., and Keyhani, M., 1990, "Convective Heat Transfer in a Sealed Vertical Storage Cask Containing Spent Fuel Canisters," *Nuclear Science and Engineering*, Vol. 105, pp. 391-403.

[20] Chalasani, N.R., and Greiner, M. 2006, "Natural Convection/Radiation Heat Transfer Simulations of an Enclosed Array of Vertical Rods", PVP2006-ICPVT11-

93734, *Proceedings of PVP 2006 ASME Pressure Vessels and Piping Division Conference*, July 23-27, Vancouver, BC.

- [21] Incropera, F.P., and DeWitt, D.P., 1996, *Introduction to Heat Transfer, 3rd Edition*, Wiley.
- [22] Wheeler, A.J., and Ganji, A.R., 2004, *Introduction to Engineering Experimentation, 2nd Edition*, Prentice Hall.
- [23] Doebelin, E.O., 2004, *Measurement Systems, Application and Design, 5th Edition*, McGraw-Hill.

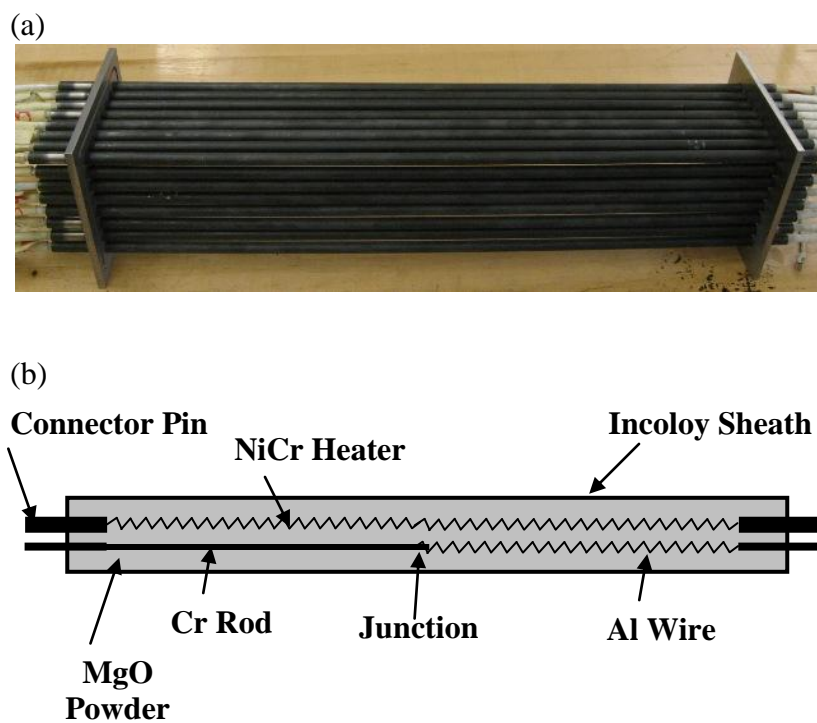


Figure 1 Experimental heaters (a) 8×8 array and end plates
(b) Axial cut through one rod showing internal components

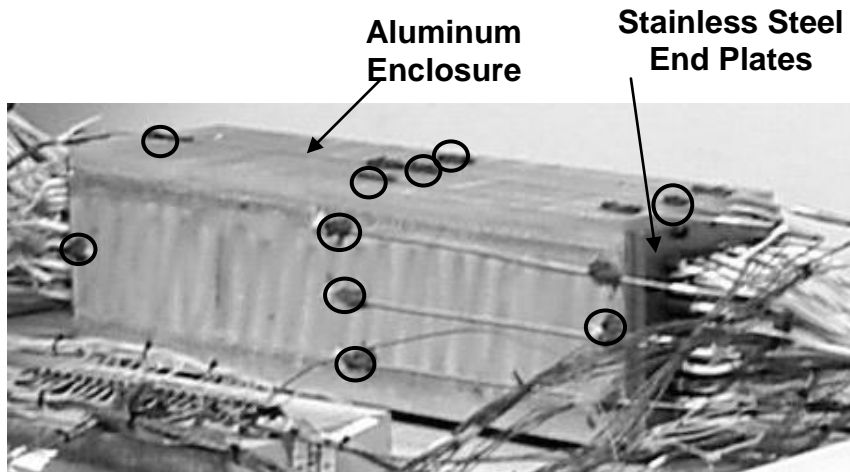


Figure 2 Photograph of aluminum enclosure and stainless steel end plates in the horizontal orientation. Circles show the locations where thermocouples enter wells drilled into the aluminum walls. Heater power and thermocouple lead wires exit through the end plates.

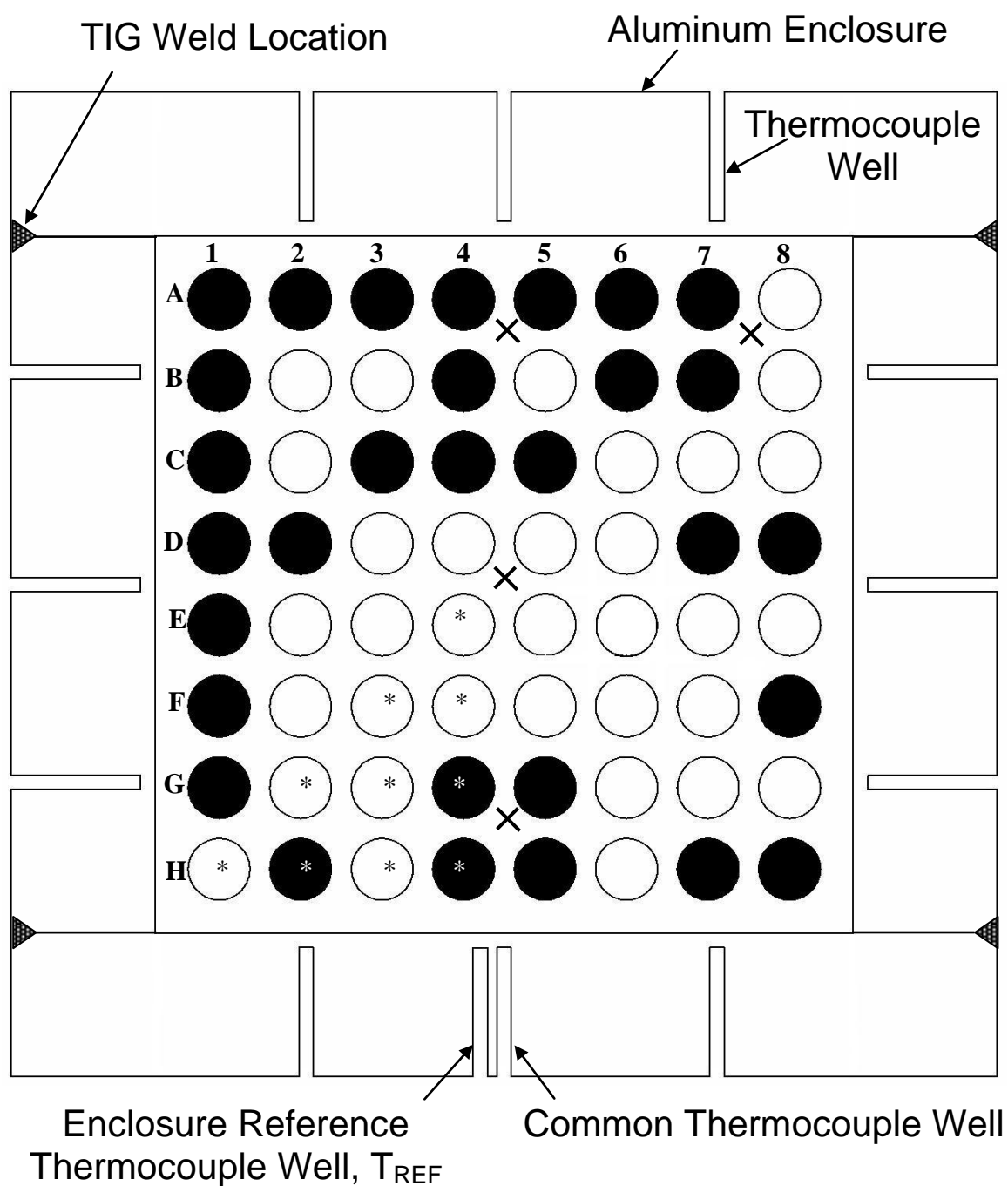


Figure 3 End view of experimental apparatus showing 64 heater rods (circles), locations of 4 end plate thermocouples (x's), aluminum enclosure walls, and wall thermocouple wells. Filled circles are the rods that are instrumented with thermocouples. The direction of the gravity vector when the apparatus is in the horizontal orientation is shown. Columns 1-8, and rows A-H are labeled.

Symmetry Group Name	Rods in Symmetry Group	Rods with TCs in Group	Number of Rods with TCs in Group
S1	A1, A8, <u>H1</u> , H8	A1, H8	2
S2	A2, A7, B1, B8, G1, G8, <u>H2</u> , H7	A2, A7, B1, G1, H2, H7	6
S3	A3, A6, C1, C8, F1, F8, <u>H3</u> , H6	A3, A6, C1, F1, F8	5
S4	A4, A5, D1, D8, E1, E8, <u>H4</u> , H5	A4, A5, D1, D8, E1, H4, H5	7
S5	B2, B7, <u>G2</u> , G7	B7	1
S6	B3, B6, C2, C7, F2, F7, <u>G3</u> , G6	B6	1
S7	B4, B5, D2, D7, E2, E7, <u>G4</u> , G5	B4, D2, D7, G4, G5	5
S8	C3, C6, <u>F3</u> , F6	C3	1
S9	C4, C5, D3, D6, E3, E6, <u>F4</u> , F5	C4, C5	2
S10	D4, D5, <u>E4</u> , E5	--	0

Table 1 Rod symmetry groups for the vertical orientation. The archetypical rod for each group is underlined.

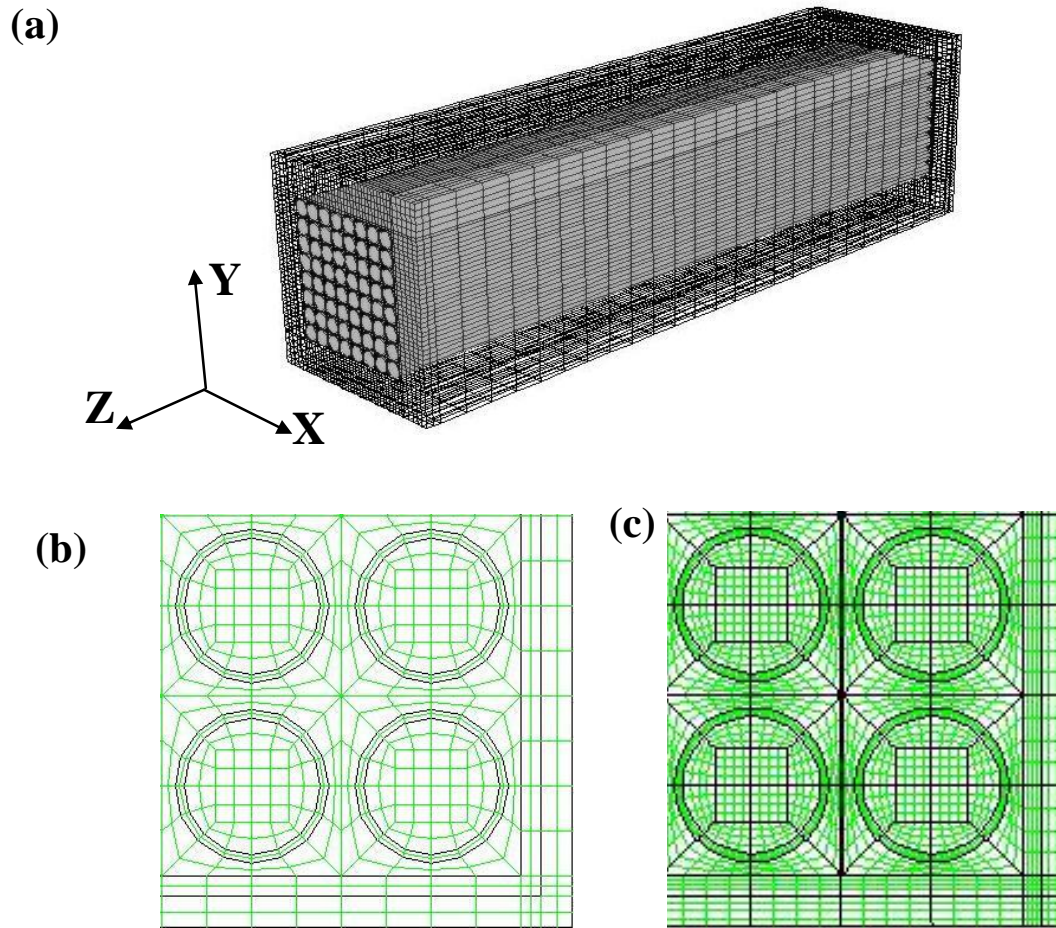


Figure 4 Finite volume grid (a) Three-dimensional mesh and coordinate system (b) Detail end view of course grid (174,928 elements), (c) Detail end view of fine grid (330,167 elements)

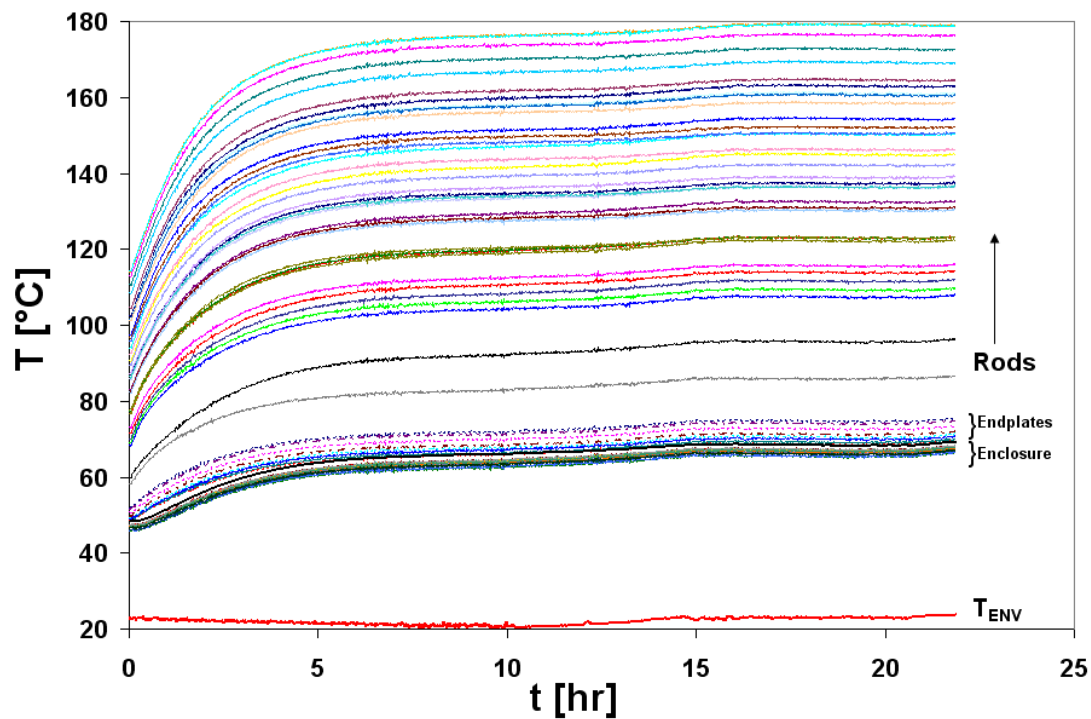


Figure 5 Measured temperature of all 60 thermocouples versus time with the apparatus in the horizontal orientation and $Q = 200$ W. The environment, enclosure, end plate, and rod temperatures are identified.

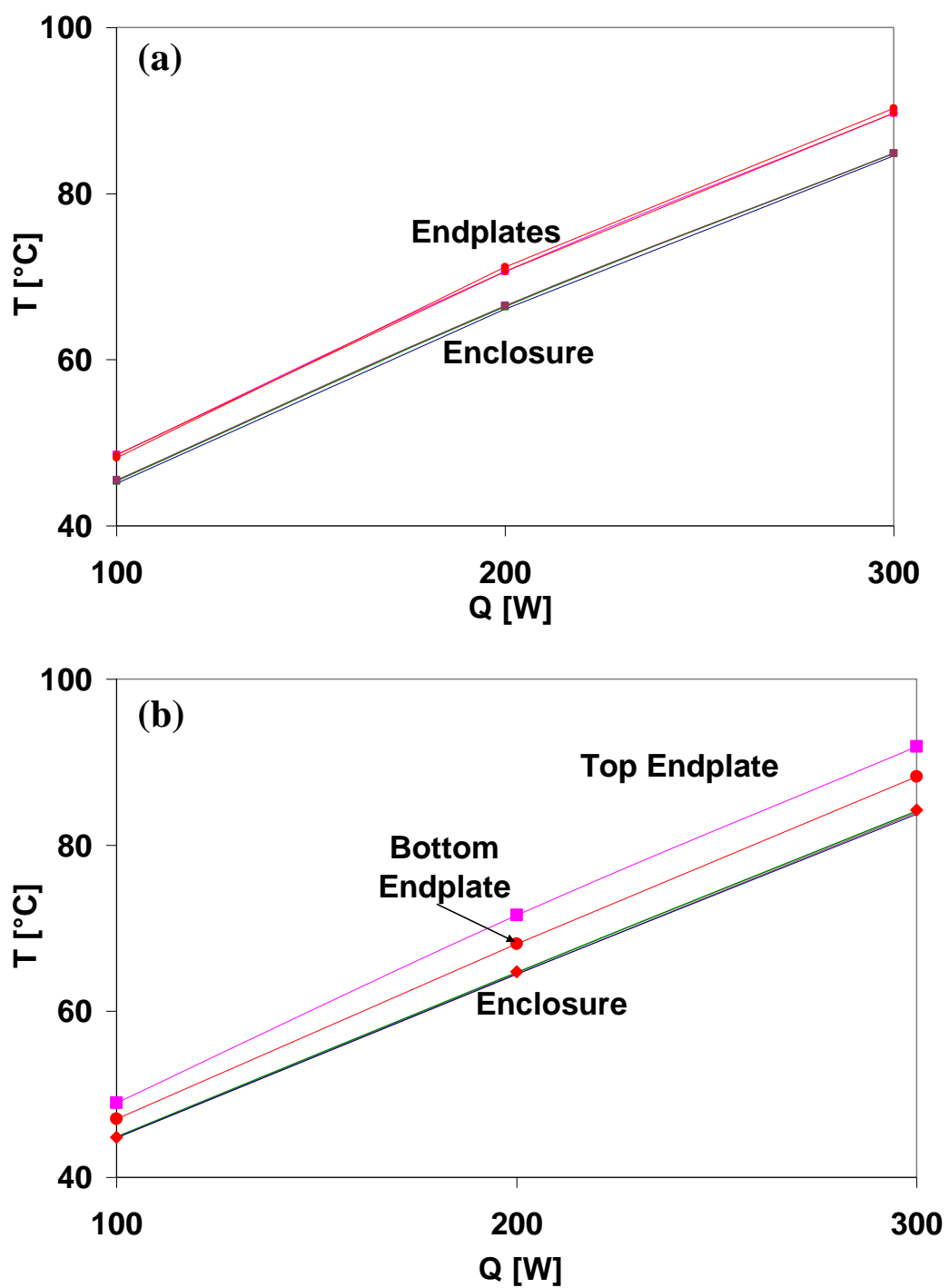


Figure 6 Measured aluminum side wall and stainless steel end plates temperatures versus rod heat generation rate (a) Horizontal orientation, and (b) Vertical orientation (top and bottom end plate temperatures are distinguishable).

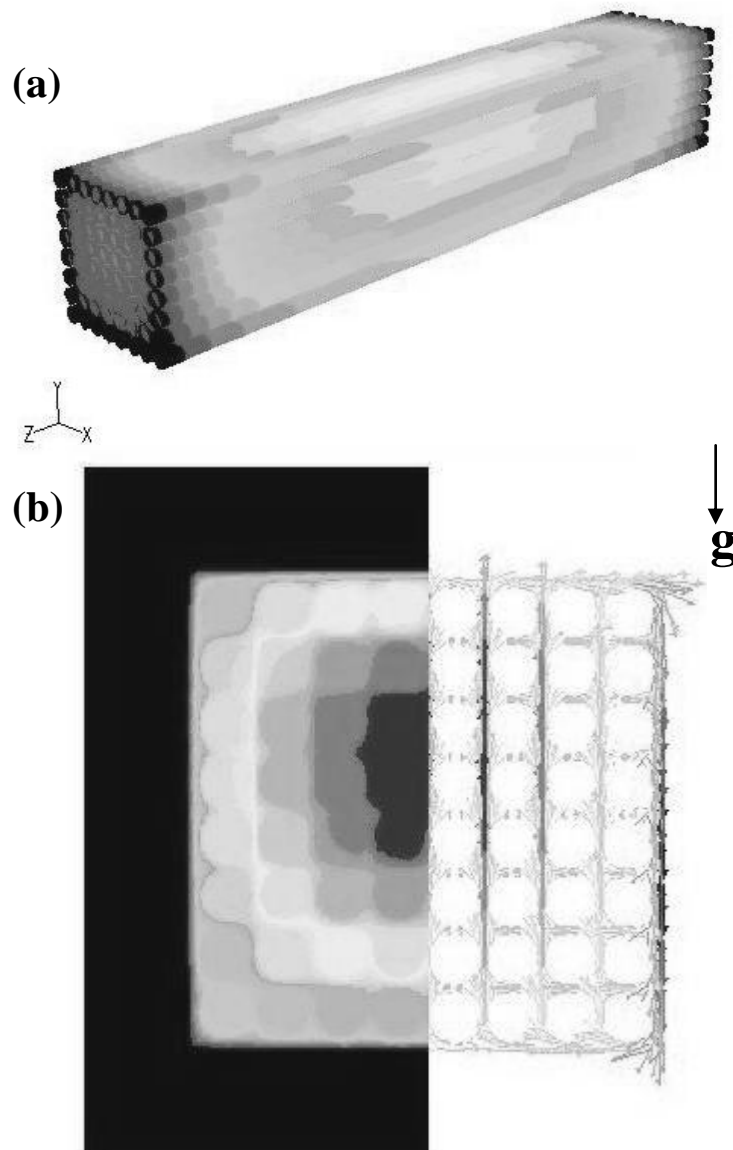


Figure 7 Simulation results for horizontal orientation at $Q = 200$ W (a) Rod surface temperature contours (b) Enclosure, gas and rod temperature contours and gas velocity field vectors at midplane between endplates.

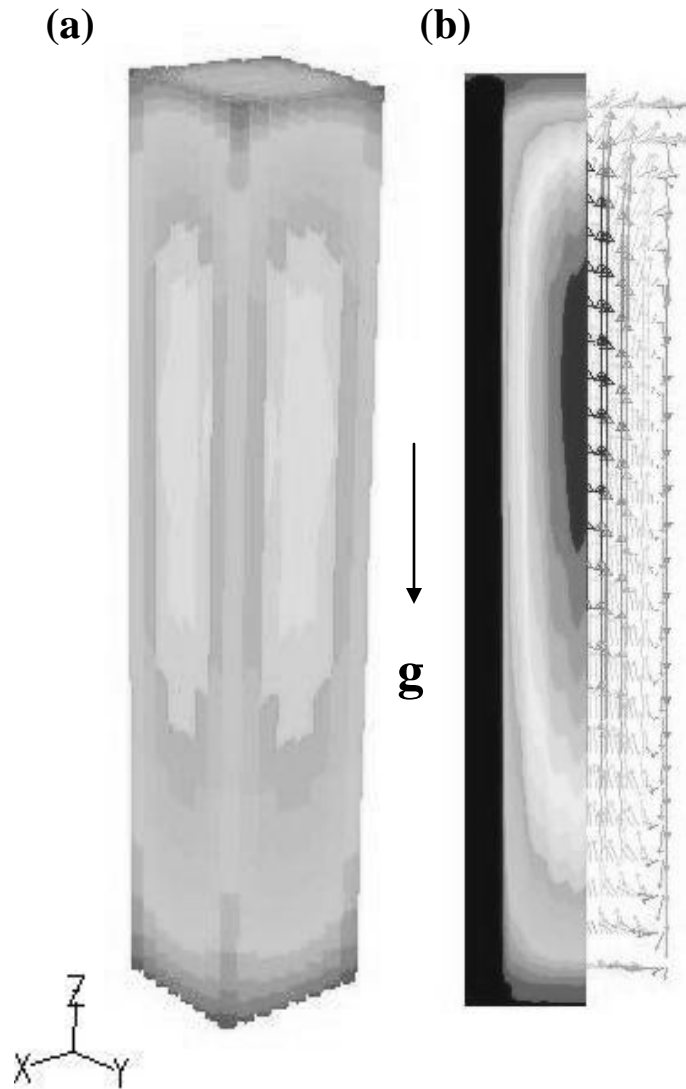


Figure 8 Simulation results for vertical orientation at $Q = 200 \text{ W}$ (a) Rod surface temperature contours (b) Enclosure and gas temperature contours and gas velocity field vectors in vertical midplane.

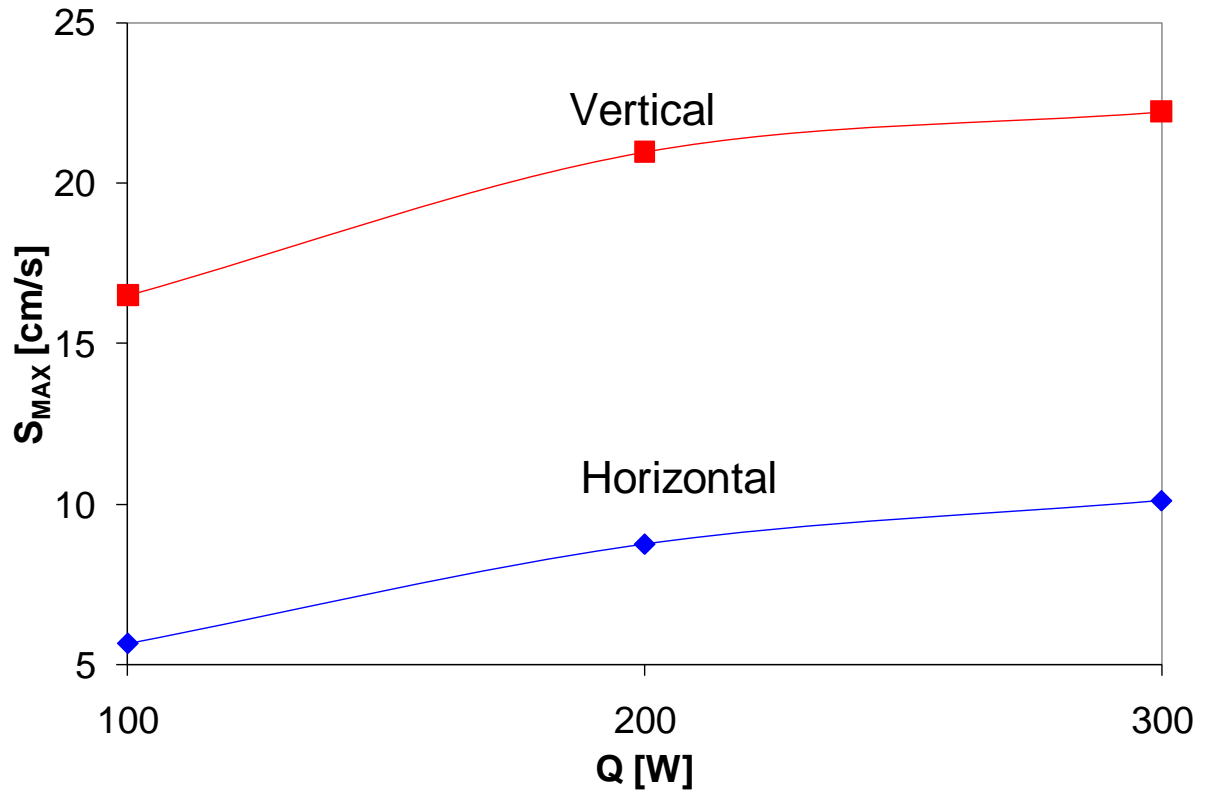


Figure 9 Simulated maximum air speed versus rod heat generation rate for horizontal and vertical orientations

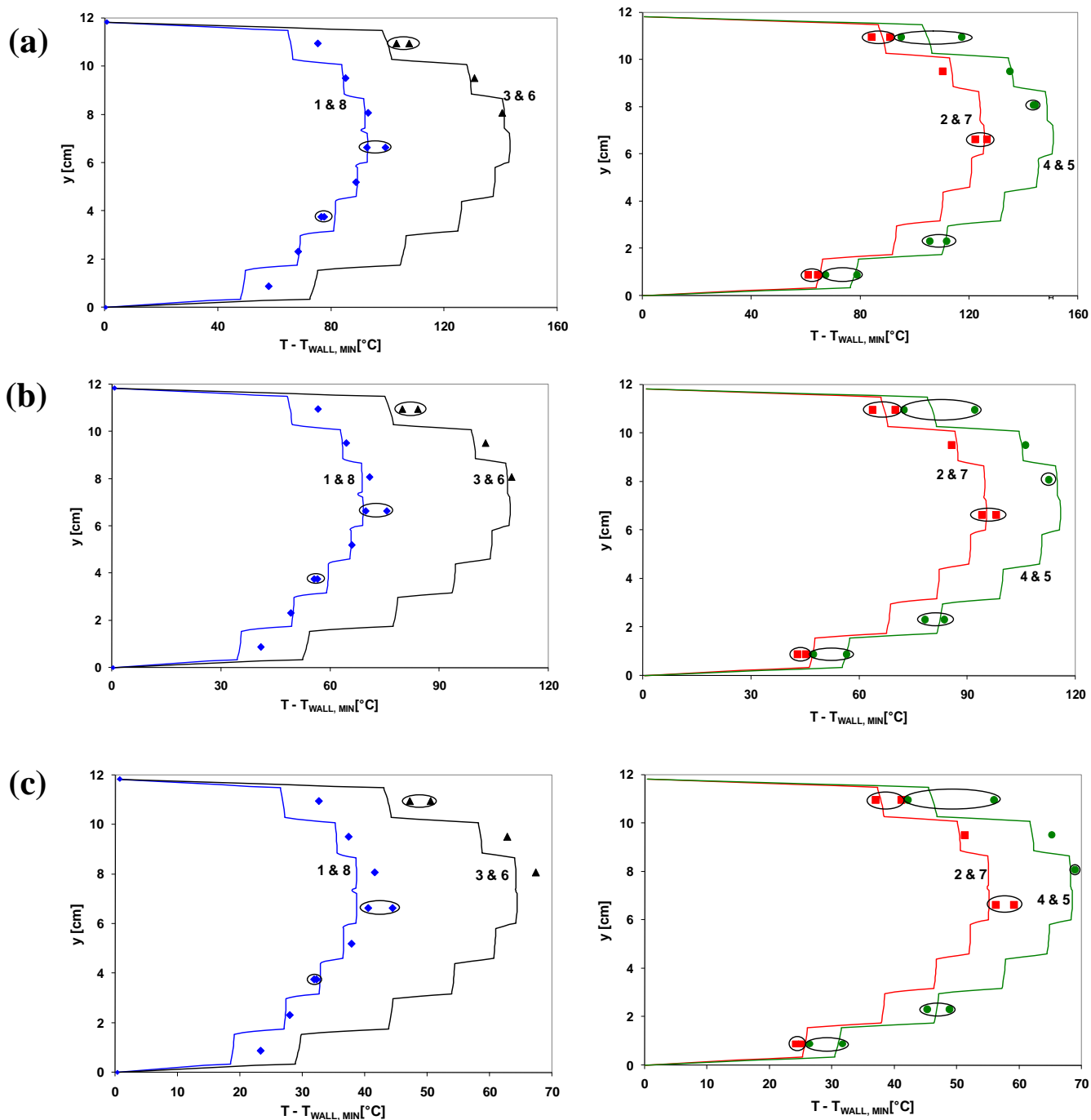


Figure 10 Measured (symbols) and simulated (lines) mid-plane temperature difference versus y-location for the horizontal orientation. Results from the following symmetric columns are paired together, 1&8, 2&7, 3&6 and 4&5. Ovals are used when two measurements were acquired for in paired columns (a) 100 W (b) 200 W (c) 300 W.

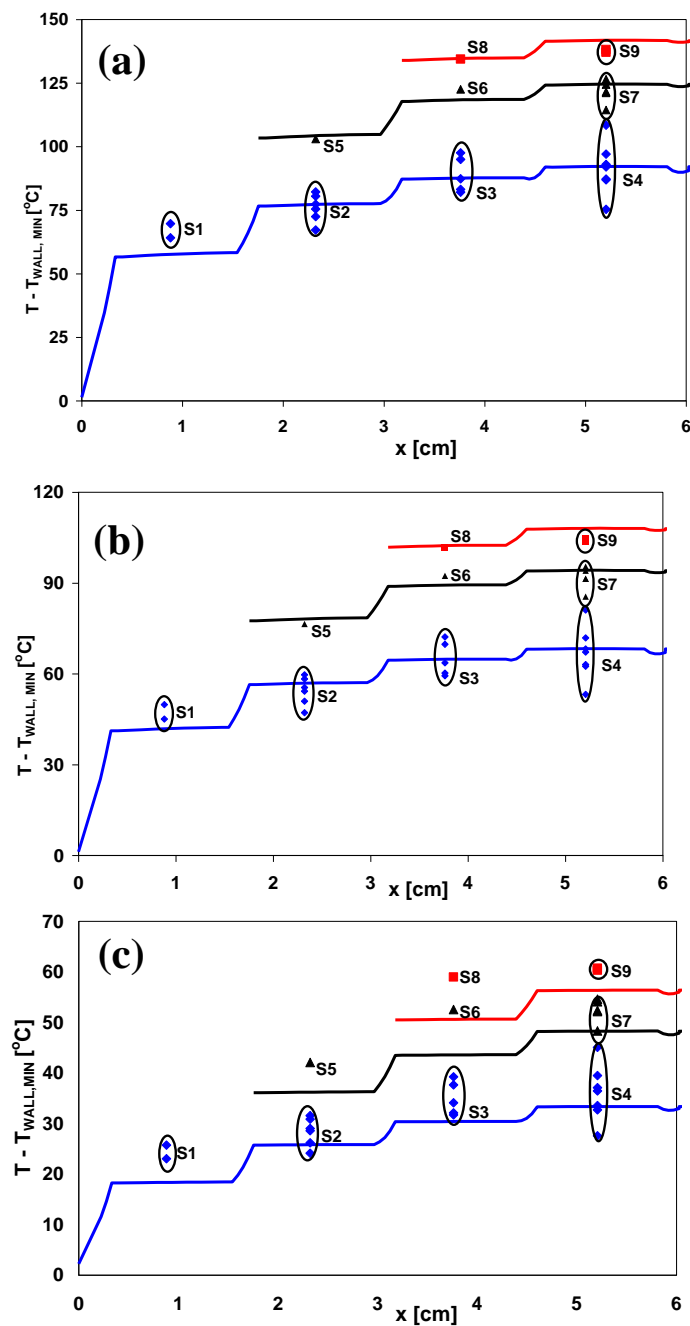


Figure 11 Measured (symbols) and simulated (lines) mid-plane temperature difference for the vertical orientation. Results for each symmetry group are plotted versus the x-location for the archetypical rod in each group. Ovals enclose data where multiple measurements within a group exist (a) 100 W (b) 200 W (c) 300 W.

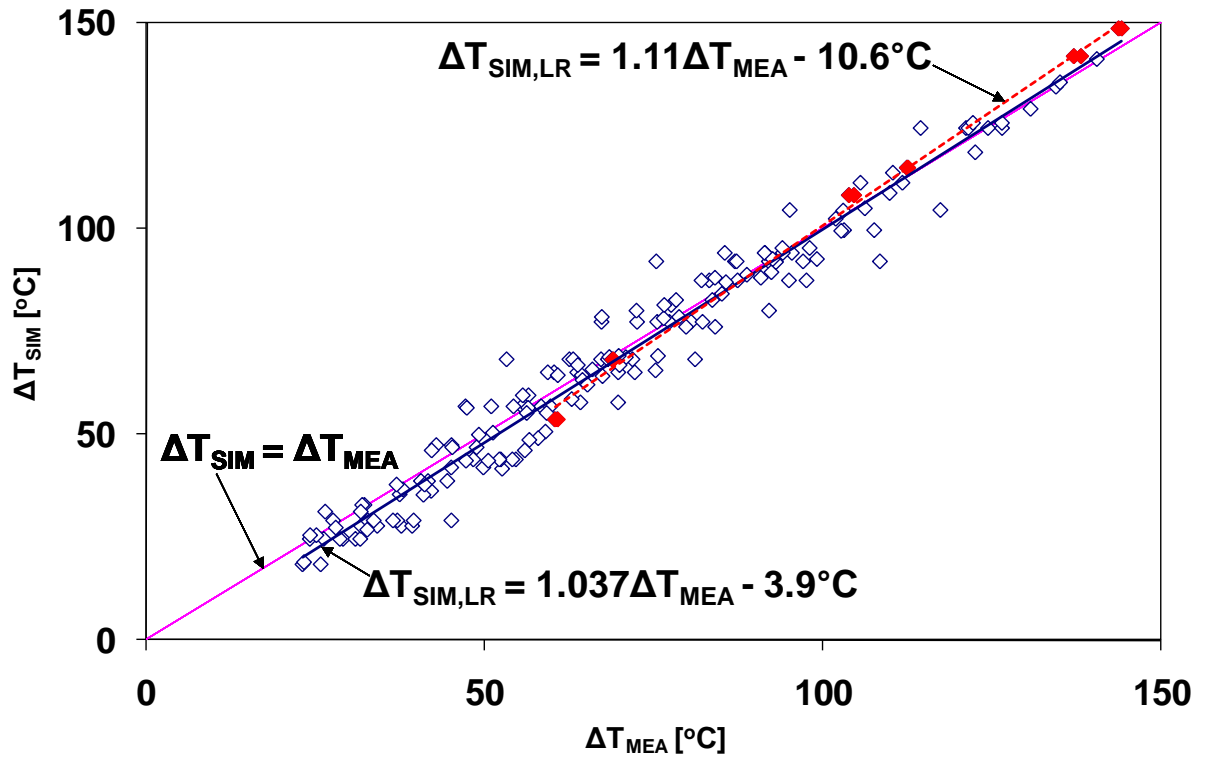


Figure 12 Simulated versus measured rod temperature differences for the horizontal and vertical orientations for $Q = 100 \text{ W}$, 200 W , and 300 W . Filled symbols are used for the data from the hottest measured rods (C4 and C5)